Mitochondrial Calcium Signaling Regulates Branched-Chain Amino Acid Catabolism in Fibrolamellar Carcinoma

Nicole M. Marsh

A dissertation
submitted in partial fulfillment of the
requirements for the degree of

Doctor of Philosophy

University of Washington
2024

Reading Committee:
Yasemin S. Sancak, Chair
Ning Zheng
Dana Miller

Program Authorized to Offer Degree:
Pharmacology

University of Washington

Abstract

Mitochondrial Calcium Signaling Regulates Branched-Chain Amino Acid Catabolism in Fibrolamellar Carcinoma

Nicole M. Marsh

Chair of the Supervisory Committee:
Yasemin S. Sancak
Department of Pharmacology

Metabolic adaptations in response to changes in energy supply and demand are essential for survival. The mitochondrial calcium uniporter coordinates metabolic homeostasis by regulating TCA cycle activation, mitochondrial fatty acid oxidation and cellular calcium signaling. However, a comprehensive analysis of uniporter-regulated mitochondrial metabolic pathways has remained unexplored. Here, we investigate the metabolic consequences of uniporter loss- and gain-of-function and find that mitochondrial calcium signaling regulates the branched-chain amino acid (BCAA) catabolism pathway. Loss of uniporter function activates the pathway through two mechanisms: increased expression of pathway proteins and stimulation of the enzyme that catalyzes the committed step of the pathway by dephosphorylation. Conversely, in the liver cancer fibrolamellar carcinoma (FLC) – which we demonstrate to have increased mitochondrial calcium levels

– expression of BCAA catabolism enzymes is suppressed. The transcription factor KLF15, a master regulator of liver metabolic gene expression, is also regulated by mitochondrial calcium signaling. KLF15 is downregulated in FLC patient tumors and cellular models. The KLF15 target gene ornithine transcarbamylase (OTC) is downregulated in FLC, which is thought to contribute to urea cycle defects and hyperammonemia observed in some FLC patients, suggesting a role for mitochondrial calcium in hyperammonemia. Inhibition of uniporter activity in FLC cellular models upregulates KLF15, BCAA catabolism genes, and OTC. Collectively, we identify an important role for mitochondrial calcium signaling in metabolic adaptation through transcriptional and post-translational regulation of metabolism and elucidate its importance for BCAA and ammonia regulation in FLC.

ACKNOWLEDGEMENTS

This work – and the experiments that did not make it into this dissertation – could not have been done without the support and guidance of my two mentors Drs. Richard Gardner and Yasemin Sancak. I am proud to have completed graduate school as a former trainee of Dr. Gardner, and I hope to be part of his lasting scientific legacy. He made scientific research fun and welcoming. Yasemin, thank you for opening your lab to me and giving me equal measures of guidance and intellectual freedom to continue growing as a researcher. It has been a joy and an honor to work with you.

Thank you to the UW Department of Pharmacology for creating a supportive learning environment. I am also grateful for the many hours put in by my committee members, Drs. Ning Zheng, Dana Miller, Edith Wang and W. Conrad Liles and by my colleagues in the Gardner and Sancak labs who helped to shape and strengthen this work.

To my friends in and out of the lab, thank you for supporting me through this journey. Graduate school came with setbacks and growing pains, and I am thankful that you walked with me through hard times and cheered me on.

No words of gratitude are sufficient to pay tribute to the many ways my parents have poured into me and prepared me to accomplish this goal. Mom, I did it (as you knew I would)! Thank you for modeling how to tackle challenges with grace and tenacity and for raising me to be a lifelong learner. Dad, thank you for your steadfast support and wise perspective when I cannot see the path ahead. I could not have done this without you.

DEDICATION

This is my father's world.
E'en yet to my listening ears,
All nature sings, and around me rings,
The music of the spheres.

This is my Father's world.
I rest me in the thought,
Of rocks and trees, of skies and seas,
His hands the wonders wrought.

This is my Father's world.
The birds that their carols raise,
The morning light, the lily white,
Declare their maker's praise.

This is my Father's world.
He shines in all that's fair.
In the rustling grass I hear Him pass,
He speaks to me everywhere.

- By Maltbie Davenport Babcock

TABLE OF CONTENTS

LIST OF FIGURES

LIST OF SUPPLEMENTAL FIGURES

LIST OF SUPPLEMENTAL TABLES

LIST OF ABBREVIATIONS

-/- – homozygous deletion

°C – degrees Celsius

A – amp

Å – Angstrom

ACADM – medium-chain specific acyl-CoA dehydrogenase, mitochondrial

ACAT1/2 – acetyl-CoA transferase 1/2

ACSF3 – acyl-CoA synthetase family member 3

ADP – adenosine diphosphate

AGC1/2 – aspartate-glutamate carrier 1/2

AKAP – A kinase anchoring protein

ALS – amyotrophic lateral sclerosis

AML12 – alpha mouse liver 12 cell line

ANOVA – analysis of variance

aq. – aqueous

ATCC – American Type Culture Collection

ATP – adenosine triphosphate

BAG2 – Bcl-2-associated athanogene 2

BCAA – branched-chain amino acid

BCAT – branched-chain aminotransferase

BCKA – branched-chain α-keto-acid

BCKDH – branched-chain α-keto-acid dehydrogenase

BCKDK – branched-chain α-keto-acid dehydrogenase kinase

BSA – bovine serum albumin

Ca^{2+} – calcium divalent cation

$CaCl_2$ – calcium chloride

CAM – 2-chloroacetamide

cAMP – cyclic adenosine monophosphate

CCCP – carbonyl cyanide m-chlorophenyl hydrazone

cDNA – complimentary deoxyribonucleic acid

cm – centimeter

CMV – cytomegalovirus promoter

CO_2 – carbon dioxide

CoA – coenzyme A

CRISPR – clustered regularly interspaced short palindromic repeats

d-AKAP1 – dual-specificity protein kinase A anchoring protein 1

DAPI – 4’,6-diamidino-2-phenylindole

DBT – dihydrolipoamide branched chain transacylase, subunit E2

ddH_2O – double distilled water

DIA – data-independent acquisition

DLD – dihydrolipoamide dehydrogenase

DMEM – Dulbecco’s Modified Eagle Medium

DMSO – dimethyl sulfoxide

DNA – deoxyribonucleic acid

DP – DNAJ-PKAc fusion

ECHB –enoyl-CoA hydratase, beta subunit

ECL – enhanced chemiluminescence

EDTA – ethylenediaminetetraacetic acid

EM – electron microscopy

Em – emission

EMRE – essential MCU regulator

EMT – epithelial to mesenchymal transition

ER – endoplasmic reticulum

Ex – excitation

$FADH_2$ – dihydroflavine adenine dinucleotide

FALDH – fatty aldehyde dehydrogenase
FAO – fatty acid oxidation
FBS – fetal bovine serum
FCCP – trifluoromethoxyphenylhydrazone
FDR – false discovery rate
FLC – fibrolamellar carcinoma
g – gram
GFP – green fluorescent protein
G-GECO – green genetically encoded calcium indicator for optical imaging
GO – gene ontology
gRNA – guide ribonucleic acid
H&E – hematoxylin and eosin stain
H^+ – proton
HADH – hydroxyacyl-CoA dehydrogenase
HADHA – hydroxyacyl-CoA dehydrogenase alpha subunit
HCC – hepatocellular carcinoma
HCO_3^- – bicarbonate anion
HEK293T – human embryonic kidney 293 cells, transformed
HeLa – Henrietta Lacks cell line
HEPES – 2-[4-(2-hydroxyethyl)piperazin-1-yl]ethanesulfonic acid
HPLC – high-performance liquid chromatography
hr – hour
HRP – horseradish peroxidase
HSP – heat shock protein
IDH – isocitrate dehydrogenase
IHC – immunohistochemistry
IMM – inner mitochondrial membrane
IMS – intermembrane space

IRB – institutional review board
IU – International Unit
K^+ – potassium cation
K_2HPO_4 - dipotassium hydrogen phosphate
kb – kilobase
KCl – potassium chloride
KEGG – Kyoto Encyclopedia of Genes and Genomes
KLF15 – Krüppel-like factor 15
KOH – potassium hydroxide
kV – kilovolt
LC-MS – liquid chromatography mass spectrometry
LC-MS/MS – liquid chromatography tandem mass spectrometry
LETM1 – leucine zipper and EF-hand containing transmembrane protein 1
M – molar
m/z – mass-to-charge ratio
MCEE – methylmalonyl-CoA epimerase
MCU – mitochondrial calcium uniporter
MCUB – mitochondrial calcium uniporter dominant negative subunit beta
$MgCl_2$ – magnesium chloride
MICU1/2 – mitochondrial calcium uptake 1/2
min – minute
mL – milliliter
mM – millimolar
MMSDH -methylmalonate-semialdehyde dehydrogenase
MMUT – methylmalonyl-CoA mutase
mPTP – mitochondrial permeability transition pore
mRNA – messenger ribonucleic acid
MS – mass spectrometry

ms – millisecond

mtCU – mitochondrial calcium uniporter complex

mtDNA – mitochondrial deoxyribonucleic acid

mtGPDH – mitochondrial GAPDH glyceraldehyde-3-phosphate dehydrogenase

mTORC1 – mechanistic target of rapamycin complex 1

mV – millivolt

Na$^+$ - sodium cation

NaCl – sodium chloride

NAD$^+$ – nicotinamide adenine dinucleotide

NADH – nicotinamide adenine dinucleotide hydride

NCLX – Na$^+$/Ca^{2+} exchanger

ng – nanogram

NH$_4^+$ – ammonium cation

NHS – normal horse serum

nL – nanoliter

nm – nanometer

nM – nanomolar

NTL – non-tumor liver

OCR – oxygen consumption rate

OGDH – oxoglutarate dehydrogenase

oligo – oligonucleotide

OMM – outer mitochondrial membrane

OTC – ornithine transcarbamylase

OXCT1/2 – 3-oxoacid CoA-transferase ½

OXPHOS – oxidative phosphorylation

PAGE – polyacrylamide gel electrophoresis

PBS – phosphate-buffered saline

PCCB – propionyl-CoA carboxylase subunit beta

PCR – polymerase chain reaction

PDH – pyruvate dehydrogenase (PDH)

PDP – pyruvate dehydrogenase phosphatase

P_i – inorganic phosphate

PKAc – protein kinase A, catalytic subunit

pmol – picomole

PPM1K – protein phosphatase Mn^{2+}-dependent 1K

PTM – post-translational modification

pt – patient

PVDF – polyvinylidene difluoride

qPCR – quantitative polymerase chain reaction

RFP – red fluorescent protein

RIPA – radioimmunoprecipitation assay buffer

ROS – reactive oxygen species

rpm – revolutions per minute

SCaMC1/2/3/L1 – calcium-binding mitochondrial carrier 1/2/3/L1

SDS – sodium dodecyl sulfate

sec – second

shRNA – short hairpin ribonucleic acid

SR – sarcoplasmic reticulum

TBST – tris-buffered saline with Tween

TCA – tricarboxylic acid

TCA – trichloroacetic acid

TCEP – tris(2-carboxyethyl)phosphine hydrochloride

TCGA – the Cancer Genome Atlas

TEAB – triethylammonium bicarbonate

TEM – transmission electron microscope

THIM – 3-ketoacyl-CoA thiolase, mitochondrial

TMRM – tetramethylrhodamine methyl ester

TOM20 – translocase of the outer membrane subunit 20

V – volt

v/v – volume per volume

VDAC – voltage-dependent anion channel

VSV-G -vesicular stomatitis virus glycoprotein

WT – wild-type

wt/vol – weight per volume

$\Delta\Psi_m$ – mitochondrial membrane potential

µF – microfarad

µg – microgram

µL – microliter

µm – micrometer

µM – micromolar

CHAPTER 1 | INTRODUCTION

1.1 | Overview of cellular metabolism

1.1.1 | The importance of metabolic adaptability

Cellular metabolic reactions fuel every function our bodies perform. This process may appear simple on the surface; we consume food which provides the energy necessary for us to remain active. At the molecular level, however, it is astoundingly complex. It has been estimated that each of our cells performs approximately one billion biochemical reactions every second [1]. These reactions produce critical energy sources, building blocks, and molecular structures, collectively making up the biochemical pathways that constitute human metabolism.

Human health hinges on the plasticity of cellular metabolism in response to changing conditions. On short time scales, our cells cycle their metabolic activity based on our fed/fasted state, exercise intensity, and circadian rhythms. Metabolism also fluctuates in response to inputs including availability of specific nutrients, body temperature, and hormones [2]. These signals and regulation vary by tissue type and the cell's microenvironment. On longer time scales, baseline metabolism will be further tuned by diet composition, lifestyle, and age. If metabolic programming becomes dysregulated, it can result in diseases such as obesity, diabetes, cardiopathies, and liver disease [2].

1.1.2 | Mitochondria and mitochondrial signaling

Mitochondria are central to eukaryotic metabolism. Mitochondria metabolize carbohydrates, amino acids, and fatty acids into common metabolic intermediates. These intermediates are then utilized by the tricarboxylic acid (TCA) cycle and oxidative phosphorylation (OXPHOS) to produce the cell's energetic currency, ATP. A typical cell can consume and replenish one billion ATP molecules every minute, with as much as 90% of those ATP molecules being generated in the mitochondria [3, 4]. This organelle is therefore central to metabolic regulation.

Though mitochondria evolved from an independent prokaryotic ancestor, 1.5 billion years of endosymbiotic evolution has resulted in extensive crosstalk between mitochondria and the rest of the cell. Most mitochondrial proteins are encoded by the nuclear genome. The mitochondrial proteome is thereby regulated through extra-mitochondrial changes in gene expression, protein transfer, and protein post-translational modifications (PTMs) [5]. Mitochondria also receive input from the cell through metabolite availability, organelle contact sites, and calcium (Ca^{2+}) signaling [6]. In exchange, healthy mitochondria release ATP, NADH/NAD^+, and other metabolites into the cytosol for utilization in enzymatic reactions. Damaged or dysfunctional mitochondria also give off signaling molecules that are sensed by the cell such as reactive oxygen species (ROS). Under conditions of acute damage, mitochondrial release of cytochrome c is the initiating signal for programmed cell death, and free mitochondrial DNA (mtDNA) triggers inflammation and immune signaling by neighboring cells [7, 8]. Through these mechanisms, the mitochondrial network tunes its activity to the needs of the cell or alerts the cell if its function is impaired.

1.2 | Calcium signaling

1.2.1 | Calcium as a messenger molecule

Calcium is the most abundant mineral in the human body [9]. 99% of our calcium is sequestered in bone, but the remaining free calcium ions are also critically important for electrochemical signaling. Calcium ions act as intracellular second messengers, driving physiological processes such as muscle contraction, synaptic activity, blood clotting, and egg fertilization[10, 11, 12]. Under basal conditions, cells maintain an extremely low cytosolic calcium concentration (~100 nM) relative to the extracellular milieu (1-1.5 mM) [13]. This 10,000-15,000 fold concentration gradient enables cells to use rapid calcium influx across the plasma membrane as a spatiotemporal signal in response to stimuli such as hormones, neurotransmitters, or growth factors [14]. During a cytosolic calcium signaling event, calcium concentrations can reach 1-2 µM [15]. Elevated calcium levels trigger downstream signaling events by altering electrochemical gradients, acting as a receptor or channel ligand, or regulating the activity of calcium-binding enzymes. Calcium signaling is an important mechanism by which cells can rapidly integrate extracellular stimuli to downstream effector responses.

Calcium waves must be quickly cleared to enable subsequent signaling events and to prevent toxic precipitate formation. At high concentrations, calcium will precipitate with phosphate groups and fatty acids [16, 17]. Depletion of free phosphate would disrupt nucleotide synthesis, cellular energetics, and kinase signaling. To limit the damaging effects of cytosolic calcium signaling, cells rapidly extrude excess calcium cations back across the plasma membrane or sequester them into organellar compartments. The endoplasmic reticulum (ER) and sarcoplasmic reticulum (SR) networks store calcium in high concentrations, later releasing it as a secondary source of intracellular calcium signaling. Free calcium in the ER ranges from 100 µM to 1 mM, and additional calcium is sequestered by high-capacity calcium-binding proteins [18]. Calcium can also be taken up by mitochondria, the Golgi apparatus, peroxisomes, and endolysosomes [19]. Storage of excess calcium in organelles is an important step in the regulation of cellular calcium signaling.

1.2.2 | Mitochondrial calcium buffering

Mitochondria store and utilize excess calcium in the intermembrane space (IMS) and the matrix. Basal mitochondrial calcium concentrations are similar to cytosolic levels (~100 nM), but concentrations will rise to the micromolar range following a signaling event from the cytosol or ER [10]. Calcium acts as a concentration-dependent effector of mitochondrial membrane potential, enzymatic activity, and cell death signaling [20].

Mitochondria buffer cytosolic calcium levels through formation of calcium phosphate complexes. Calcium buffering occurs when matrix calcium concentrations exceed 10 nmol Ca^{2+}/mg of mitochondrial protein (~1–5 μM) [21]. The slightly alkaline pH of the matrix favors formation of calcium phosphate complexes, whereas the cytosol's neutral pH favors calcium in the dissociated state [10]. Sequestration of calcium ions by soluble polyphosphate polymers minimizes precipitation, but at high calcium levels, calcium phosphate complexes form solid deposits [10]. The composition of these deposits has been experimentally determined by energy-dispersive X-ray spectroscopy, confirming the presence of calcium and phosphate as well as smaller percentages of organic compounds [22, 23]. Mitochondrial calcium phosphate deposits have been observed in a wide variety of cell types with deposit diameters typically ranging from 20-100 nm [23]. The buffering capacity of precipitated calcium phosphate exceeds the free mitochondrial calcium concentration by 100,000-fold [21]. Mitochondrial calcium buffering serves to store large amounts of cellular calcium while maintaining organellar sensitivity to small changes in cytosolic calcium fluxes.

1.2.3 | Calcium regulation of mitochondrial health and metabolism

Changes in calcium concentration regulate mitochondrial protein function and metabolic output. Many of the known mitochondrial calcium-binding proteins contain a conserved Ca^{2+} binding motif called an EF-hand. The helix-loop-helix structure of the EF-hand mediates conformational changes upon calcium binding. In the IMS, calcium is bound by the EF-hand-containing proteins mtGPDH, AGC1/2, SCaMC1/2/3/L1, MICU1/2, and LETM1 [24]. Through these proteins, calcium signaling regulates the production of $FADH_2$ and transport of aspartate, glutamate, ATP, P_i, K^+, H^+, and Ca^{2+} across the inner mitochondrial membrane (IMM). However, the best-appreciated mitochondrial pathway activated by calcium is the TCA cycle. Three of the TCA cycle-associated dehydrogenases – pyruvate dehydrogenase (PDH), isocitrate dehydrogenase (IDH), and oxoglutarate dehydrogenase (OGDH) – are stimulated by calcium signaling in the mitochondrial matrix [25]. In the presence of mitochondrial calcium signaling, TCA cycle output is increased, yielding additional ATP, carbon intermediates, and high-energy electron carriers for OXPHOS.

The three calcium-sensitive TCA cycle dehydrogenases have distinct mechanisms of regulation. IDH and OGDH bind calcium directly – though they do not have EF-hand motifs – whereas PDH is indirectly regulated by the pyruvate dehydrogenase phosphatase (PDP) [26]. Calcium-bound PDP has increased phosphatase activity, which reverses the inhibitory modifications of the E1α subunit of PDH [10]. Calcium-binding to IDH and

OGDH increases the enzymes' affinity for their substrates, thereby accelerating their reaction rates. These proteins have different calcium sensitivities (OGDH > PDH > IDH) which vary based on ATP/ADP ratios, but they are generally stimulated by calcium concentrations in the range of 100 nM to 2 μM [25, 27]. With basal calcium concentrations in the matrix resting at ~100 nM, maximal stimulation only occurs during transient calcium signaling events, making the TCA cycle sensitive to extramitochondrial cues. Because TCA cycle flux is intricately tied to ATP production, ROS generation, and the metabolism of amino acids, lipids, and nucleic acids, calcium stimulation of TCA cycle enzymes has broad implications for cellular metabolism and growth [10].

Finally, mitochondrial calcium is a regulator of cell death via the mitochondrial permeability transition pore (mPTP). Opening of the mPTP non-selectively releases low molecular weight substances from the mitochondria when the calcium retention capacity of the matrix has been exceeded [28]. This can occur transiently as a means of protecting mitochondria against oxidative damage, but irreversible opening of the pore under pathologic calcium or ROS overload results in loss of the mitochondrial membrane potential ($\Delta\Psi_m$), OXPHOS uncoupling, rupture of the outer mitochondrial membrane (OMM), and release of pro-apoptotic proteins [28]. Calcium signaling therefore has pleiotropic effects on mitochondrial health; elevated calcium stimulates central metabolic pathways, but excessive calcium impairs respiration and can induce apoptotic or necrotic cell death [29].

1.2.4 | Regulators of mitochondrial influx and efflux

The divalent charge of calcium ions prevents their free diffusion across the outer and inner mitochondrial membranes. Calcium transport is therefore mediated by proteins in the OMM and IMM. VDAC proteins facilitate calcium flux across the OMM, and they are often positioned in proximity to ER contact sites which enhances mitochondrial sensitivity to local calcium concentration changes driven by ER calcium release [30, 17]. Bulk calcium influx across the IMM is dependent on the mitochondrial calcium uniporter complex (mtCU). The transmembrane portion of the mtCU is comprised of a tetrameric complex of MCU proteins which form the calcium-selective pore structure and four EMRE proteins which are also essential for calcium uptake [31 32]. Calcium flux through the mtCU is regulated by incorporation of the additional components such as MCUB and by the gatekeeping proteins MICU1/2/3 [10]. Calcium uptake through the mtCU is driven by the mitochondrial membrane potential ($\Delta\Psi_m$ = -180 mV) and is stimulated by local increases in calcium concentration which are sensed by MICU1/2 [10]. Calcium efflux from the matrix is primarily regulated by the Na^+/Ca^{2+} exchanger NCLX, though LETM1 may be another transporter that allows calcium to leave the matrix. Both ion exchangers typically support calcium efflux, but their activity can be reversible under certain conditions which may explain how MCU-deficient mitochondria maintain low levels of calcium [10, 31]. Collectively, these proteins – in combination with calcium buffering mechanisms – regulate the calcium concentration inside mitochondrial compartments and couple it to cellular calcium signaling.

1.2.5 | Phenotypes associated with altered mitochondrial calcium flux

Genetic modulation of MCU is sufficient to impair calcium-regulated processes in the matrix, resulting in downstream metabolic vulnerabilities. Cells with MCU knocked down have reduced PDH, IDH, and OGDH enzymatic activity and lower NADH/NAD$^+$ ratios [31 33 34, 35]. Consistent with suppressed TCA cycle flux, MCU-deficient cells also have lower levels of ATP [33]. MCU-/- mice are slightly smaller than WT mice but otherwise appear to have mostly normal physiology and have only minor alterations in their basal respiration [31]. Similar observations were made of EMRE -/- mice [36]. However, MCU -/- mice exhibit exercise intolerance compared to WT mice, and MCU is required for sufficient ATP production to fuel increased sinoatrial node activity and elevated heart rate. [31, 37]. This indicates that rapid calcium influx into the matrix is dispensable under resting conditions but is important during conditions of stress and high energetic demand.

There are no known heritable mutations in the mtCU pore-forming proteins MCU or MCUB associated with human disease, however alterations in mtCU function have been reported to have pathologic implications. High fat diet-induced obesity, diabetes, and other metabolic disorders are associated with changes in mtCU protein expression or activity [38, 39, 40]. MtCU function also contributes to development of neural circuitry and memory, and mitochondrial calcium overload has been observed across neurodegenerative disorders including Alzheimer's disease, Parkinson’s disease, Huntington’s disease, and amyotrophic lateral sclerosis (ALS) [10, 41, 42]. Furthermore, loss-of-function mutations in MICU1 or MICU2 lead to lethargy and muscle weakness or neurodevelopmental issues, respectively [43, 44, 45, 46, 47, 48].

The reported role of the mtCU differs across cancer types, but many solid tumors exhibit increases in mtCU activity. Increased mitochondrial calcium signaling has been observed in breast cancer [49, 50, 51], hepatocellular carcinoma [33, 52], pancreatic cancer [53], and colorectal cancer [54, 55, 56]. Moreover, high MCU expression can promote tumor cell migration and invasion and has been correlated with poor patient prognosis [33, 49, 50, 53, 57]. Elevated mitochondrial calcium is thought to support cancer growth through increased metabolic activity, pro-survival signaling, and local immunosuppression [15]. However, this must be balanced against the mitochondrial calcium-mediated initiation of cell death pathways. Hence, it is not surprising that many tumors with increased mitochondrial calcium also have increased expression of anti-apoptotic genes [15]. Averting calcium-induced cell death may also explain why certain cancers conversely appear to benefit from downregulation of mitochondrial calcium influx [58, 59]. Further work is needed to define the specific tumorigenic conditions which favor mtCU activation or suppression and to identify mitochondrial processes affected by altered calcium signaling.

1.3 | Utilization of branched-chain amino acids

1.3.1 | Importance of branched-chain amino acids

In the following chapter, it is demonstrated that changes in mitochondrial calcium signaling have downstream effects on the catabolism of branched-chain amino acids (BCAAs). BCAA is the collective term for leucine, valine, and isoleucine. These are three of the nine essential amino acids which humans must obtain from their diet as they cannot be synthesized *de novo*. Once in the body, BCAAs undergo one of two fates – catabolism into carbon- and nitrogen-based metabolites or incorporation into protein synthesis. The frequency of leucine, valine, and isoleucine incorporation into eukaryotic protein sequences are 10%, 6%, and 5%, respectively, making leucine the most abundantly encoded of the 20 amino acids [60]. The three BCAAs are particularly hydrophobic residues. Their hydrophobicity contributes to the formation of α-helix and β-sheet secondary structures and promotes protein folding of the non-aqueous interior of globular proteins [61]. BCAAs are also enriched in transmembrane domains spanning membrane lipid bilayers [62]. Given their essential nature and their importance for protein structure, BCAA utilization and breakdown must be tightly regulated to conserve these limited resources within the cell.

1.3.2 | BCAA catabolism

The multistep catabolic pathways of the three BCAAs generate important biochemical intermediates which can be utilized in a number of critical energetic processes. The amino groups are used to synthesize glutamate, which can be further converted into other amino acids or nucleotides. BCAA-derived carbons are then processed by a series of enzymes into acetoacetate, acetyl-CoA and/or succinyl-CoA for use in the TCA cycle or as precursors for the synthesis of glucose, fatty acids, or ketone bodies. Additionally, BCAA catabolism regenerates multiple NADH and $FADH_2$ molecules [63]. However, build-up of some catabolic intermediates is toxic, and genetic defects in certain BCAA catabolism enzymes are known to cause diseases. These include maple syrup urine disease, sweaty feet syndrome, propionic acidemia, and methylmalonic acidemia [2]. The pathologies associated with disorders of BCAA catabolism suggest that it is critical for the body to maintain coordinated regulation of the multiple enzymatic steps of catabolism while maximizing the energetic potential from these three amino acids.

The initial two steps of catabolism are shared by all three BCAAs and are key points of pathway regulation. First, BCAAs undergo reversible transamination by BCAT1 in the cytosol or BCAT2 in the mitochondria to produce glutamate and the three corresponding keto-acids. The enzymatic steps downstream of BCAT1/2 are all carried out exclusively in the mitochondria. The second reaction is the first non-reversible and therefore committed step of the pathway. This is carried out by the BCKDH complex. Because the BCAT and BCKDH enzymes act on all three BCAAs, catabolism rates are generally synchronized between leucine, valine, and isoleucine, despite having divergent downstream reactions and end-products [62].

1.3.3 | Cellular and systemic regulation of BCAAs

At the cellular level, the BCAA catabolism pathway is regulated transcriptionally and post-translationally. Multiple metabolic and hormonal cues including starvation, insulin, glucagon, adrenaline, cortisol, and BCAA availability converge through transcription factor regulation to tune the expression of BCAA catabolism enzymes [61]. Additionally, allosteric end-product inhibition by NADH and the branch-chain acyl-CoA esters directly regulates the committed step performed by the BCKDH complex [61, 64]. BCKDH is further inhibited by phosphorylation of the E1α subunit. BCKDH-E1α modification is regulated by the opposing activities of the BCKDK kinase and PPM1K phosphatase. BCKDK is inhibited by allosteric interactions with branched-chain α-keto-acids (BCKAs) [64]. This dual regulation results in active BCKDH complex in the presence of abundant upstream reactants from BCAT1/2 and less active BCKDH complex when its end-product concentrations are high.

Regulation of systemic BCAA concentrations takes place through absorption and catabolism across multiple tissues. BCAA catabolism occurs primarily in liver, skeletal muscle, kidney, and adipose tissue [2]. Upon initial absorption into the bloodstream, BCAAs bypass first-pass hepatic metabolism due to low expression of BCAT1/2 proteins in the liver [65]. BCAAs are instead taken up by liver and skeletal muscle and stored in proteins [66]. This lowers the levels of circulating BCAAs and their corresponding BCKAs which become cardio- and neurotoxic in high concentrations [67]. To initiate catabolism, deamination of BCAAs into their respective BCKAs is carried out in skeletal muscle and adipose tissues, and the BCKAs are transferred to the liver for the remainder of the catabolic process [68, 69]. Amino acid-derived ammonia is also processed and cleared by the liver through the urea cycle. Because liver is a primary site of BCAA storage, catabolism, and ammonia clearance, hepatocyte regulation of these pathways can have systemic effects on metabolism and amino acid availability.

1.4 | Fibrolamellar carcinoma

1.4.1 | Fibrolamellar carcinoma patients and pathologies

Fibrolamellar carcinoma (FLC) is a rare form of liver cancer found in adolescents and young adults. The annual incidence of FLC is estimated to be between 0.02 and 0.185 per 100,000 individuals in the United States [70]. The peak age range at diagnosis is 15 to 19 years with no significant differences in ethnic or geographic prevalence [70, 71]. As with other abdominal cancers, patients typically present with weight loss (25-30%), abdominal pain (21-74%), and/or an abdominal mass or hepatomegaly (15-40%) [72]. FLC does not present secondary to other liver diseases, and there are no known risk factors. Due to a paucity of symptoms early in FLC progression, diagnosis often comes only after the primary tumor is 10-12 cm in diameter and 30-40% of patients have distant metastases [73]. Though FLC is rare, this cancer has a high burden of disease given the early age of onset and severity of disease at diagnosis.

Late diagnosis and metastases pose a challenge as surgical resection remains the standard treatment for FLC. More than 50% of FLC patients see recurrence within 10-33 months after surgery [74]. Even patients who received a liver transplant were reported to have a 5-year survival rate of only 48% [73]. For patients with disseminated disease or those who do not receive surgery, the 5-year survival is below 20% [73]. There remains a need for better diagnostic tools and targeted treatment strategies to improve clinical outcomes for these patients.

FLC has unique pathologic features that distinguish it from classical hepatocellular carcinoma (HCC). First, the young age and lack of prior liver disease in FLC patients contrasts with most HCC patients. HCC has an average age of presentation of 65 years, and more than 90% of cases are associated with preexisting chronic liver disease [75, 76]. Second, FLC tumors are characterized by distinct lamellated fibers of collagen (giving it the name fibrolamellar carcinoma). ~70% of primary tumors also have a central scar involving calcifications, while these features are rarely observed in HCC [77]. Histologically, FLC tumors present with large cells, prominent nucleoli, and an abundance of eosinophilic mitochondria [75]. FLC tumors have relative chromosome stability and lack many of the genetic mutations commonly associated with HCC tumors [73, 75]. Though FLC was initially classified as a subtype of HCC [78], it is now generally considered to be a distinct diagnosis, requiring a unique treatment plan.

1.4.2 | Molecular underpinnings of FLC – DNAJ-PKAc fusion

Though FLC is not associated with typical oncogenic mutations in tumor activator or suppressor genes, it is characterized by a novel fusion protein. This fusion protein is the result of a *de novo*, in-frame deletion of ~400 kb in chromosome 19 which was first described in 2014 [79]. The precise chromosome breakpoints vary across patients, with the predominant outcome being a chimeric transcript encoding exon 1 of *DNAJB1* and exons 2-10 of *PRKACA*. The resulting fusion protein, DNAJ-PKAc (hereon referred to as DP), consists of the HSP70-interacting J-domain of an Hsp40 protein and the catalytic subunit of the protein kinase A (PKAc). Mice bearing the equivalent deletion and DP fusion protein developed liver tumors with similar pathology to FLC, indicating that this mutation is sufficient for oncogenesis [80]. The ~400 kb deletion also results in heterozygous loss of 8 coding genes (ASF1B, ADGRL1, RN7SL231P, ADGRES, DDX39A, PTGER1, GIPC1 and PKN1) and 4 putative genes (ENSG00000160251, ENSG00000224543, ENSG00000266913, ENSG00000267474) [71]. However, expression levels of these transcripts are not significantly altered by the deletion [81, 82]. Similar phenotypes are observed when DP is over-expressed as when the chromosome 19 deletion is replicated by CRISPR/Cas9 editing, suggesting that DP is the driver of FLC pathology, not the heterozygous loss of the genes flanked by *DNAJB1 and PRKACA* [71, 83, 84]. As such, DP expression is now considered to be a key feature of FLC.

The DP fusion protein distinguishes FLC from other types of liver cancer. DP was not detected in patients diagnosed with conventional HCC, scirrhous HCC, cholangiocarcinoma, hepatic adenoma, or hepatoblastoma [85]. This specificity has made DP a useful diagnostic screening tool for differentiating FLC from other tumors with similar presentation. However, DP is not unique to FLC, as it has also been detected in a small number of patients with pancreatobiliary neoplasms [86]. It remains unknown why DP-expressing cancers arise primarily in the hepato-pancreato-biliary system.

FLC is part of a larger family of cancers which have mutations or amplifications of PKA-related genes. Pancreatobiliary tumors have been reported to contain *ATPB1::PRKACA and ATPB1::PRKACB* chimeras, affecting the α and β catalytic subunits of PKA, respectively [87]. *GATA2A::PRKACA*, *TPGS1::PRKACA*, and *ASF1B::PRKACA* have also been detected in various cancer types tracked by The Cancer Genome Atlas (TCGA) [86]. Wild-type (WT) *PRKACA* is amplified in 12% of ovarian serous cystadenocarcinoma cases, 5% of uterine corpus endometrial carcinoma cases, and ≤3% of adenoid cystic carcinoma, lung squamous cell carcinoma, sarcoma, and breast invasive carcinoma cases [79]. This suggests that PKAc over-expression, even in the absence of a chimera, can support oncogenic signaling. Similarly, cancers can present with loss-of-function mutations in the regulatory subunits of PKA, supporting increased PKA signaling in these tumors [88, 89, 90]. Together, these tumor alterations in PKA expression indicate that PKA signaling contributes to cancer growth or survival.

This raises the question of how PKA-activating mutations in general and the DP fusion protein specifically contributes to oncogenesis and cancer progression. WT PKA kinase signaling is tightly controlled through binding of its regulatory subunits, cAMP-dependent activation, and AKAP-mediated spatial constraints. Loss of any of these regulatory mechanisms could support cancer, as many of the pathways downstream of PKA phosphorylation are involved in growth, development, and metabolism. Increased PKA activity is associated with cancer EMT, migration and invasion [91]. In FLC, DP is over-expressed at the mRNA and protein levels compared to the WT copy of PKAc [92]. This is likely the combined effect of increased transcription rate at the *DNAJB1* promoter and increased mRNA and/or protein stability of the fusion. DP has a similar affinity for cAMP as WT PKAc, and it retains its ability to bind PKA regulatory subunits [74, 93]. However, studies on the protein interactome of DP show reduced interaction with certain AKAPs and increased J-domain-mediated interactions with Hsp70 and the anti-apoptotic signaling protein BAG2 [94]. The downstream result is altered PKA and ERK kinase signaling and cell resistance to apoptosis. DP catalytic activity is required for these signaling changes and for oncogenesis, yet *PRKACA* over-expression is insufficient to model FLC, suggesting that the J-domain also plays an important role in pathogenesis [83 94, 95]. Though the immediate phosphorylation substrates and protein interactors of DP have been identified [92, 94], further work is required to elucidate the downstream effects of the altered PKA activity in FLC and to understand their relative contributions to tumorigenesis.

1.4.3 | Mitochondrial changes in FLC

FLC tumors are characterized by increased mitochondrial abundance. Early electron microscopy analysis of patient tumors showed enlarged cells with a mitochondria-rich cytoplasm [96, 97, 98]. This observation aligns with the pathology classification of FLC as an oncocytic cancer. Oncocytic tumors are defined by a granular, eosinophilic cytoplasm, indicative of an accumulation of mitochondria. Though oncocytic tumors have been observed in most tissue types, they are rare and most often associated with cancers of the thyroid, kidney, or salivary and pituitary glands [96]. Classical HCC does not generally present with oncocytic cells. This phenotype is, therefore, another feature that distinguishes FLC from classical HCC.

Along with increased mitochondrial abundance, early electron micrographs of FLC tumor cells showed electron-dense, granular particles in a high number of mitochondria [98]. These precipitates are consistent in appearance and size with mitochondrial calcium phosphate deposits [23, 29]. The presence of deposits is suggestive of mitochondrial calcium overload, however it has yet to be demonstrated whether FLC mitochondria have increased concentrations of free calcium and whether this has implications for mitochondrial function in these tumors.

1.4.4 | KLF15 transcription factor

The zinc-finger transcription factor KLF15 plays an important role in the regulation of BCAA catabolism and other metabolic processes. KLF15 is expressed at high levels in metabolically active tissues including liver, heart, kidney, pancreas, skeletal muscle, and adipose tissue [99, 100]. In these tissues, KLF15-mediated transcription of metabolic genes supports gluconeogenesis, amino acid catabolism, urea cycle, and fatty acid oxidation (FAO) [101, 102, 103, 104]. Notably, KLF15 levels correlate with transcription of the BCAA catabolism pathway genes BCAT2, BCKDHA, PPM1K, and IVD [105, 106]. Correspondingly, leucine and valine serum concentrations are increased in KLF15 -/-

mice [104]. KLF15 is therefore an important point of regulation for multiple metabolic pathways including BCAA catabolism.

1.4.5 | Potential Roles of KLF15 in FLC pathology

A reduction in KLF15-mediated transcription can have several pathological downstream effects. Decreased levels of KLF15 contribute to cardiac hypertrophy in heart failure patients [100]. Additionally, downregulation of KLF15 in the heart or kidney results in fibrosis [107, 108, 109]. In the liver, KLF15 is essential for ornithine transcarbamylase (OTC) expression and activity in the urea cycle, and KLF15 -/- mice have elevated ammonia and decreased urea concentrations in their urine [103]. Furthermore, KLF15 contributes to tissue differentiation and maturation and is sufficient to slow the proliferation of hepatoblasts [110, 111]. Loss of KLF15 expression is then associated with pluripotency and oncogenicity [99]. In the following chapter, it is demonstrated that KLF15 protein levels are reduced in FLC tumors. As the literature has shown that loss of KLF15 accelerates proliferation, promotes collagen formation, and impairs the urea cycle – all phenotypes observed in FLC [82, 112, 113] – I propose that KLF15 likely plays an important role in altering FLC metabolism.

1.5 | Open questions that inspired this work

1.5.1 | Novel roles of uniporter-mediated calcium signaling

There are numerous pathways speculated to be regulated by calcium signaling in the mitochondria, yet it remains to be elucidated how mitochondrial calcium performs some of these functions. The majority of validated calcium-binding proteins in the mitochondria are EF-hand containing proteins responsive to cytosolic or IMS calcium levels [24, 114], with few known calcium-binding proteins localized in the matrix [25, 115]. Influx and efflux of calcium in the matrix is tightly regulated [10], yet relatively little is known about the signaling effects of calcium in the mitochondrial matrix. To screen for pathways affected by calcium signaling in the mitochondrial matrix, I performed proteomics and transcriptomics analysis comparing WT and MCU KO cells. This led to the identification of BCAA catabolism as a novel MCU-regulated pathway. I demonstrate that BCAA catabolism is stimulated transcriptionally and through activation of the committed enzymatic step when calcium signaling is abolished in the matrix. This work reaffirms that calcium influx into the matrix has broader functions beyond stimulation of the TCA cycle or triggering cell death.

1.5.2 | Mitochondrial alterations in FLC

Metabolic reprogramming is a central hallmark of cancer which implicates mitochondria [116]. Recent work on understanding the drivers of FLC pathology have demonstrated changes in mitochondrial metabolism and dynamics [84, 117], however it remains to be elucidated how these changes are related to the DP fusion protein and whether these metabolic shifts are important for cancer progression. Existing research has also yet to investigate the role of oncocytic transformation of FLC cells. And though it was speculated early on that these abundant mitochondria may contain excess calcium [98], verification of this hypothesis is still needed. In Chapter 2, I replicate and quantify the finding of calcium phosphate deposits in FLC tumor mitochondria as well as measure elevated concentrations of free calcium in DP-expressing cells. This work proves that FLC tumors and DP-expressing cells exhibit mitochondrial calcium overload and further demonstrates that increased calcium signaling is important for the regulation of amino acid metabolism and ammonia clearance. These metabolic changes downstream of uniporter-regulated calcium signals likely contribute to several FLC cellular phenotypes and could be leveraged in future pharmacologic treatments for this cancer.

1.6 | References

1. Hołyst, R. *et al.* Living Cell as a Self-Synchronized Chemical Reactor. *J Phys Chem Lett* **15**, 3559–3570 (2024).
2. Judge, A. & Dodd, M. S. Metabolism. *Essays Biochem* **64**, 607–647 (2020).
3. Alberts, B. *et al. Molecular Biology of the Cell.* (Garland Science, New York, 2002).
4. Javadov, S., Kozlov, A. V & Camara, A. K. S. Mitochondria in Health and Diseases. *Cells* **9**, (2020).
5. Walker, B. R. & Moraes, C. T. Nuclear-Mitochondrial Interactions. *Biomolecules* **12**, (2022).
6. Messina, M., Vaz, F. M. & Rahman, S. Mitochondrial membrane synthesis, remodelling and cellular trafficking. *J Inherit Metab Dis* (2024) doi:10.1002/jimd.12766.
7. Andreyev, A. & Fiskum, G. Calcium induced release of mitochondrial cytochrome c by different mechanisms selective for brain versus liver. *Cell Death Differ* **6**, 825–32 (1999).
8. Hong, Q. *et al.* The emerging role of mtDNA release in sepsis: Current evidence and potential therapeutic targets. *J Cell Physiol* (2024) doi:10.1002/jcp.31331.
9. *Diet and Health: Implications for Reducing Chronic Disease Risk.* (National Academy Press, Washington, D.C., 1989).
10. Garbincius, J. F. & Elrod, J. W. Mitochondrial calcium exchange in physiology and disease. *Physiol Rev* **102**, 893–992 (2022).
11. LeBrasseur, N. Calcium for strong clotting. *J Cell Biol.* **160**, 980 (2003).
12. Sugita, H., Takarabe, S., Kageyama, A., Kawata, Y. & Ito, J. Molecular Mechanism of Oocyte Activation in Mammals: Past, Present, and Future Directions. *Biomolecules* **14**, (2024).

13. Rizzuto, R. & Pozzan, T. Microdomains of intracellular Ca2+: molecular determinants and functional consequences. *Physiol Rev* **86**, 369–408 (2006).

14. Alhajeri, M. M., Alkhanjari, R. R., Hodeify, R., Khraibi, A. & Hamdan, H. Neurotransmitters, neuropeptides and calcium in oocyte maturation and early development. *Front Cell Dev Biol* **10**, 980219 (2022).

15. Marchi, S., Giorgi, C., Galluzzi, L. & Pinton, P. Ca2+ Fluxes and Cancer. *Mol Cell* **78**, 1055–1069 (2020).

16. Clapham, D. E. Calcium signaling. *Cell* **131**, 1047–58 (2007).

17. Jin, C., Kumar, P., Gracia-Sancho, J. & Dufour, J.-F. Calcium transfer between endoplasmic reticulum and mitochondria in liver diseases. *FEBS Lett* **595**, 1411–1421 (2021).

18. Eisner, D., Neher, E., Taschenberger, H. & Smith, G. Physiology of intracellular calcium buffering. *Physiol Rev* **103**, 2767–2845 (2023).

19. Prins, D. & Michalak, M. Organellar calcium buffers. *Cold Spring Harb Perspect Biol* **3**, (2011).

20. Cannino, G., Ciscato, F., Masgras, I., Sánchez-Martín, C. & Rasola, A. Metabolic Plasticity of Tumor Cell Mitochondria. *Front Oncol* **8**, 333 (2018).

21. Chalmers, S. & Nicholls, D. G. The relationship between free and total calcium concentrations in the matrix of liver and brain mitochondria. *J Biol Chem* **278**, 19062–70 (2003).

22. Weinbach, E. C. & Von Brand, T. Formation, isolation and composition of dense granules from mitochondria. *Biochim Biophys Acta* **148**, 256–66 (1967).

23. Wolf, S. G. *et al.* 3D visualization of mitochondrial solid-phase calcium stores in whole cells. *Elife* **6**, (2017).

24. Hajnóczky, G. *et al.* Reliance of ER-mitochondrial calcium signaling on mitochondrial EF-hand Ca2+ binding proteins: Miros, MICUs, LETM1 and solute carriers. *Curr Opin Cell Biol* **29**, 133–41 (2014).

25. Denton, R. M. Regulation of mitochondrial dehydrogenases by calcium ions. *Biochim Biophys Acta* **1787**, 1309–16 (2009).

26. Bustos, G. *et al.* The ER-mitochondria Ca2+ signaling in cancer progression: Fueling the monster. *Int Rev Cell Mol Biol* **363**, 49–121 (2021).

27. Hansford, R. G. Dehydrogenase activation by Ca2+ in cells and tissues. *J Bioenerg Biomembr* **23**, 823–54 (1991).

28. Endlicher, R., Drahota, Z., Štefková, K., Červinková, Z. & Kučera, O. The Mitochondrial Permeability Transition Pore-Current Knowledge of Its Structure, Function, and

Regulation, and Optimized Methods for Evaluating Its Functional State. *Cells* **12**, (2023).

29. Strubbe-Rivera, J. O. *et al.* The mitochondrial permeability transition phenomenon elucidated by cryo-EM reveals the genuine impact of calcium overload on mitochondrial structure and function. *Sci Rep* **11**, 1037 (2021).
30. Rosencrans, W. M., Rajendran, M., Bezrukov, S. M. & Rostovtseva, T. K. VDAC regulation of mitochondrial calcium flux: From channel biophysics to disease. *Cell Calcium* **94**, 102356 (2021).
31. Pan, X. *et al.* The physiological role of mitochondrial calcium revealed by mice lacking the mitochondrial calcium uniporter. *Nat Cell Biol* **15**, 1464–72 (2013).
32. Sancak, Y. *et al.* EMRE is an essential component of the mitochondrial calcium uniporter complex. *Science* **342**, 1379–82 (2013).
33. Ren, T. *et al.* MCU-dependent mitochondrial Ca2+ inhibits NAD+/SIRT3/SOD2 pathway to promote ROS production and metastasis of HCC cells. *Oncogene* **36**, 5897–5909 (2017).
34. Young, M. P. *et al.* Metabolic adaptation to the chronic loss of Ca2+ signaling induced by KO of IP3 receptors or the mitochondrial Ca2+ uniporter. *J Biol Chem* **298**, 101436 (2022).
35. Balderas, E. *et al.* Mitochondrial calcium uniporter stabilization preserves energetic homeostasis during Complex I impairment. *Nat Commun* **13**, 2769 (2022).
36. Liu, J. C. *et al.* EMRE is essential for mitochondrial calcium uniporter activity in a mouse model. *JCI Insight* **5**, (2020).
37. Wu, Y. *et al.* The mitochondrial uniporter controls fight or flight heart rate increases. *Nat Commun* **6**, 6081 (2015).
38. Arruda, A. P. *et al.* Chronic enrichment of hepatic endoplasmic reticulum-mitochondria contact leads to mitochondrial dysfunction in obesity. *Nat Med* **20**, 1427–35 (2014).
39. Vecellio Reane, D., Serna, J. D. C. & Raffaello, A. Unravelling the complexity of the mitochondrial Ca2+ uniporter: regulation, tissue specificity, and physiological implications. *Cell Calcium* **121**, 102907 (2024).
40. Ghosh, S. *et al.* MCU-complex-mediated mitochondrial calcium signaling is impaired in Barth syndrome. *Hum Mol Genet* **31**, 376–385 (2022).
41. König, T. *et al.* The m-AAA Protease Associated with Neurodegeneration Limits MCU Activity in Mitochondria. *Mol Cell* **64**, 148–162 (2016).
42. Walters, G. C. & Usachev, Y. M. Mitochondrial calcium cycling in neuronal function and neurodegeneration. *Front Cell Dev Biol* **11**, 1094356 (2023).

43. Logan, C. V *et al.* Loss-of-function mutations in MICU1 cause a brain and muscle disorder linked to primary alterations in mitochondrial calcium signaling. *Nat Genet* **46**, 188–93 (2014).

44. Lewis-Smith, D. *et al.* Homozygous deletion in MICU1 presenting with fatigue and lethargy in childhood. *Neurol Genet* **2**, e59 (2016).

45. O'Grady, G. L. *et al.* Diagnosis and etiology of congenital muscular dystrophy: We are halfway there. *Ann Neurol* **80**, 101–11 (2016).

46. Mojbafan, M. *et al.* Reporting a rare form of myopathy, myopathy with extrapyramidal signs, in an Iranian family using next generation sequencing: a case report. *BMC Med Genet* **21**, 77 (2020).

47. Wilton, K. M. *et al.* Developmental brain abnormalities and acute encephalopathy in a patient with myopathy with extrapyramidal signs secondary to pathogenic variants in MICU1. *JIMD Rep* **53**, 22–28 (2020).

48. Shamseldin, H. E. *et al.* A null mutation in MICU2 causes abnormal mitochondrial calcium homeostasis and a severe neurodevelopmental disorder. *Brain* **140**, 2806–2813 (2017).

49. Curry, M. C., Peters, A. A., Kenny, P. A., Roberts-Thomson, S. J. & Monteith, G. R. Mitochondrial calcium uniporter silencing potentiates caspase-independent cell death in MDA-MB-231 breast cancer cells. *Biochem Biophys Res Commun* **434**, 695–700 (2013).

50. Tosatto, A. *et al.* The mitochondrial calcium uniporter regulates breast cancer progression via HIF-1α. *EMBO Mol Med* **8**, 569–85 (2016).

51. Yu, C. *et al.* Mitochondrial calcium uniporter as a target of microRNA-340 and promoter of metastasis via enhancing the Warburg effect. *Oncotarget* **8**, 83831–83844 (2017).

52. Jin, M. *et al.* MCUR1 facilitates epithelial-mesenchymal transition and metastasis via the mitochondrial calcium dependent ROS/Nrf2/Notch pathway in hepatocellular carcinoma. *J Exp Clin Cancer Res* **38**, 136 (2019).

53. Wang, X. *et al.* Mitochondrial Calcium Uniporter Drives Metastasis and Confers a Targetable Cystine Dependency in Pancreatic Cancer. *Cancer Res* **82**, 2254–2268 (2022).

54. Liu, Y. *et al.* MCU-induced mitochondrial calcium uptake promotes mitochondrial biogenesis and colorectal cancer growth. *Signal Transduct Target Ther* **5**, 59 (2020).

55. Zeng, F. *et al.* RIPK1 Binds MCU to Mediate Induction of Mitochondrial Ca2+ Uptake and Promotes Colorectal Oncogenesis. *Cancer Res* **78**, 2876–2885 (2018).

56. Zhu, J. *et al.* miR-138-5p targets MCU to inhibit mitochondrial biogenesis and colorectal cancer growth. *J Cell Mol Med* **27**, 2112–2122 (2023).

57. Hall, D. D., Wu, Y., Domann, F. E., Spitz, D. R. & Anderson, M. E. Mitochondrial calcium uniporter activity is dispensable for MDA-MB-231 breast carcinoma cell survival. *PLoS One* **9**, e96866 (2014).

58. Colussi, D. M. & Stathopulos, P. B. The mitochondrial calcium uniporter: Balancing tumourigenic and anti-tumourigenic responses. *J Physiol* **602**, 3315–3339 (2024).

59. Xie, K.-F., Guo, D.-D. & Luo, X.-J. SMDT1-driven change in mitochondrial dynamics mediate cell apoptosis in PDAC. *Biochem Biophys Res Commun* **511**, 323–329 (2019).

60. Bogatyreva, N. S., Finkelstein, A. V & Galzitskaya, O. V. Trend of amino acid composition of proteins of different taxa. *J Bioinform Comput Biol* **4**, 597–608 (2006).

61. Bifari, F. & Nisoli, E. Branched-chain amino acids differently modulate catabolic and anabolic states in mammals: a pharmacological point of view. *Br J Pharmacol* **174**, 1366–1377 (2017).

62. Brosnan, J. T. & Brosnan, M. E. Branched-chain amino acids: enzyme and substrate regulation. *J Nutr* **136**, 207S–11S (2006).

63. Choi, B. H., Hyun, S. & Koo, S.-H. The role of BCAA metabolism in metabolic health and disease. *Exp Mol Med* (2024) doi:10.1038/s12276-024-01263-6.

64. Blair, M. C., Neinast, M. D. & Arany, Z. Whole-body metabolic fate of branched-chain amino acids. *Biochem J* **478**, 765–776 (2021).

65. Lo, E. K. K. *et al.* The Emerging Role of Branched-Chain Amino Acids in Liver Diseases. *Biomedicines* **10**, (2022).

66. Sivanand, S. & Vander Heiden, M. G. Emerging Roles for Branched-Chain Amino Acid Metabolism in Cancer. *Cancer Cell* **37**, 147–156 (2020).

67. Burrage, L. C., Nagamani, S. C. S., Campeau, P. M. & Lee, B. H. Branched-chain amino acid metabolism: from rare Mendelian diseases to more common disorders. *Hum Mol Genet* **23**, R1-8 (2014).

68. Verkerke, A. R. P. *et al.* BCAA-nitrogen flux in brown fat controls metabolic health independent of thermogenesis. *Cell* **187**, 2359-2374.e18 (2024).

69. Platell, C., Kong, S. E., McCauley, R. & Hall, J. C. Branched-chain amino acids. *J Gastroenterol Hepatol* **15**, 706–17 (2000).

70. Zack, T. *et al.* Defining incidence and complications of fibrolamellar liver cancer through tiered computational analysis of clinical data. *NPJ Precis Oncol* **7**, 29 (2023).

71. Lalazar, G. & Simon, S. M. Fibrolamellar Carcinoma: Recent Advances and Unresolved Questions on the Molecular Mechanisms. *Semin Liver Dis* **38**, 51–59 (2018).

72. Ganeshan, D. *et al.* Imaging features of fibrolamellar hepatocellular carcinoma. *AJR Am J Roentgenol* **202**, 544–52 (2014).

73. O’Neill, A. F. *et al.* Fibrolamellar carcinoma: An entity all its own. *Curr Probl Cancer* **45**, 100770 (2021).

74. Riggle, K. M., Turnham, R., Scott, J. D., Yeung, R. S. & Riehle, K. J. Fibrolamellar Hepatocellular Carcinoma: Mechanistic Distinction From Adult Hepatocellular Carcinoma. *Pediatr Blood Cancer* **63**, 1163–7 (2016).

75. Torbenson, M. Fibrolamellar carcinoma: 2012 update. *Scientifica (Cairo)* **2012**, 743790 (2012).

76. Llovet, J. M. *et al.* Hepatocellular carcinoma. *Nat Rev Dis Primers* **7**, 6 (2021).

77. Mamone, G. *et al.* Imaging of calcified hepatic lesions: spectrum of diseases. *Abdom Radiol (NY)* **46**, 2540–2555 (2021).

78. Edmondson, H. A. Differential diagnosis of tumors and tumor-like lesions of liver in infancy and childhood. *AMA J Dis Child* **91**, 168–86 (1956).

79. Honeyman, J. N. *et al.* Detection of a recurrent DNAJB1-PRKACA chimeric transcript in fibrolamellar hepatocellular carcinoma. *Science* **343**, 1010–4 (2014).

80. Engelholm, L. H. *et al.* CRISPR/Cas9 Engineering of Adult Mouse Liver Demonstrates That the Dnajb1-Prkaca Gene Fusion Is Sufficient to Induce Tumors Resembling Fibrolamellar Hepatocellular Carcinoma. *Gastroenterology* **153**, 1662-1673.e10 (2017).

81. Simon, E. P. *et al.* Transcriptomic characterization of fibrolamellar hepatocellular carcinoma. *Proc Natl Acad Sci U S A* **112**, E5916-25 (2015).

82. Turnham, R. E. *et al.* An acquired scaffolding function of the DNAJ-PKAc fusion contributes to oncogenic signaling in fibrolamellar carcinoma. *Elife* **8**, (2019).

83. Kastenhuber, E. R. *et al.* DNAJB1-PRKACA fusion kinase interacts with β-catenin and the liver regenerative response to drive fibrolamellar hepatocellular carcinoma. *Proc Natl Acad Sci U S A* **114**, 13076–13084 (2017).

84. Kim, S. S. *et al.* DNAJB1-PRKACA in HEK293T cells induces LINC00473 overexpression that depends on PKA signaling. *PLoS One* **17**, e0263829 (2022).

85. Graham, R. P. *et al.* DNAJB1-PRKACA is specific for fibrolamellar carcinoma. *Mod Pathol* **28**, 822–9 (2015).

86. Vyas, M. *et al.* DNAJB1-PRKACA fusions occur in oncocytic pancreatic and biliary neoplasms and are not specific for fibrolamellar hepatocellular carcinoma. *Mod Pathol* **33**, 648–656 (2020).

87. Itoh, T. *et al.* Gene Rearrangement and Expression of PRKACA and PRKACB Govern Morphobiology of Pancreatobiliary Oncocytic Neoplasms. *Mod Pathol* **37**, 100358 (2024).

88. Rooper, L. M. *et al.* Low-grade non-intestinal-type sinonasal adenocarcinoma: a histologically distinctive but molecularly heterogeneous entity. *Mod Pathol* **35**, 1160–1167 (2022).

89. Chan, G. K. L. *et al.* Oncogenic PKA signaling increases c-MYC protein expression through multiple targetable mechanisms. *Elife* **12**, (2023).

90. Hirsch, T. Z. *et al.* BAP1 mutations define a homogeneous subgroup of hepatocellular carcinoma with fibrolamellar-like features and activated PKA. *J Hepatol* **72**, 924–936 (2020).

91. Shaikh, D. *et al.* cAMP-dependent protein kinase is essential for hypoxia-mediated epithelial-mesenchymal transition, migration, and invasion in lung cancer cells. *Cell Signal* **24**, 2396–406 (2012).

92. Riggle, K. M. *et al.* Enhanced cAMP-stimulated protein kinase A activity in human fibrolamellar hepatocellular carcinoma. *Pediatr Res* **80**, 110–8 (2016).

93. Cheung, J. *et al.* Structural insights into mis-regulation of protein kinase A in human tumors. *Proc Natl Acad Sci U S A* **112**, 1374–9 (2015).

94. Lauer, S. M. *et al.* Recruitment of BAG2 to DNAJ-PKAc scaffolds promotes cell survival and resistance to drug-induced apoptosis in fibrolamellar carcinoma. *Cell Rep* **43**, 113678 (2024).

95. Shirani, M. *et al.* Increased Protein Kinase A Activity Induces Fibrolamellar Hepatocellular Carcinoma Features Independent of DNAJB1. *Cancer Res* (2024) doi:10.1158/0008-5472.CAN-23-4110.

96. Gasparre, G., Romeo, G., Rugolo, M. & Porcelli, A. M. Learning from oncocytic tumors: Why choose inefficient mitochondria? *Biochim Biophys Acta* **1807**, 633–42 (2011).

97. Craig, J. R., Peters, R. L., Edmondson, H. A. & Omata, M. Fibrolamellar carcinoma of the liver: a tumor of adolescents and young adults with distinctive clinico-pathologic features. *Cancer* **46**, 372–9 (1980).

98. Farhi, D. C., Shikes, R. H. & Silverberg, S. G. Ultrastructure of fibrolamellar oncocytic hepatoma. *Cancer* **50**, 702–9 (1982).

99. McConnell, B. B. & Yang, V. W. Mammalian Krüppel-like factors in health and diseases. *Physiol Rev* **90**, 1337–81 (2010).

100. Fan, L., Hsieh, P. N., Sweet, D. R. & Jain, M. K. Krüppel-like factor 15: Regulator of BCAA metabolism and circadian protein rhythmicity. *Pharmacol Res* **130**, 123–126 (2018).

101. Chen, H., Li, L.-L. & Du, Y. Krüppel-like factor 15 in liver diseases: Insights into metabolic reprogramming. *Front Pharmacol* **14**, 1115226 (2023).

102. Piret, S. E. *et al.* Loss of proximal tubular transcription factor Krüppel-like factor 15 exacerbates kidney injury through loss of fatty acid oxidation. *Kidney Int* **100**, 1250–1267 (2021).

103. Jeyaraj, D. *et al.* Klf15 orchestrates circadian nitrogen homeostasis. *Cell Metab* **15**, 311–23 (2012).

104. Gray, S. *et al.* Regulation of gluconeogenesis by Krüppel-like factor 15. *Cell Metab* **5**, 305–12 (2007).

105. Shao, D. *et al.* Glucose promotes cell growth by suppressing branched-chain amino acid degradation. *Nat Commun* **9**, 2935 (2018).

106. Mehrazad Saber, Z. *et al.* High protein diet-induced metabolic changes are transcriptionally regulated via KLF15-dependent and independent pathways. *Biochem Biophys Res Commun* **582**, 35–42 (2021).

107. Wang, B. *et al.* The Kruppel-like factor KLF15 inhibits connective tissue growth factor (CTGF) expression in cardiac fibroblasts. *J Mol Cell Cardiol* **45**, 193–7 (2008).

108. Tian, Y. *et al.* KLF15 negatively regulates cardiac fibrosis by which SDF-1β attenuates cardiac fibrosis in type 2 diabetic mice. *Toxicol Appl Pharmacol* **427**, 115654 (2021).

109. Mao, L. *et al.* Histone Deacetylase 11 Contributes to Renal Fibrosis by Repressing KLF15 Transcription. *Front Cell Dev Biol* **8**, 235 (2020).

110. Anzai, K. *et al.* Kruppel-like factor 15 induces the development of mature hepatocyte-like cells from hepatoblasts. *Sci Rep* **11**, 18551 (2021).

111. Guo, Y. *et al.* Podocyte-Specific Induction of Krüppel-Like Factor 15 Restores Differentiation Markers and Attenuates Kidney Injury in Proteinuric Kidney Disease. *J Am Soc Nephrol* **29**, 2529–2545 (2018).

112. Nerlich, A. G. *et al.* Excessive collagen formation in fibrolamellar carcinoma of the liver: a morphological and biochemical study. *Mod Pathol* **5**, 580–5 (1992).

113. Sulaiman, R. A. & Geberhiwot, T. Fibrolamellar hepatocellular carcinoma mimicking ornithine transcarbamylase deficiency. *JIMD Rep* **16**, 47–50 (2014).

114. Del Arco, A., Contreras, L., Pardo, B. & Satrustegui, J. Calcium regulation of mitochondrial carriers. *Biochim Biophys Acta* **1863**, 2413–21 (2016).

115. Elnatan, D. & Agard, D. A. Calcium binding to a remote site can replace magnesium as cofactor for mitochondrial Hsp90 (TRAP1) ATPase activity. *J Biol Chem* **293**, 13717–13724 (2018).

116. Hanahan, D. Hallmarks of Cancer: New Dimensions. *Cancer Discov* **12**, 31–46 (2022).

117. Levin, S. N. *et al.* Disruption of proteome by an oncogenic fusion kinase alters metabolism in fibrolamellar hepatocellular carcinoma. *Sci Adv* **9**, eadg7038 (2023).

CHAPTER 2 | MITOCHONDRIAL CALCIUM SIGNALING REGULATES BRANCHED-CHAIN AMINO ACID CATABOLISM IN FIBROLAMELLAR CARCINOMA

2.1 | Introduction

Efficient utilization of energy sources based on their availability and cellular needs requires metabolic flexibility. Mitochondrial calcium (Ca^{2+}) signaling plays a central role in metabolic adaptation to acute or prolonged changes in energy demands and metabolite levels [1-5]. A principal regulator of this signaling pathway is the mitochondrial Ca^{2+} uniporter (hereon referred to as the uniporter), a Ca^{2+}-selective channel in the inner mitochondrial membrane. The uniporter facilitates bulk entry of Ca^{2+} into the mitochondrial matrix [6, 7]. This Ca^{2+} influx contributes to activation of the tricarboxylic acid (TCA) cycle, buffering of cytosolic Ca^{2+} signaling, or mitochondrial damage and cell death, depending on the amount of Ca^{2+} that enters the mitochondria [8]. Thus, the uniporter regulates metabolism, mitochondrial and cytosolic Ca^{2+} signaling, and cell survival.

Five core proteins constitute the uniporter: three transmembrane proteins (MCU, EMRE and MCUb) and two membrane-associated regulatory subunits (MICU1-2) [6, 7, 9, 10]. MCU and EMRE are necessary and sufficient to form a functional Ca^{2+} channel, and MICU1-2 and MCUb regulate uniporter activity [10-13]. In addition, diverse physiological and pathological stimuli alter uniporter-mediated mitochondrial Ca^{2+} uptake through transcriptional and post-translational mechanisms [1, 8, 14]. Both increased and decreased mitochondrial Ca^{2+} levels are observed in disease-associated states, such as high fat diet-induced obesity[15],neurodegeneration [16, 17], metabolic disorders [18] and cancer [19]. Reduced mitochondrial Ca^{2+} uptake leads to slower cell proliferation rates [20-22], smaller body size [23, 24], exercise intolerance [24], and epigenetic changes [25] in mice. Conversely, increased mitochondrial Ca^{2+} load is most often associated with mitochondrial damage and cell death [26]. Nevertheless, enhanced uniporter activity is thought to be beneficial under energetic stress [1], pointing to a complex regulation of mitochondrial Ca^{2+} signaling to balance cellular metabolic needs.

Despite the importance of the uniporter for metabolic adaptation, a comprehensive analysis of mitochondrial pathways that are regulated by the uniporter is lacking. To better understand the effects of the uniporter on mitochondrial function, we analyzed MCU knockout (KO) mitochondria using proteomics and RNA sequencing. Our results show increased expression of branched-chain amino acid (BCAA) catabolism proteins in HeLa MCU KO cells. Furthermore, a key phosphorylation event that inhibits pathway activity is reduced in these cells, thereby augmenting BCAA catabolism.

To determine if these metabolic changes are reversed under conditions of elevated mitochondrial Ca^{2+}, we turned to fibrolamellar carcinoma (FLC), an oncocytic tumor with indications of increased mitochondrial Ca^{2+} levels in the literature [27-29]. FLC is a rare liver cancer that primarily affects adolescents and young adults. Recent in-depth analysis of the FLC proteome and transcriptome identified significant differences in tumor mitochondria and metabolism compared to adjacent non-tumor liver samples [30], indicating a key role for mitochondria in FLC pathogenesis. Using patient samples and cell models, we show that increased mitochondrial Ca^{2+} levels is a distinguishing feature of FLC. Furthermore, expression of BCAA pathway proteins is significantly decreased in FLC, a phenotype which is reversed by MCU knockdown. This is consistent with the uniporter playing a central regulatory role in BCAA catabolism. We also report that expression of the transcription factor KLF15, a regulator of multiple BCAA catabolism genes, is suppressed in FLC tumors and is regulated by MCU. This pathologic event has important implications for FLC patients due to KLF15's role in promoting expression of the urea cycle enzyme ornithine transcarbamylase (OTC) [31]. Downregulation of OTC is thought to contribute to impaired urea cycle function and subsequently to hyperammonemia and hyperammonemic encephalopathy diagnosed in some late-stage FLC patients [32]. We observe that, similarly to KLF15, OTC expression is suppressed in FLC tumors and is MCU-regulated in cellular models of FLC.

Overall, our results implicate increased uniporter function in FLC and identify BCAA catabolism and the urea cycle as novel uniporter-regulated pathways downstream of KLF15. Based on these findings, we propose that MCU and KLF15 are potential therapeutic targets in the treatment of FLC and its sequelae.

2.2 | Results

2.2.1 | Loss of uniporter slows growth and alters expression of mitochondrial proteins

To better characterize how mitochondria respond to loss of mitochondrial Ca^{2+} uptake, we generated a HeLa MCU KO cell line as well as a rescue cell line by stable expression of FLAG-tagged MCU in the KO cells. As previously reported, loss of MCU significantly slowed growth, which was remedied by MCU re-expression (**Figs. 2.1A, 2.1B)** [20-22,33]. Yet, MCU KO cells did not show a significant decrease in their basal respiration, maximal respiration, ATP production-coupled respiration, respiration due to proton leak, or non-mitochondrial oxygen consumption rates, and they showed only a mild reduction in their spare respiratory capacity (**Figs. S2.1A-G)**, despite having impaired TCA cycle activity.

These mild energetic phenotypes have been attributed to the activation of glycolysis and glutamine utilization in MCU KO cells [20, 33] Whether there are additional metabolic changes that sustain oxidative phosphorylation and energy production in the absence of uniporter is unclear. To better characterize the effects of MCU loss on the mitochondria, we compared WT and MCU KO mitochondria using proteomics **(Fig. 2.1C)** and transcriptomics **(Fig. 2.1D)**. Gene set enrichment analysis [34] of significantly upregulated mitochondria-associated proteins and genes in MCU KO cells showed a strong enrichment of the branched-chain amino acid (BCAA) catabolism pathway and fatty acid oxidation (FAO) in both datasets **(Figs. S2.1H, S2.1I).** A link between FAO pathway and MCU has been reported previously [4]. We confirmed FAO activation in MCU KO cells by lipid analysis. MCU KO cells contained markedly reduced levels of very long-chain fatty acids compared to WT cells **(Fig. S2.1J)**. This was accompanied by increased levels of acylcarnitines, fatty acid metabolites that are transported to the mitochondria for oxidation **(Fig. S2.1K)**. Interestingly, 8 of the 48 proteins in the Kyoto Encyclopedia of Genes and Genomes (KEGG) BCAA catabolism pathway (hsa0028) showed a significant increase in protein levels **(Fig. 2.1E)**. In addition, 20 out of 48 KEGG BCAA catabolism genes showed a significant 1.3-2 fold increase in their mRNA levels in MCU KO cells **(Fig. 2.1F)**. Because of this strong enrichment of BCAA metabolism genes in our dataset and the importance of BCAA metabolism in a diverse set of diseases, we focused on the previously unreported link between mitochondrial calcium signaling and BCAA metabolism.

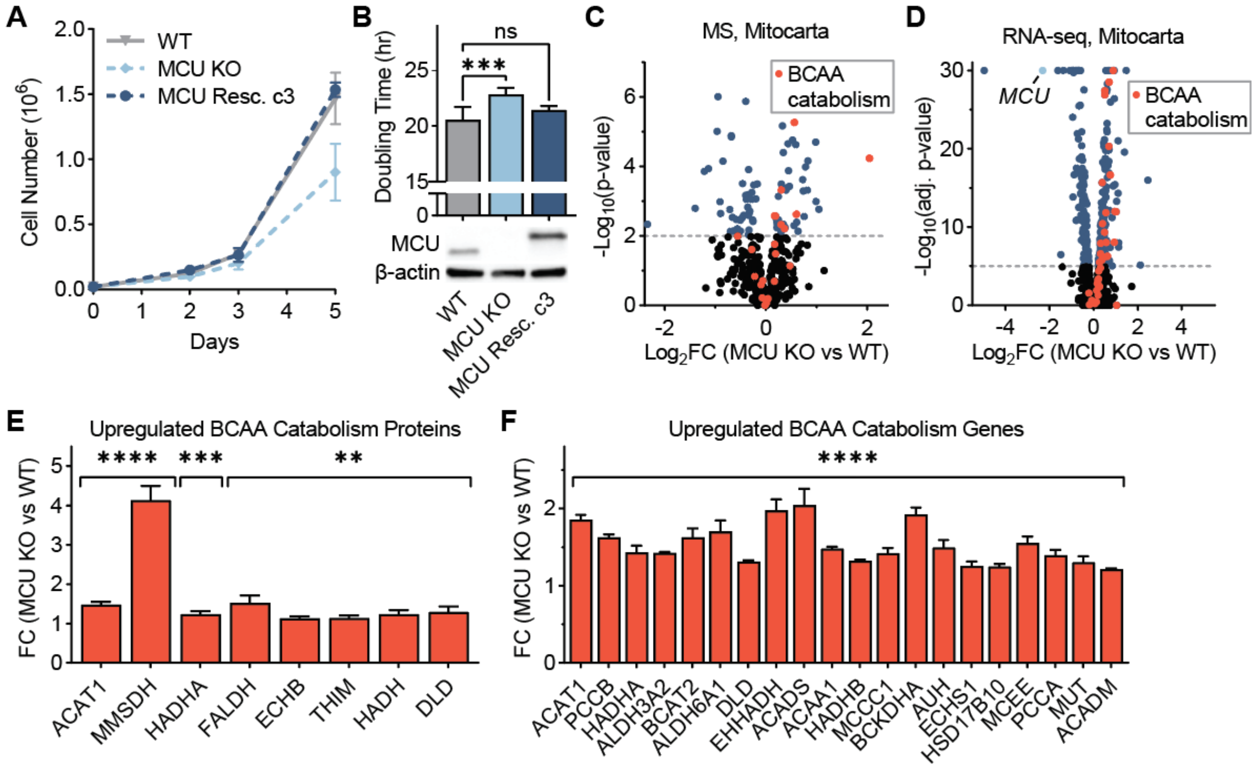

Figure 2.1 MCU KO cells exhibit growth defects and altered mitochondrial proteome

(A) Loss of MCU reduces proliferation of HeLa cells. WT, MCU KO, and MCU rescue cells were counted on days 2, 3, and 5 after plating; n=4-6. **(B)** HeLa cell doubling times were calculated from cell counts on days 2 to 5 in (A); statistical significance was determined by Dunnett's multiple comparisons test following one-way ANOVA; expression of MCU and MCU-FLAG were confirmed by Western blot. **(C)** Volcano plot shows relative abundance of mitochondrial proteins in MCU KO cells compared to WT cells. Red points indicate proteins in the valine, leucine, and isoleucine degradation KEGG pathway; n=5. **(D)** Volcano plot shows relative abundance of mRNAs encoding mitochondrial proteins in MCU KO cells compared to WT cells. Red points indicate genes in the valine, leucine and isoleucine degradation KEGG pathway; MCU is marked in light blue; n=3. **(E, F)** Fold change (FC) of valine, leucine, and isoleucine degradation-associated proteins (E) and genes (F) enriched in MCU KO cells in (C, D); proteins and genes are listed in order of ascending p-value. All error bars represent standard deviation; ns indicates non-significant, * indicates a p-value < 0.05, ** indicates a p-value < 0.01, *** indicates a p-value < 0.001, and **** indicates a p-value < 0.0001.

2.2.2 | BCAA catabolism pathway activity is upregulated by MCU loss

To better understand the relationship between mitochondrial Ca^{2+} signaling and BCAA metabolism, we monitored expression of select pathway proteins after uniporter perturbation. HeLa cells lacking MCU exhibited no mitochondrial calcium uptake, and a small but consistent increase in levels of BCAA catabolism proteins **(Figs. 2.2A, 2.2B, S2.2A)**. We observed similar changes in HeLa cells that lack EMRE, an essential component of the uniporter **(Figs. 2.2C, 2.2D, S2.2B).** To establish whether uniporter-mediated BCAA catabolism regulation extends to other cell types and species, in particular to cells that originate from tissues with high BCAA catabolism rates such as liver, we blotted for pathway proteins in the mouse hepatocyte cell line AML12. RNAi-mediated knockdown of MCU reduced mitochondrial Ca^{2+} uptake rates **(Fig. S2.2C)** and significantly increased the expression of proteins in the BCAA catabolism pathway **(Figs. 2.2E, 2.2F)**.

The committed step in the BCAA catabolism pathway is the oxidative decarboxylation reaction carried out by the branched-chain α-ketoacid dehydrogenase (BCKDH) complex. The activity of this complex is regulated by phosphorylation and dephosphorylation of the E1α subunit by the branched-chain α-ketoacid dehydrogenase kinase (BCKDK) and mitochondrial protein phosphatase 1K (PPM1K), respectively. Phosphorylation by BCKDK is inhibitory, whereas dephosphorylation by PPM1K activates the complex **(Fig. 2.2G)**. We considered the possibility that BCKD-E1α phosphorylation may be uniporter-regulated, similar to pyruvate dehydrogenase (PDH) complex in some tissues[35,36]. Interestingly, in HeLa cells, BCKD-E1α phosphorylation was significantly reduced in MCU or EMRE KO cells and after MCU knockdown **(Figs. 2.2H, 2.2I, 2.2J, S2.2D-S2.2F)**. However, in AML12 cells that originate from liver, where PDH phosphorylation is known to be insensitive to mitochondrial Ca^{2+} levels [35], we did not observe a change in phospho-BCKD-E1α levels **(Fig. S2.2G)**. These data suggest that MCU regulates the activity of the BCAA catabolism pathway both through phosphorylation and transcriptional regulation of pathway enzyme expression in a cell- and tissue-specific manner.

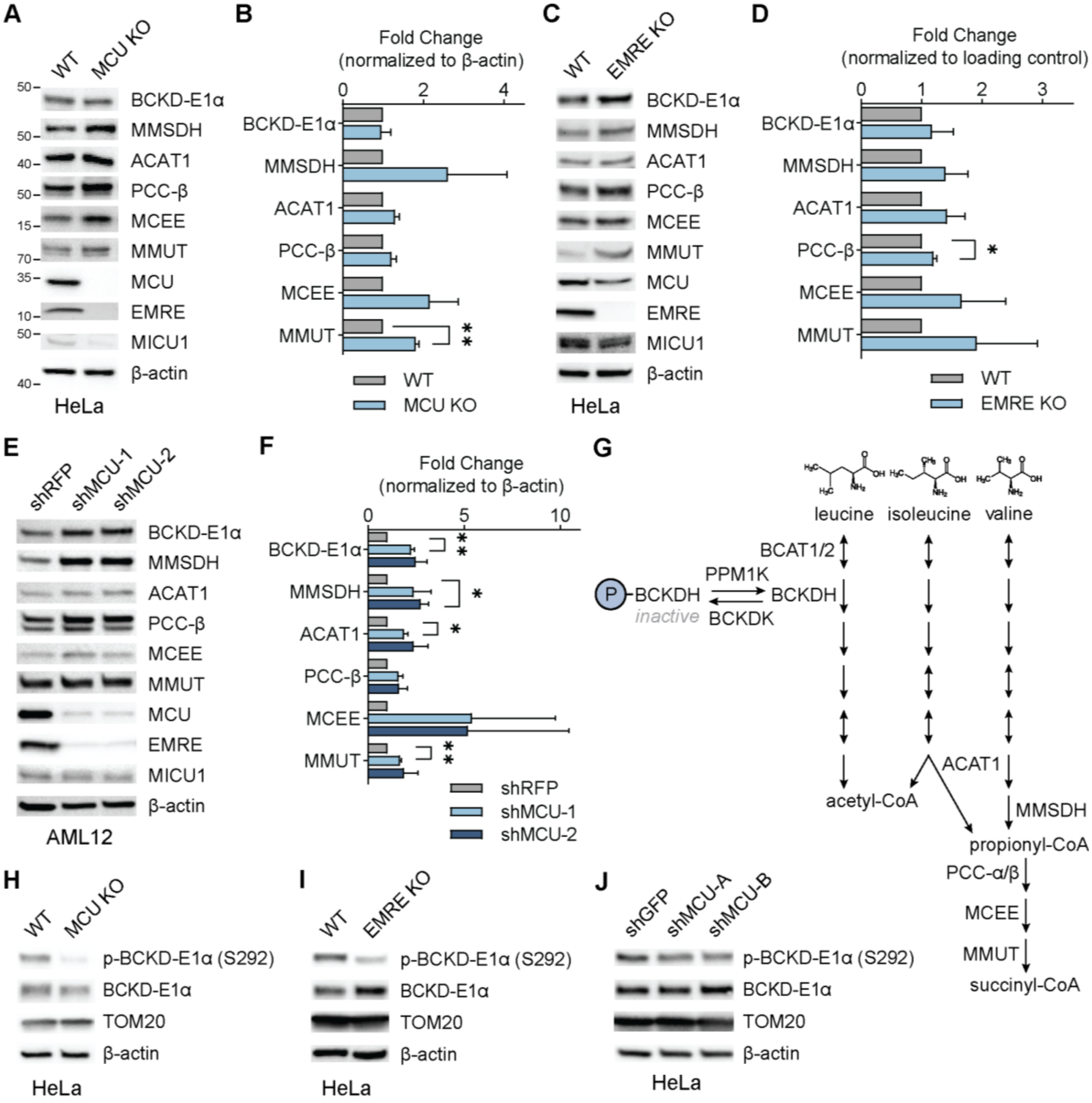

Figure 2.2 Mitochondrial calcium uniporter regulates BCAA catabolism pathway

(A, B) Immunoblots of select BCAA catabolism proteins and uniporter components (A) and their quantification (B) in HeLa WT and MCU KO cells show mild but consistent increase in pathway protein expression; n=3. **(C, D)** Loss of EMRE also causes increased BCAA catabolism protein expression; immunoblots of select BCAA catabolism pathway proteins (C) and their quantification (D) in HeLa WT and EMRE KO cells; n=3. **(E, F)** Immunoblots of select BCAA pathway proteins (E) and their quantification (F) in AML12 cells following shRNA-mediated MCU knockdown; n=3. **(G)** Schematic of BCAA catabolism pathway. The committed step in the pathway is catalyzed by BCKDH complex, which is activated by dephosphorylation. **(H-J)** Immunoblots of phosphorylated and total BCKD-E1α in HeLa WT, MCU KO (H) and EMRE KO cells (I) and WT HeLa cells with MCU knockdown (J); n=3. Statistical significance was determined by one-sample t-test. All error bars represent standard deviation; * indicates a p-value < 0.05 and ** indicates a p-value < 0.01.

2.2.3 | BCAA catabolism helps maintain NADH/NAD$^+$ balance in MCU KO cells

To understand the physiological significance of increased BCAA catabolism in the absence of MCU, we treated cells with the BCKDK inhibitor BT2 and measured cell growth. WT cells were not affected by 10 mM BT2 treatment for 3 days, whereas MCU KO cells showed increased growth with further activation of BCAA catabolism **(Fig. 2.3A)**. To explain the mechanism of this unexpected growth phenotype, we first considered the possibility that BCAA catabolism supports the TCA cycle, whose activation is impaired in MCU KO cells.

Degradation of the three BCAAs – valine, leucine, and isoleucine – generates the TCA cycle metabolites acetyl-CoA and succinyl-CoA **(Fig. 2.3B)**. Because loss of MCU abrogates stimulation of the Ca^{2+}-sensitive TCA cycle enzymes pyruvate dehydrogenase (PDH), isocitrate dehydrogenase (IDH), and oxoglutarate dehydrogenase (OGDH), thereby dampening the production of acetyl-CoA and subsequently succinyl-CoA, we conjectured that increased BCAA catabolism in MCU KO cells supports the TCA cycle. We tested this hypothesis by tracing $^{13}C_6$-labelled leucine carbons after a short labelling period **(Fig. 2.3C)**. Interestingly, despite having equal amounts of labelled leucine, MCU KO cells showed decreased or unchanged incorporation of leucine-derived carbons into TCA cycle intermediates, as well as into glutamate and aspartate, compared to WT cells **(Fig. 2.3B)**. These data suggest that BCAA carbons do not preferentially feed into the TCA cycle in MCU KO cells.

MCU KO cells have reduced $NADH/NAD^+$ levels [24], and we hypothesized that increased BCAA catabolism could provide an alternative source of NADH to compensate for this deficiency. To understand the contribution of the BCAA catabolism pathway to $NADH/NAD^+$ homeostasis in MCU KO cells, we starved WT and MCU KO cells of BCAAs for three hours and measured relative $NADH/NAD^+$ ratios. Consistent with previous reports, MCU KO cells had a lower $NADH/NAD^+$ ratio than WT cells under normal growth conditions. Moreover, while BCAA withdrawal did not affect the $NADH/NAD^+$ ratio in WT cells, MCU KO cells trended toward a reduction in the absence of BCAAs **(Fig 2.3D)**. These findings show an unexpected function of BCAA catabolism in cellular energy homeostasis through NADH production independent of the TCA cycle activity and show an important role for Ca^{2+} signaling in this regulation.

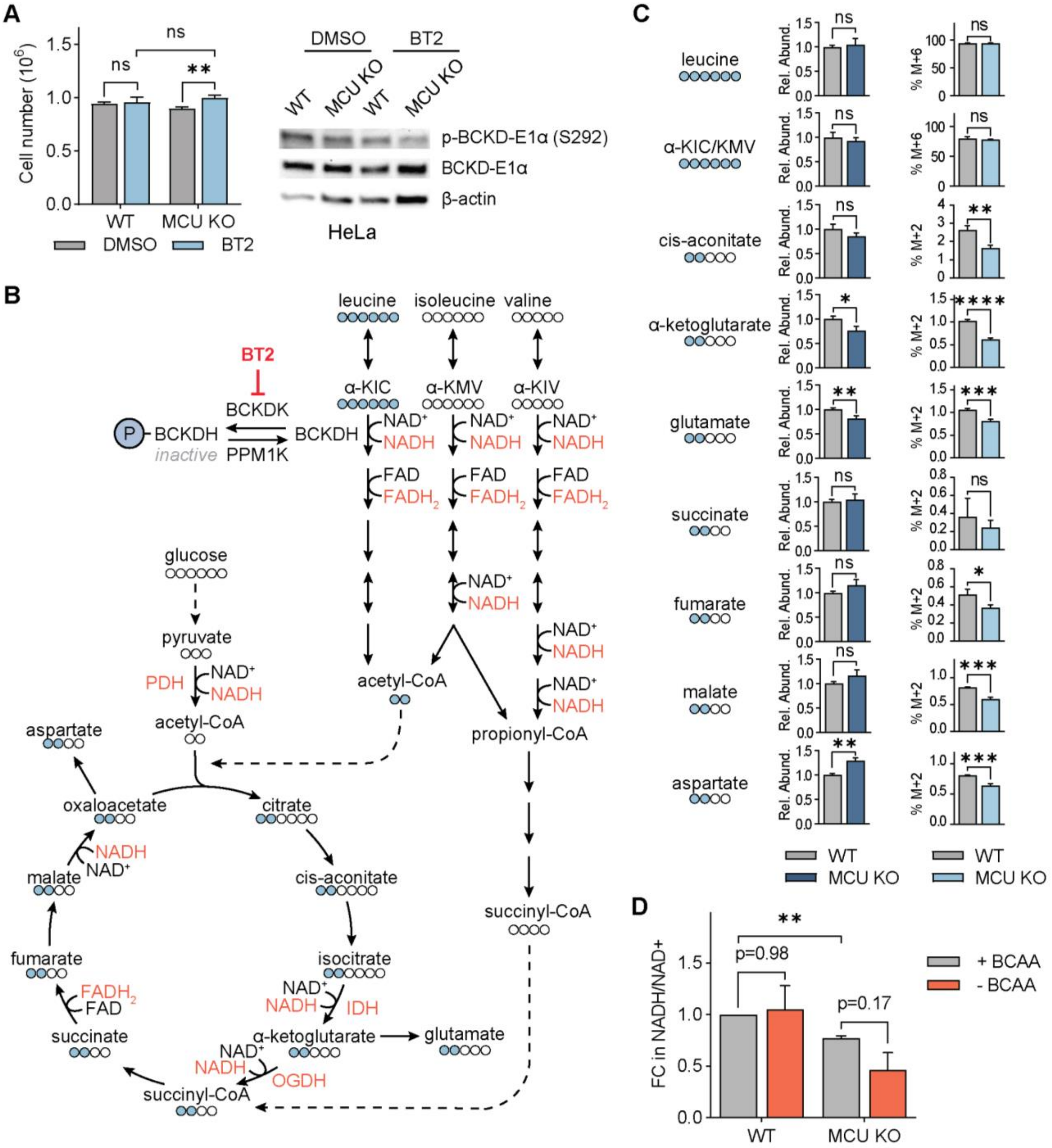

Figure 2.3 BCAA catabolism helps maintain NADH/NAD⁺ balance in MCU KO cells

(A) Cell numbers of WT and MCU KO cells with and without pharmacological activation of BCAA catabolism with BT2. Cells were counted three days after plating and treatment; n=4-5. Statistical significance was determined by Dunnett's multiple comparisons test following one-way ANOVA. **(B)** Schematic of BCAA catabolism and TCA cycle enzymes and metabolites; BCAA catabolism produces acetyl-CoA and succinyl-CoA, which can enter the TCA cycle; Ca^{2+}-regulated enzymes and NAD^+/NADH, FAD/$FADH_2$ coupled reactions are shown in red. Labelled leucine carbons (indicated as blue circles) and their incorporation into the TCA cycle are also shown. **(C)** Relative abundance of indicated metabolites and their fraction generated from labeled leucine in WT and MCU KO HeLa cells are shown. Statistical significance was determined by unpaired t-test; n=3. **(D)** Relative NADH/NAD$^+$ ratios in WT and MCU KO cells with and without BCAA starvation. All error bars indicate standard deviation; ** indicates a p-value < 0.01, *** indicates a p-value < 0.001, **** indicates a p-value < 0.0001.

2.2.4 | Increased mitochondrial Ca^{2+} levels are a hallmark of fibrolamellar carcinoma (FLC)

FLC is a rare liver cancer that affects children and young adults. This cancer is characterized by a somatic ~400 kb genomic deletion that fuses the first exon of the DnaJ homolog subfamily B member 1 gene (*DNAJB1*) to exon 2–10 of the cAMP-dependent protein kinase catalytic subunit alpha gene (*PRKACA*) [37] **(Fig. 2.4A)**. This deletion event generates a fusion kinase, DNAJ-PKAc, which we refer to as DP from hereon. FLC tumors are oncocytic neoplasms that are characterized by an aberrant number of mitochondria [27, 28, 38]. In addition, earlier reports noted the presence of electron dense particles in electron microscopy (EM) images of FLC tumors [28]. These electron dense particles are Ca^{2+} phosphate precipitates that form in the mitochondrial matrix [39, 40] as a result of high matrix Ca^{2+} levels. We sought to further characterize mitochondrial Ca^{2+} changes and investigate uniporter function and BCAA metabolism in FLC.

We obtained paired FLC and non-tumor liver (NTL) tissue samples from five patients and confirmed DP expression in the tumors using western blotting with an antibody that detects PKAc **(Fig. 2.4B, Supp Table 2.1)**. To investigate mitochondrial Ca^{2+} levels in FLC, we performed EM analysis on tumor and non-tumor liver from one patient **(Figs. 2.4C, 2.4D)**. 39% of FLC mitochondria contained one or more electron dense Ca^{2+} deposits compared to 4% of mitochondria from non-tumor liver **(Fig. 2.4E)**. We also analyzed mitochondria from a second patient, for which a control liver sample did not exist, by comparing mitochondria in oncocytic and peri-oncocytic cells from the tumor periphery **(Figs. S2.4A-S2.4C)**. This analysis also showed an increased percentage of mitochondria with electron dense particles in oncocytic cells (24%) compared to non-oncocytic cells (10%) **(Fig. S2.4D)**. EM analysis of tumor and control liver from a hepatocellular carcinoma (HCC) patient did not show more abundant Ca^{2+} deposits in HCC mitochondria **(Figs. S2.4E-S2.4G)**. This suggests that high levels of mitochondrial Ca^{2+} deposits may be an FLC-specific phenotype.

We next quantified levels of the uniporter proteins MCU, EMRE and MICU1 in FLC and paired NTL control lysates. MCU and EMRE levels were significantly increased relative to TOM20, and MICU1 trended towards higher expression in tumors **(Figs. 2.4F, 2.4G)**. The control mitochondrial protein HSP60 did not show a significant difference between tumors and control lysates, suggesting that the increase in uniporter protein expression is specific and is not simply a result of increased mitochondrial proteome abundance in FLC. Immunohistochemistry (IHC) analysis of tumor and normal liver sections also showed stronger MCU staining in the tumor **(Fig. 2.4H)**. Quantitative PCR (qPCR) analysis showed that FLC tumors had elevated MCU mRNA levels **(Fig. 2.4I)**. Analysis of MCU transcript levels from 8 matching normal and FLC tumors also showed increased MCU transcript levels in FLC **(Fig. 2.4J)**. Together, these data are consistent with higher uniporter expression driving increased mitochondrial Ca^{2+} levels in FLC.

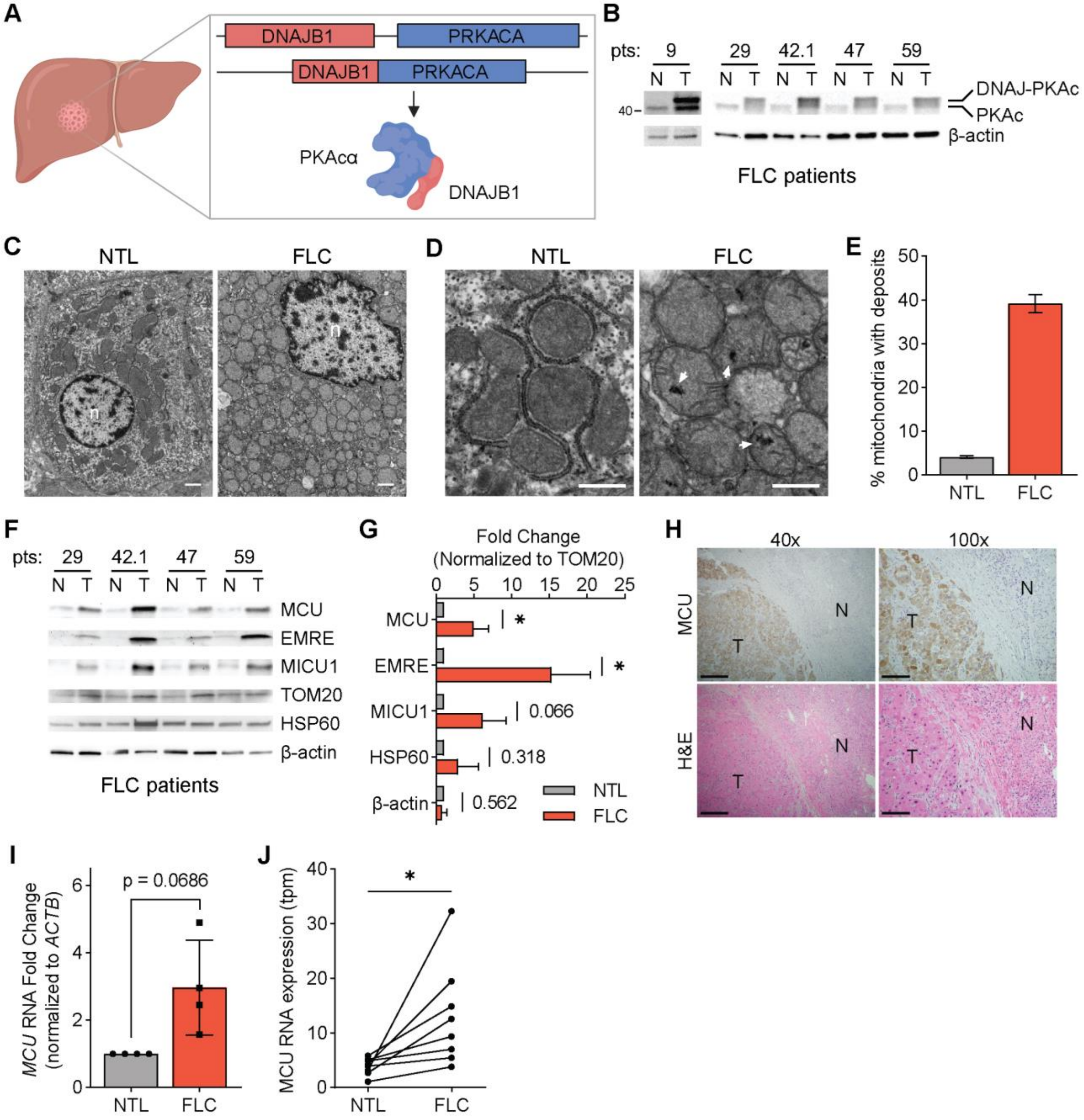

Figure 2.4 FLC is characterized by increased mitochondrial Ca^{2+} levels and uniporter expression

(A) Schematic of FLC liver tumor with heterozygous deletion in chromosome 19 producing the DNAJ-PKAc (DP) fusion protein. **(B)** Immunoblot of lysates from non-tumor (N) and tumor (T) liver from FLC patients shows DP fusion protein expression in the tumor. **(C)** Electron micrographs at 10,000x magnification of non-tumor (NTL) and tumor (FLC) sections from patient 9; nuclei are labeled n; scale bars = 1 µm. **(D)** Micrographs of samples shown in (C) at 25,000x magnification; white arrowheads mark representative Ca^{2+} deposits in the tumor; scale bars = 600 nm. **(E)** Percentage of mitochondria from FLC patient 9 with Ca^{2+} deposits; the mean is reported from manual counting of >500 mitochondria per sample by two independent, blinded analysts. **(F)** Immunoblots of uniporter components and control mitochondrial proteins from paired non-tumor (N) and FLC tumor (T) samples. **(G)** Pooled quantification of immunoblots in (F) normalized to TOM20 levels; statistical significance was determined by one-sample t-test. **(H)** H&E and MCU IHC staining of non-tumor (N) and tumor (T) regions of liver from FLC patient 9; 40x and 100x image scale bars are 500 µm and 200 µm, respectively. **(I)** qPCR analysis of MCU RNA expression in paired non-tumor liver and tumors from FLC patients 29, 42.1, 47, and 59. **(J)** MCU mRNA expression in 8 paired normal liver and FLC tumors. All error bars indicate standard deviation; numbers above error bars indicate p-values; * indicates a p-value < 0.05.

2.2.5 | Cellular FLC models show increased mitochondrial Ca^{2+} levels

To better understand the role of mitochondrial Ca^{2+} signaling in FLC metabolism, we turned to two clonal AML12 cell lines, c14 and c4, which were generated using genome editing [41] and used as cellular models of FLC. These clones carry the heterozygous FLC deletion, express a single allele of the fusion kinase DP, and grow faster than WT AML12 cells **(Figs. 2.5A, 2.5B)**. The clonal cells also recapitulate FLC-associated signaling events and have been successfully used to investigate FLC biology and therapeutics [41, 42].

To determine if c14 and c4 clones have increased mitochondrial Ca^{2+} levels, we treated digitonin-permeabilized cells with the mitochondrial uncoupler CCCP, which results in release of Ca^{2+} ions from the mitochondria. Both clones showed increased mitochondrial Ca^{2+} release compared to WT **(Figs. 2.5C, 2.5D)**. Measurement of free matrix Ca^{2+} levels using the mitochondria-targeted G-GECO Ca^{2+} reporter[43] indicated higher resting Ca^{2+} levels in the FLC clones **(Figs. 2.5E-2.5G)**. Resting cytosolic Ca^{2+} levels were similar in the clones and WT cells **(Fig S2.5A)**. We also measured mitochondrial Ca^{2+} uptake rates in digitonin-permeabilized cells. C14 and c4 mitochondria showed decreased Ca^{2+} uptake rates **(Figs. 2.5H, 2.5I),** despite expressing MCU at comparable levels to WT cells **(Fig. 2.5J)**. This decrease in Ca^{2+} uptake rate was not due to reduced mitochondrial membrane potential in FLC clones **(Fig. S2.5B)**, but is likely due to higher concentrations of Ca^{2+} in the matrix negatively affecting mitochondrial Ca^{2+} uptake rates. Next, we tested whether elevated Ca^{2+} levels in c14 and c4 mitochondria are dependent on the kinase activity of DP, which sustains FLC tumor growth [44, 45]. Interestingly, the PKA inhibitor BLU2864 [46] did not affect the amount of Ca^{2+} released from WT mitochondria, but caused a significant reduction in the FLC clones **(Fig. 2.5K)**, with concomitant decreases in PKA substrate phosphorylation in all cell lines **(Fig. S2.5C)**. These data indicate that the kinase activity of DP contributes to the dysregulation of mitochondrial Ca^{2+} homeostasis in the FLC clones.

To investigate the consequences of increased mitochondrial Ca^{2+} levels for oxidative phosphorylation and energy production in FLC, we measured the oxygen consumption rate (OCR) of AML12 cells with the Seahorse extracellular flux analyzer. FLC clones showed increased basal, maximal and non-mitochondrial OCR, as well as increased spare respiratory capacity, proton leak, and ATP production-coupled respiration **(Figs. 2.5K, S2.5D-S2.5I)**, as would be expected with increased uniporter function [20, 47]. Based on our data, we conclude that high mitochondrial Ca^{2+} is a previously underappreciated feature of FLC that is coupled to DP activity and alters FLC metabolism.

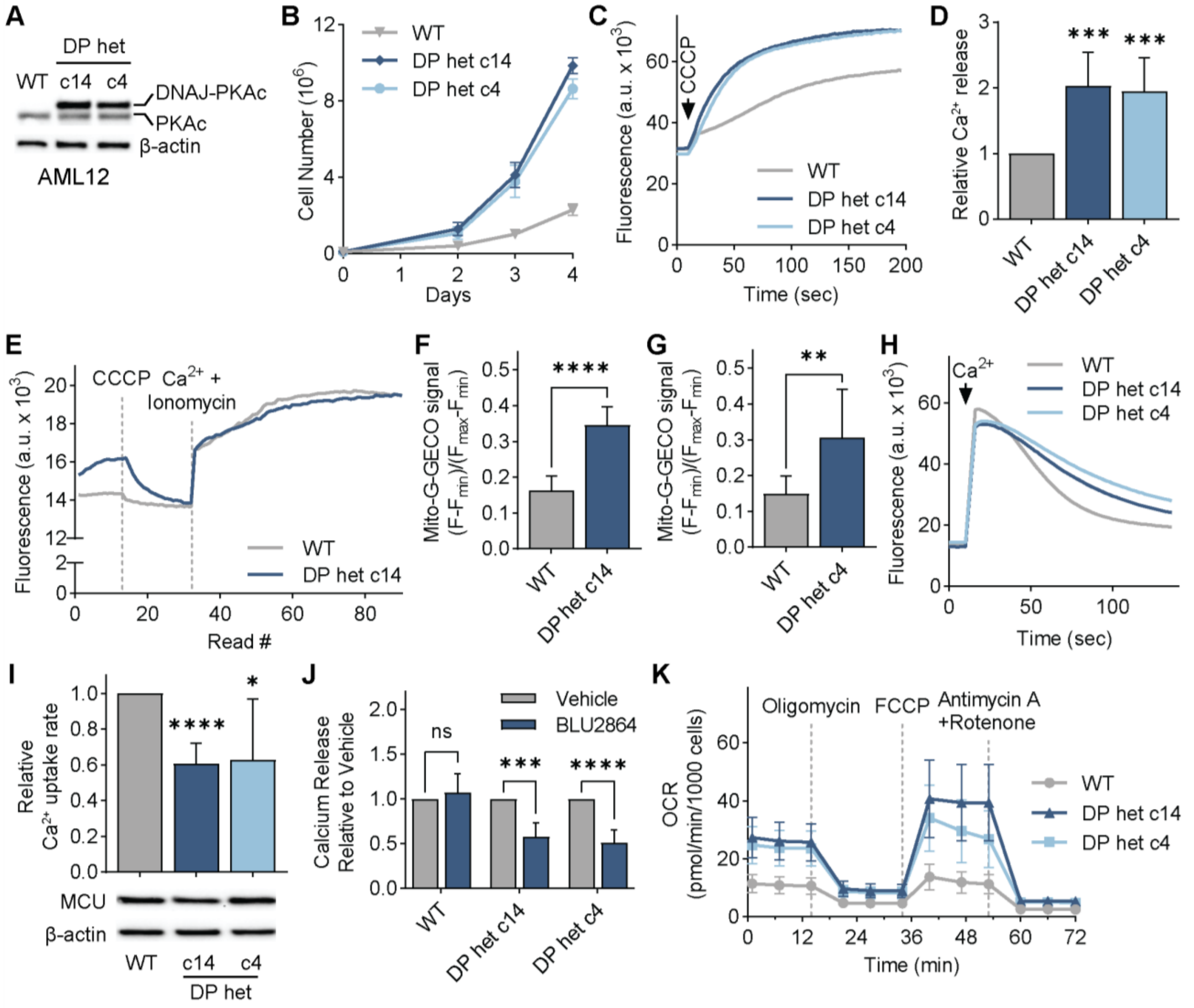

Figure 2.5 Cellular models of FLC show DP-dependent increase in mitochondrial Ca^{2+} levels

(A) Immunoblot of lysates from AML12 WT and clones c14 and c4 using an antibody against PKAc confirm heterozygous DP expression in the clones. **(B)** Proliferation of cellular models of FLC compared to WT AML12 cells; cells were counted on days 2, 3, and 4 after plating; n=3. **(C, D)** Representative traces (C) and quantification (D) of mitochondrial Ca^{2+} release assays in AML12 cells; cells were treated with uncoupler CCCP, and the relative amount of Ca^{2+} released was quantified using a Ca^{2+} indicator dye; statistical significance was determined by one-sample t-test; n=10. **(E)** Representative trace of mitochondrial free Ca^{2+} levels of AML12 WT and c14 cells quantified using matrix-targeted Ca^{2+} reporter G-GECO (mito-G-GECO). **(F, G)** Baseline mito-G-GECO fluorescence normalized to minimum and maximum signals in AML12 WT and c14 (F) or c4 (G) cells; statistical significance was determined by Mann Whitney test; n=20-23 (F) and n=12 (G). **(H, I)** Representative traces (H) and mitochondrial Ca^{2+} uptake rates in

AML12 cells (I); mitochondrial Ca^{2+} uptake rates were calculated by monitoring Ca^{2+} clearance in the presence of a Ca^{2+} indicator dye; statistical significance was determined by one-sample t-test; n=9. Immunoblot of MCU shows comparable MCU expression in DP clones compared to WT controls. **(J)** Mitochondrial Ca2+ release was measured as in (C) after cells were treated with 5 μM PKA inhibitor BLU2864 or DMSO for 4 days and normalized to total protein levels; fold change in released Ca^{2+} is shown relative to DMSO control for each cell line; statistical significance was determined by paired t-test, n=7-9. **(K)** Seahorse extracellular flux analysis of oxygen consumption rates (OCR) in FLC clones compared to WT AML12 cells at baseline and after indicated treatments; n=10-16. All error bars indicate standard deviation; * indicates a p-value < 0.05, ** indicates a p-value < 0.01, *** indicates a p-value < 0.001, and **** indicates a p-value < 0.0001.

2.2.6 | Uniporter regulates expression of proteins involved in BCAA catabolism in FLC

Decreased BCAA catabolism is associated with poor patient outcomes in hepatocellular carcinoma [48], however the mechanisms by which cancer cells downregulate this pathway are not known. We asked whether increased uniporter activity in FLC suppresses expression of BCAA catabolism genes, converse to the increase we observed in MCU KO cells. Analysis of tumors from FLC patients showed significantly reduced levels of BCAA catabolism pathway enzymes compared to matching non-tumor liver samples **(Fig. 2.6A)**, with less than 50% expression in the tumors compared to normal liver when protein levels were normalized to the outer mitochondrial membrane protein TOM20 (**Fig. 2.6B)**. These trends were also evident in FLC clones c14 and c4 **(Figs. 2.6C, 2.6D).** Knockdown of MCU using two hairpin RNAs in FLC cellular models increased expression of BCAA catabolism pathway enzymes **(Figs. 2.6E, 2.6F)**. Interestingly, we did not observe an MCU-dependent change in phosphorylation of BCKD-E1α in patient lysates or AML12 c14 and c4 cells **(Figs. S2.6A-S2.6C)**, in contrast with our observations in MCU KO HeLa cells **(Fig. 2.2H)**, suggesting that mitochondrial Ca^{2+} signaling regulates the pathway's activity through its effects on gene expression or protein stability in the liver. These results are similar to previous reports for PDH phosphorylation [49], and they reflect tissue-specific differences in regulation of mitochondrial metabolism by Ca^{2+} signaling. We also analyzed pathway expression at the RNA level in transcriptomics data from 8 FLC patients. Most pathway genes showed significant reduction in their RNA levels in the tumors compared to matching control liver **(Fig. 2.6G)**. BCAT1, BCAT2, OXCT1 and OXCT2, genes that are not expressed in the healthy liver, were upregulated in the tumors, likely as adaptations to regenerate BCAAs from ketoacids (BCAT1 and 2) and to enable utilization of ketone bodies as an energy source (OXCT1 and 2), which may be beneficial for tumor growth.

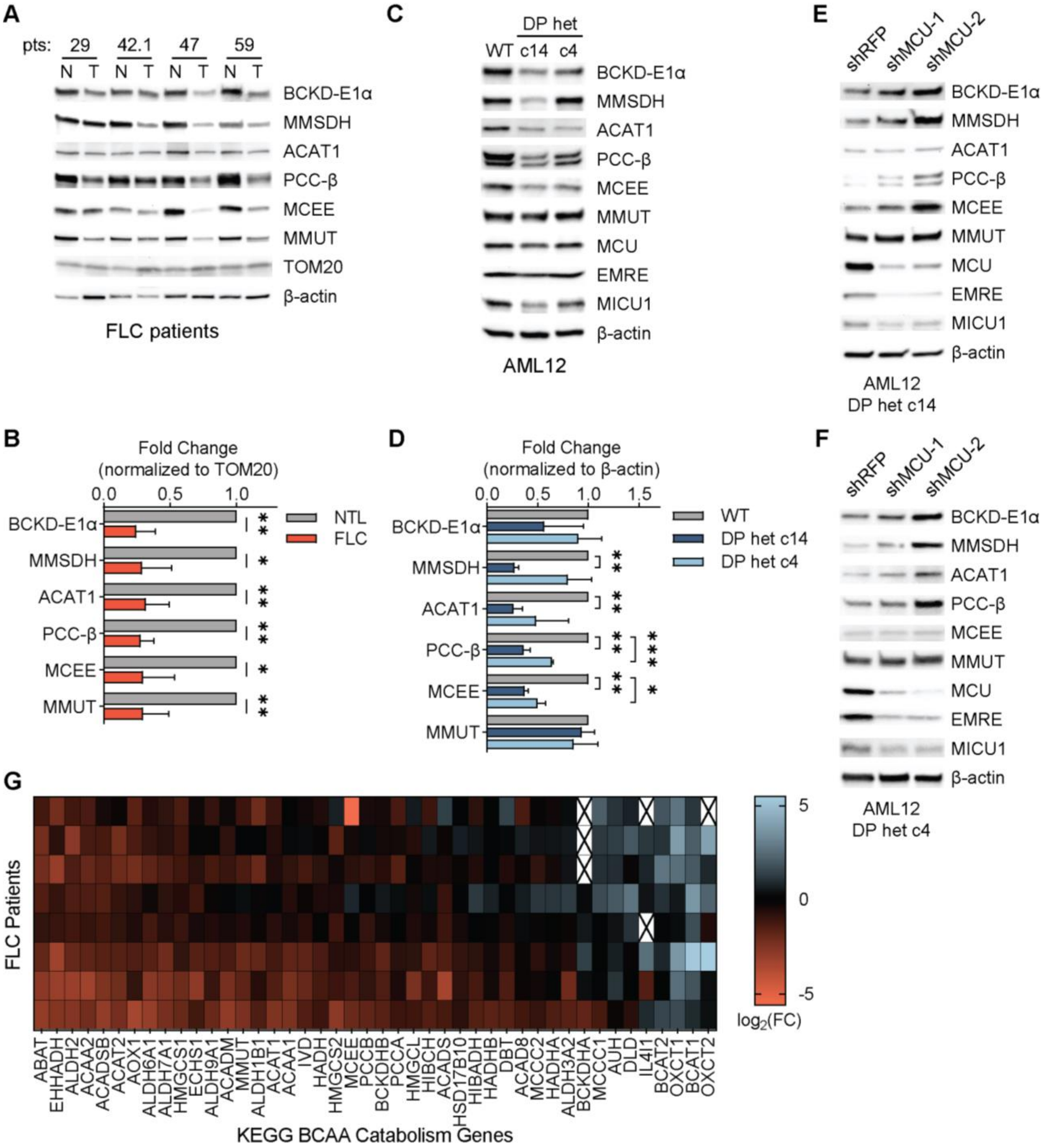

Figure 2.6 Uniporter inhibition alleviates suppressed BCAA catabolism in FLC

(A) Immunoblots of select BCAA catabolism enzymes from paired non-tumor (N) and FLC tumor (T) lysates. **(B)** Pooled quantification of protein levels in (A) normalized to TOM20 levels; statistical significance was determined by one-sample t-test. **(C, D)** Immunoblots (C) and quantification (D) of select BCAA catabolism proteins and MCU complex components in AML12 cells. FLC models show decreased expression of BCAA catabolism pathway enzymes; statistical significance was determined by one-sample t-test; n=4. **(E, F)** MCU knockdown increases expression of BCAA catabolism pathway proteins in FLC clones c14 (E) and c4 (F); immunoblots of select pathway proteins and uniporter components are shown. **(G)** Heatmap shows abundance of BCAA catabolism pathway gene mRNA levels in FLC relative to matched non-tumor liver. n=8 paired NTL and FLC, data was omitted (denoted with an X) when RNA was not detected in NTL and/or FLC sample. All error bars indicate standard deviation; * indicates a p-value < 0.05, ** indicates a p-value < 0.01, and *** indicates a p-value < 0.001.

2.2.7 | Mitochondrial Ca^{2+} signaling regulates expression of KLF15 and its targets in FLC

Reduced mRNA expression of BCAA pathway enzymes in FLC suggested the presence of a transcriptional regulatory mechanism. Krüppel-like factor 15 (KLF15) is an important transcriptional regulator of metabolic gene expression in the liver, including BCAA catabolism and urea cycle genes [31, 50, 51]. To investigate whether KLF15 plays a role in FLC metabolism, we first probed for KLF15 in lysates from FLC patients by Western blot. FLC tumors exhibited markedly reduced levels of KLF15 **(Fig. 2.7A)**. IHC of tissue sections from FLC patients confirmed low KLF15 and high MCU expression in the tumors, with the opposite trend evident in normal liver **(Fig. 2.7B)**. Likewise, AML12 clones c14 and c4 showed reduced KLF15 expression compared to WT cells **(Fig. 2.7C)**.

To investigate the role of uniporter function in KLF15 regulation, we knocked down MCU in AML12 WT and c14 cells. This caused a substantial increase in KLF15 levels **(Figs. 2.7D, 2.7E)**, suggesting that mitochondrial Ca^{2+} signaling negatively regulates KLF15 expression. We reasoned that reduced KLF15 expression may have important metabolic consequences beyond inhibition of BCAA catabolism in FLC, including regulation of the urea cycle by KLF15. Defects in the urea cycle can lead to accumulation of ammonia and cause hyperammonemia **(Fig. 2.7F)**, which can cause neurological damage and death [52]. Interestingly, KLF15 KO mice suffer from increased blood ammonia levels due to significantly reduced OTC expression and activity in the liver [31]. Decreased OTC expression has also been identified as a potential cause of hyperammonemia in some FLC patients [30]. Protein and RNA levels of OTC also showed a significant reduction in tumor samples compared to normal liver in our patient cohort **(Figs. 2.7G-2.7I)**. Analysis of OTC mRNA in 8 matching normal and FLC liver samples showed a decrease in OTC expression, consistent with transcriptional regulation of OTC in FLC **(Fig. 2.7J)**. Moreover, knockdown of MCU in WT AML12 and c14 cells increased OTC expression **(Figs. 2.7K, 2.7L)**, suggesting a previously unknown link between mitochondrial Ca^{2+} signaling and urea cycle regulation.

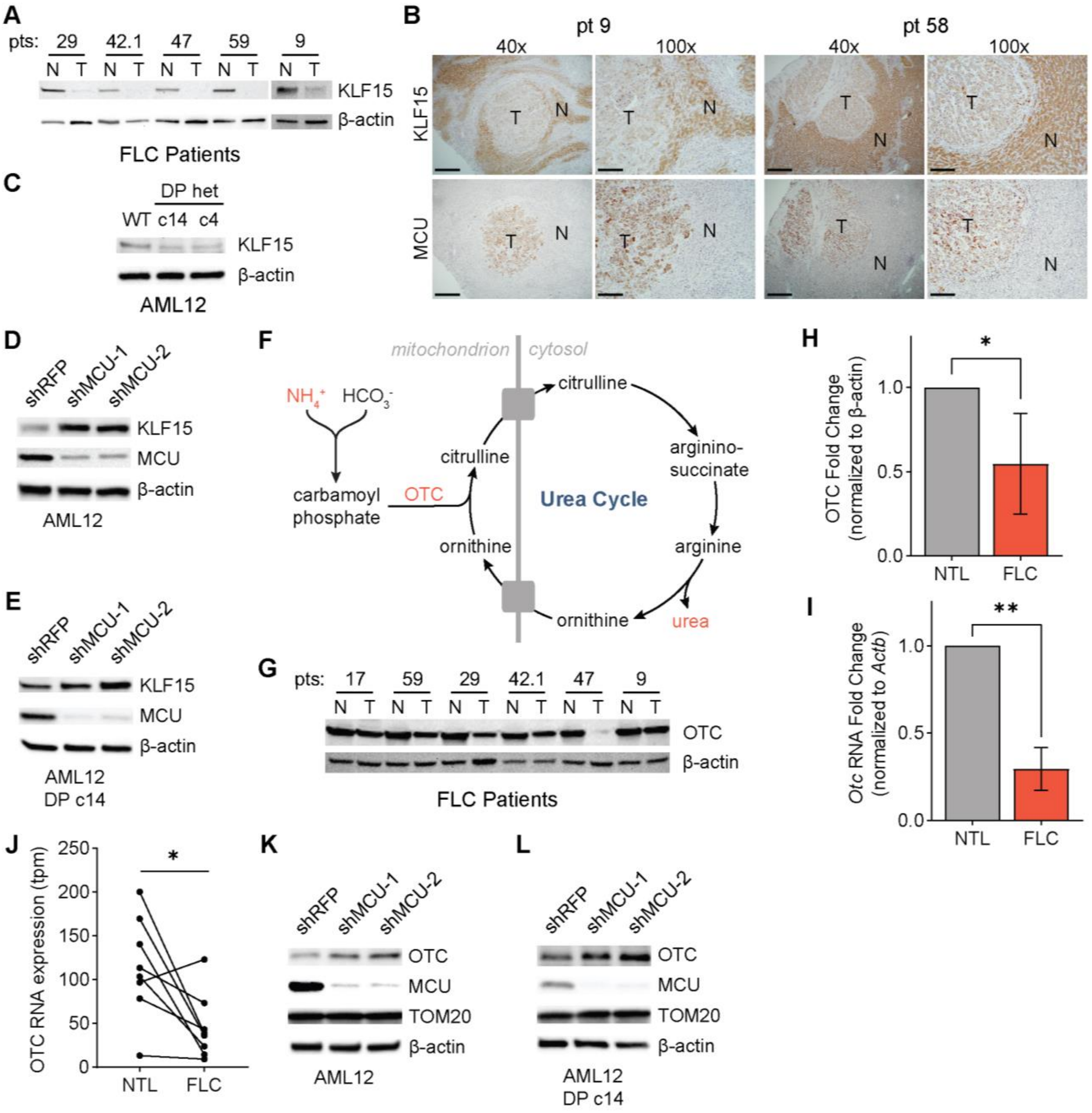

Figure 2.7 Reduced KLF15 and OTC expression in FLC is regulated by the uniporter

(A) Immunoblots of KLF15 in paired non-tumor (N) and FLC tumor (T) lysates. **(B)** IHC of MCU or KLF15 on non-tumor (N) and tumor (T) regions from FLC patients 9 and 58 show high MCU and low KLF15 expression in the tumors; 40x and 100x image scale bars are 500 µm and 200 µm, respectively. **(C)** Immunoblot of KLF15 from WT AML12, c14 and c4 lysates. **(D, E)** Immunoblots of KLF15 from WT AML12 (C) and c14 (D) lysates following MCU knockdown. **(F)** Schematic of the urea cycle; metabolites and OTC, a mitochondrial protein with reduced levels in FLC, are shown. **(G)** Immunoblot of OTC from paired non-tumor (N) and FLC tumor (T) lysates. **(H)** Quantification of OTC protein levels in (G) relative to β-actin. **(I)** qPCR analysis of OTC mRNA expression in paired non-tumor liver and tumors from FLC patients 29, 42.1, 47, and 59. **(J)** OTC mRNA expression in 8 paired normal liver and FLC tumors. **(K, L)** Immunoblots of OTC from WT AML12 (J) and c14 (K) lysates following MCU knockdown. All error bars indicate standard deviation; * indicates a p-value < 0.05 and ** indicates a p-value < 0.01.

2.2.8 | Model

Based on our data, we propose a model in which mitochondrial Ca^{2+} signaling regulates the BCAA catabolism pathway and the urea cycle through the transcription factor KLF15 **(Fig. 2.8)**. In cells with increased mitochondrial Ca^{2+} levels, such as FLC cells, reduced KLF15 expression leads to reduced expression of BCAA catabolism pathway genes, which conserves essential BCAAs for protein synthesis and promotes cell growth. In cells that do not have bulk mitochondrial Ca^{2+} uptake (MCU-deficient cells), increased KLF15 and activated BCAA catabolism supplies the cells with NADH as a compensatory mechanism in the absence of Ca^{2+} stimulation of TCA enzymes.

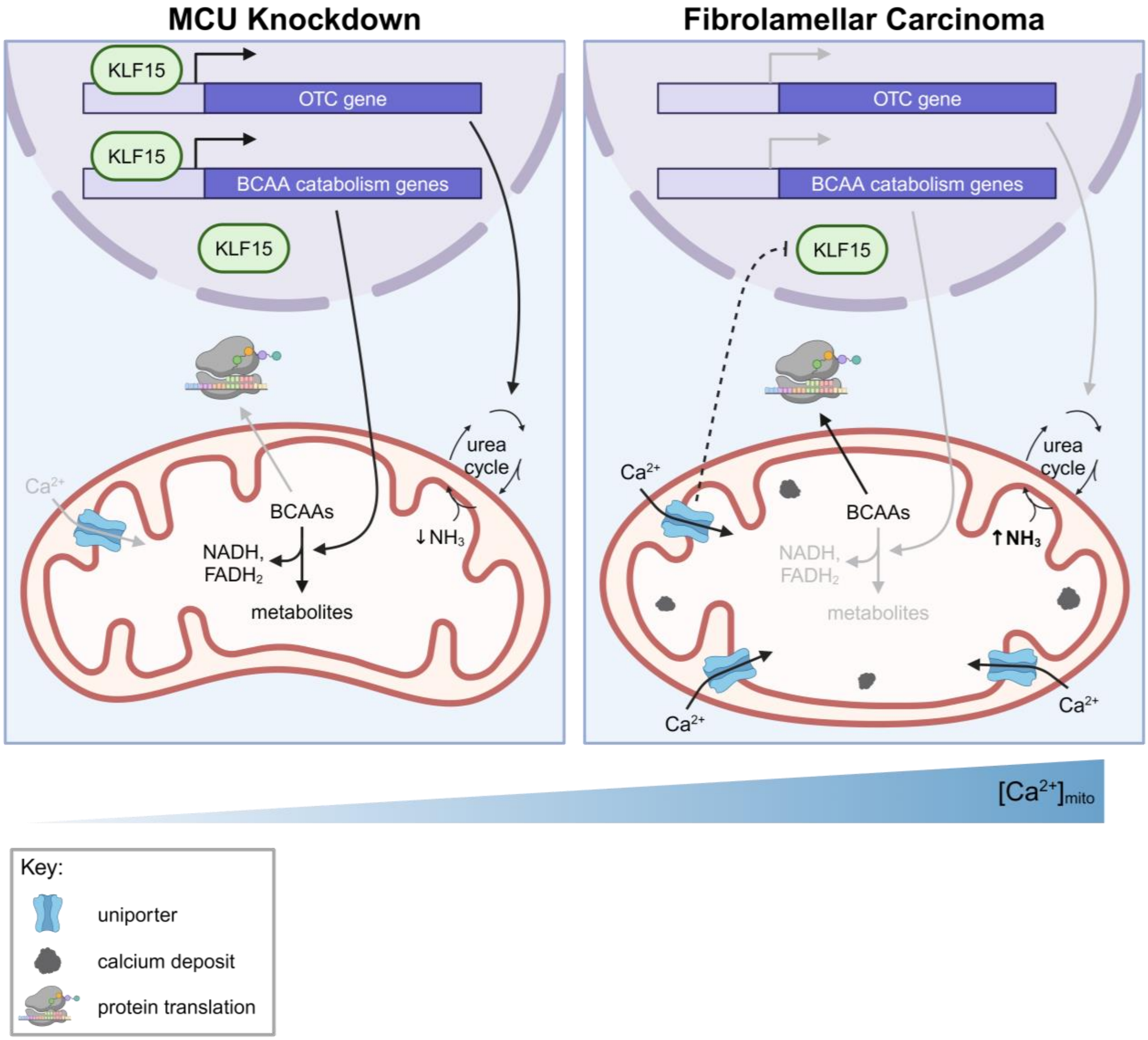

Figure 2.8 Model for regulation of KLF15, BCAAs, and the urea cycle by mitochondrial Ca^{2+} signaling

Our data suggest that, under conditions of low uniporter function, high KLF15 levels stimulate expression of BCAA catabolism pathway genes and OTC. Activation of this pathway helps maintain NADH/NAD^{+} balance. Increased uniporter activity, as observed in FLC, inhibits KLF15 and leads to decreased BCAA pathway and OTC expression. This inhibition conserves BCAAs for use in translation and cell growth. MCU inhibition also causes urea cycle impairment, which can cause hyperammonemia. How the uniporter regulates KLF15 expression is not known.

2.3 | Discussion

We have uncovered a novel role for the mitochondrial Ca^{2+} uniporter in maintenance of cellular metabolism through regulation of BCAA catabolism. More specifically, we demonstrate that loss of uniporter function results in increased expression of BCAA catabolism enzymes and activation of the pathway's committed step through dephosphorylation. Conversely, in models of high mitochondrial Ca^{2+}, BCAA catabolism is transcriptionally suppressed. Based on our findings, we propose that mitochondrial Ca^{2+} signaling acts as a regulatory switch through which BCAAs are either broken down to support oxidative phosphorylation or conserved for translation in accordance with the cell's needs.

The BCAA catabolism pathway is responsive to nutrients, hormones, and circadian rhythm, and its activity is altered in disease states including type II diabetes, cardiovascular disease, liver disease, and cancer[53-55]. Here, we identify mitochondrial Ca^{2+} signaling as a previously unrecognized mechanism by which the catabolism pathway is regulated. Our data also point to tissue-specific differences in Ca^{2+} regulation of this pathway that are akin to the tissue-specific differences in Ca^{2+}-dependent PDH phosphorylation and TCA cycle regulation[56]. These variances highlight the importance of studying BCAA catabolism regulation in multiple biological contexts. Further work will be necessary to delineate the contribution of Ca^{2+} signaling in transcriptional and post-translational regulation of BCAA catabolism across a broader range of cell types and tissues.

The majority of BCAA catabolism occurs in skeletal muscle, adipose tissue, and the liver[57]. However, the initial conversion of BCAAs to α-ketoacids is not performed in the liver, due to the lack of BCAT1 and BCAT2 expression. Instead, skeletal muscle processes

BCAAs from the diet and supplies the liver with α-ketoacids through the bloodstream[53]. In the current study, most experiments were performed in hepatocyte-derived cell lines without BCAT expression or in frozen liver tissue. As such, we were unable to measure changes in BCAA consumption in these samples. This limited our ability to assess rates of BCAA catabolism directly. Nonetheless, regulation of the pathway components remains sensitive to alterations in cell lines, enabling us to characterize upstream effectors regardless of pathway activity *in vitro*.

We further demonstrated that the relationship between mitochondrial Ca^{2+} signaling and BCAA catabolism is conserved in FLC. To date, there are no effective treatments for FLC other than surgical resection, indicating a need to elucidate the underlying mechanisms driving this cancer and identify potential drug targets. The genetic driver of fibrolamellar oncogenesis was identified by Honeyman *et al.* in 2014 with the discovery of the DNAJ-PKAc fusion kinase[37]. In the subsequent decade, progress has been made in characterizing downstream signaling changes, however, it remained unclear how DP gives rise to the mitochondrial and metabolic alterations observed in FLC tumors[30,41,58]. Our results confirm previous reports that FLC mitochondria contain an increased number of Ca^{2+} deposits[28] and demonstrate for the first time that DP-expressing cells have elevated levels of free Ca^{2+} in their mitochondria. We show that FLC tumors have suppressed expression of many of the proteins responsible for BCAA catabolism and that this phenotype is reversible by inhibiting mitochondrial Ca^{2+} influx.

By reducing BCAA catabolism, FLC tumors conserve their supply of leucine, valine, and isoleucine. We postulate that these essential amino acids are used to sustain increased rates of protein synthesis, supported by a previous study showing a nearly 2-

fold increase in protein translation in DP-expressing cells[58]. Additionally, elevated levels of free BCAAs may have important signaling functions. For example, reduced catabolism of BCAAs in the liver can stimulate mTORC1[48], and accumulation of α-ketoacids inhibits gluconeogenesis in hepatocytes[59]. Whether reduced BCAA catabolism alters signaling and directly contributes to metabolic changes in FLC remains to be seen.

BCAA catabolism enzymes are known to be regulated by the transcription factor KLF15[51,60]. We observe a significant, uniporter-dependent reduction in KLF15 protein levels in DP-expressing cells. Reduction in KLF15 levels has been correlated with tumor growth and poor prognosis in several types of cancer[61-66], but to our knowledge, this is the first time KLF15 expression changes have been implicated in liver cancer. KLF15 also regulates genes associated with gluconeogenesis, lipogenesis, metabolism of non-BCAA amino acids, and the urea cycle[31,67,68]. In line with this, FLC patients can develop an impairment in the urea cycle, resulting in hyperammonemia and, in some cases, hyperammonemic encephalopathy[30,69-71]. This phenotype has been attributed to reduced expression of the KLF15 target OTC[30], which we show can be reversed through knockdown of MCU. Downregulation of OTC may favor tumor growth and survival, as build-up of ammonia in the tumor microenvironment has been shown to inhibit immunosurveillance[72-76]. Additionally, accumulation of the OTC substrates ammonia and ornithine can support the production of collagen[75,77,78]. Collagen is a large component of the fibrous bands which are a hallmark of FLC tumors. Fibrosis has also been attributed to downregulation of KLF15 in heart and kidney disease[79-81]. Furthermore, elevated levels of MCU are associated with increased collagen production and liver fibrosis[82]. Future investigations should consider a potential link between the uniporter, KLF15 and these pathologic features of FLC.

Our model of FLC signaling asserts that mitochondrial Ca^{2+} concentrations are increased due to aberrant DP activity and that mitochondrial Ca^{2+} then suppresses KLF15, thereby regulating expression of BCAA catabolism and urea cycle enzymes. Additional studies are warranted to determine the mechanistic link between DP and accumulation of mitochondrial Ca^{2+}, in particular the upregulation of uniporter proteins. PKA is a multifunctional kinase whose activity and subcellular localization are tightly regulated through A-kinase anchoring proteins (AKAPs)[83]. dAKAP-1 associates with the outer surface of the mitochondria and orchestrates PKA-dependent local protein synthesis in the peri-mitochondrial space, directly affecting mitochondrial function[84]. In contrast to wildtype PKA, the DP kinase shows reduced binding to d-AKAP1 and other AKAPs and consequently exhibits more diffuse cytosolic localization[58]. Although the mechanism of DP-induced mitochondrial Ca^{2+} changes remains to be elucidated, a requirement for PKA kinase activity suggests that either reduced PKA localization to the mitochondria or novel PKA substrates targeted by DP lead to mitochondrial Ca^{2+} changes in FLC. It also remains to be determined how mitochondrial conditions affect either the expression or stability of KLF15 in FLC. However, from these findings, it is clear that Ca^{2+} signaling is an important component of the bidirectional communication between mitochondria and the rest of the cell.

The MCU/KLF15/BCAA catabolism signaling axis that we identified in FLC may also play a role in other forms of cancer. Based on analysis of the Cancer Genome Atlas (TGCA), the BCAA catabolism pathway was shown to be downregulated in approximately 70% of cancers[48]. Additionally, both suppressed BCAA catabolism and increased uniporter activity have independently been reported to correlate with poor patient prognosis in hepatic cancers[48,85-87]. This raises the intriguing possibility that uniporter-mediated metabolic changes may be a more general mechanism of metabolic regulation in cancer, whereby increased mitochondrial Ca^{2+} levels stimulate TCA cycle activity, downregulate BCAA catabolism, and conserve essential amino acids for protein synthesis and cell proliferation.

2.4 | Methods

2.4.1 | Cell lines and tissue culture

All cell lines were grown in a standard tissue culture incubator (VWR, 75875-212) at 37°C with 5% CO_2. HeLa cells were cultured in DMEM (Thermo Fisher Scientific, 11-965-118) supplemented with 10% FBS (VWR, 89510-186), 2 mM GlutaMAX (Thermo Fisher Scientific, 35-050-061), and 100 IU/mL penicillin and 100 µg/mL streptomycin (VWR, 45000-652). HeLa cells were obtained from the Whitehead Institute for Biomedical Research. The HeLa cell line has the following short tandem repeat profile: D5S818 (11, 12); D13S317 (12, 13.3); D7S820 (8, 12); D16S539 (9, 10); vWA (16, 18); TH01 (7); AMEL (X); TPOX (8, 12); CSF1PO (9, 10). This profile is a 94% match to HeLa Cervical Adenocarcinoma (Human) (CCL-2; ATCC) according to the analysis performed by the ATCC database. AML12 cells were cultured in DMEM/F-12 medium (Gibco, 11330057) supplemented with 10% FBS (VWR, 89510-186), 1x insulin-transferrin-selenium (Gibco, 41400045), 40 ng/mL dexamethasone (MP Biomedicals, 0219456180), and 100 IU/mL penicillin and 100 µg/mL streptomycin (VWR, 45000-652). AML12 cells were obtained from ATCC (CRL-2254, lot #70039497) and CRISPR-edited AML12 DNAJ-PKAc clones c14 and c4 were generated and validated by the Scott Lab as described[41]. All cell lines were tested for mycoplasma using the Genlantis MycoScope PCR Detection Kit (VWR, 10497-508) and were confirmed to be free of mycoplasma contamination.

2.4.2 | Generation of knockout and rescue cell lines

Broad Institute gRNA sequences for MCU (TGAACTGACAGCGTTCACGC) and EMRE (GTCTCAGCCAGGTACCGTCG) were each cloned into the pU6T7 vector (Addgene, 71462). 5 million HeLa cells were resuspended in 400 µL DMEM with 2 µg SpCas9 plasmid (Addgene, 71814), 500 ng gRNA plasmid, and 17.5 µg pUC19 plasmid (Addgene, 50005). The cells and DNA were transferred to a cuvette, incubated on ice for 5 min, and electroporated at 200 V with a capacitance of 950 µF and pulse length of 23 ms. Electroporated cells were allowed to grow to confluence on a 10 cm plate before being diluted to 1 cell/200 µL and plated in 96-well plates to obtain single cell clones. HeLa MCU KO and EMRE KO clones were verified by Western blotting, functional assays, and sequencing. To rescue MCU expression, MCU KO clone 18 was infected with lentivirus containing an MCU-FLAG construct with the sequence below. Following resistance marker selection, single cell clones were isolated and screened for MCU expression by Western blot.

2.4.3 | MCU-FLAG DNA sequence

ATGGCGGCCGCCGCAGGTAGATCGCTCCTGCTGCTCCTCTCCTCTCGGGGCGGCGGCG
GCGGGGGCGCCGGCGGCTGCGGGGCGCTGACTGCCGGCTGCTTCCCTGGGCTGGGCG
TCAGCCGCCACCGGCAGCAGCAGCACCACCGGACGGTACACCAGAGGATCGCTTCCTG

GCAGAATTTGGGAGCTGTTTATTGCAGCACTGTTGTGCCCTCTGATGATGTTACAGTG
GTTTATCAAAATGGGTTACCTGTGATATCTGTGAGGCTACCATCCCGGCGTGAACGCT
GTCAGTTCACACTCAAGCCTATCTCTGACTCTGTTGGTGTATTTTTACGACAACTGCAA
GAAGAGGATCGGGGAATTGACAGAGTTGCTATCTATTCACCAGATGGTGTTCGCGTTG
CTGCTTCAACAGGAATAGACCTCCTCCTCCTTGATGACTTTAAGCTGGTCATTAATGAC
TTAACATACCACGTACGACCACCAAAAAGAGACCTCTTAAGTCATGAAAATGCAGCAA
CGCTGAATGATGTAAAGACATTGGTCCAGCAACTATACACCACACTGTGCATTGAGCA
GCACCAGTTAAACAAGGAAAGGGAGCTTATTGAAAGACTAGAGGATCTCAAAGAGCA
GCTGGCTCCCCTGGAAAAGGTACGAATTGAGATTAGCAGAAAAGCTGAGAAGAGGAC
CACTTTGGTGCTATGGGGTGGCCTTGCCTACATGGCCACACAGTTTGGCATTTTGGCC
CGGCTTACCTGGTGGGAATATTCCTGGGACATCATGGAGCCAGTAACATACTTCATCA
CTTATGGAAGTGCCATGGCAATGTATGCATATTTTGTAATGACACGCCAGGAATATGT
TTATCCAGAAGCCAGAGACAGACAATACTTACTATTTTTCCATAAAGGAGCCAAAAAGT
CACGTTTTGACCTAGAGAAATACAATCAACTCAAGGATGCAATTGCTCAGGCAGAAAT
GGACCTTAAGAGACTGAGAGACCCATTACAAGTACATCTGCCTCTCCGACAAATTGGT
GAAAAAGATTCTAGAGGTGGATCTGGTGGATCTGGTGGATCTATGGATTACAAGGAT
GACGATGACAAG

2.4.4 | Proliferation assays

20,000 HeLa cells were plated in 6-well plates on day 0. On days 2, 3, and 5, the media was aspirated, and the cells were washed with PBS (Thermo Fisher Scientific, 20012050), detached with 200 µL trypsin solution (Gibco, 12605-010), and then resuspended in 1.8 mL media for a total volume of 2 mL. The resuspended cells were counted using a Beckman Coulter Z2 Cell and Particle Counter (Beckman Coulter, 383550). 100,000 AML12 cells were plated in 10 cm plates on day 0. On days 2, 3, and 4, the media was aspirated, and the cells were washed with PBS (Thermo Fisher Scientific, 20012050), detached with 2 mL trypsin solution (Gibco, 12605-010), and then resuspended in 4 mL media, for a total volume of 6 mL. The resuspended cells were counted using a Coulter Z2 Cell and Particle Counter (Beckman Coulter, 383550).

For BT2 treatment experiments, 100,000 HeLa cells were plated in 6-well plates on day 0 with 10 μM BT2 (MedChem Express, HY-114855) or DMSO (Sigma-Aldrich, D8418). On day 3, cells were harvested and counted as described above.

2.4.5 | Mass spectrometry sample preparation

Five replicates of 500,000 WT and MCU KO HeLa cells were plated in 10 cm plates. After 48 hr, the media was aspirated, and cells were washed with cold PBS (Thermo Fisher Scientific, 20012050) and lysed with 350 μL fresh lysis buffer consisting of 8 M urea (Sigma-Aldrich, U5128), 1 M Tris, 1 M tris(2-carboxyethyl)phosphine hydrochloride (TCEP, Sigma-Aldrich, C4706), and 0.6 M 2-chloroacetamide (CAM, Sigma-Aldrich, C0267). Lysates were sonicated on ice for 10 min with 30 sec on/off pulses at an amplitude setting of 100 in a cup-horn sonicator . Samples were vortexed at 1400 rpm on a thermomixer (Eppendorf) for 30 min at 37 °C. Samples were then centrifuged at 17,000 g for 10 min at 4 °C, and 175 μL of the supernatant was transferred to a new tube. 700 μL cold acetone was added to each sample. 43.75 μL Trichloroacetic acid (TCA, Sigma-Aldrich, T4885) was then added for a final concentration of 5%. The samples were vortexed briefly at 1400 rpm and stored overnight at -20 °C. Samples were centrifuged at

6,000 g for 10 min at 4 °C, and the supernatant was aspirated. 500 µL cold acetone was added to the pellet, and the pellet was sonicated in an ice bath until the pellet was dissolved (5-10 min). The samples were incubated on ice for another 15 min then centrifuged at 6,000 g for 10 min at 4 °C. The supernatant was aspirated, and the pellets were air dried for 2-3 min. Samples were resuspended in 200 µL 8 M urea, 100 mM Tris solution. Samples were vortexed for 1 hr at 37 °C to dissolve the pellet in solution. Protein concentrations were measured with the Pierce 660 nm Protein Assay (Thermo Fisher Scientific, 22660) and 500 µg of protein per sample was used for subsequent mass spectrometry experiments. Samples were diluted 1:1 with 100 mM triethylammonium bicarbonate (TEAB, Sigma, T7408), reducing the urea concentration to 4 M. A stock of 2 µg/µL Lys-C endoproteinase (Fujifilm Wako Chemicals, 121-05063) was added to each sample for an enzyme:protein ratio of 1:100. Samples were vortexed at 1400 rpm for 2 hr at 37 °C. Samples were again diluted 1:1 with 100 mM TEAB, bringing the urea concentration to 2 M. 0.5 µg/µL stock of trypsin (Promega, V5111) dissolved in 40 mM acetic acid was added to each sample for an enzyme:protein ratio of 1:100. Samples were vortexed at 1400 rpm overnight at 37 °C.

The following day, HPLC-grade formic acid (Sigma, 5438040100) was added for a final concentration of 2% by volume. Samples were centrifuged at 11,000 g for 5 min. 5% of the supernatant was used for stage tipping. C_{18} StageTips were made as described in Rappsilber *et al.*[88]. StageTips were washed with sequential washes of 50 µL HPLC-grade methanol (Sigma, 494291), Buffer B, and Buffer A, centrifuging the tips at 1,800 g for 2 min between each wash. Buffer B consisted of 0.1% HPLC-grade trifluoroacetic acid (TFA, Alfa Aesar, AA446305Y) and 80% HPLC-grade acetonitrile (Sigma-Aldrich, 271004).

Buffer A consisted of 0.1% TFA and 5% acetonitrile. Samples were loaded on the StageTips, centrifuged at 1,800 g for 2 min, and washed again with Buffer A.

2.4.6 | LC-MS/MS-based proteomics and data analysis

Peptide samples were separated on an EASY-nLC 1200 System (Thermo Fisher Scientific) using 20 cm long fused silica capillary columns (100 µm ID, laser pulled in-house with Sutter P-2000, Novato CA) packed with 3 µm 120 Å reversed phase C18 beads (Dr. Maisch, Ammerbuch, DE). The LC gradient was 90 min long with 5–35% B at 300 nL/min. LC solvent A was 0.1% (v/v) aq. acetic acid and LC solvent B was 20% 0.1% (v/v) acetic acid, 80% acetonitrile. MS data was collected with a Thermo Fisher Scientific Orbitrap Fusion Lumos. The MS method used was a Data-independent acquisition (DIA) method with a 120K resolution MS1 scan from m/z 395-1005 and 15K resolution MS2 scans with 12 Th isolation with between m/z 400-1000; the AGC target was 400,000 ions with a max injection time of 25 ms. Raw files were analyzed with MSFragger 3.4[89] and DIA-nn 1.8[90] using protein and peptide FDRs of 0.01. The FASTA database used for search was a human Uniprot reference database downloaded 2021-11-08, with ‘stricttrypsin’ and 2 missed cleavages permitted. Variable modifications were N-term acetylation, pyroGlu- and loss of ammonia (-17.0265 nQnC) at peptide N-termini. Carbamidomethyl (C) was a fixed modification. Data was further processed using the Perseus software package (version 1.5.2.6), the R environment, Origin Pro 8.0 and Microsoft Excel. GO term enrichment analysis was performed using the ShinyGO 0.76 web application (http://bioinformatics.sdstate.edu/go/)[34].

2.4.7 | RNA sequencing

500,000 HeLa cells were plated in 6-well plates. After two days, total RNA was isolated using an RNeasy kit (Qiagen, 74106). Samples were sent to Genewiz for sequencing and data analysis, as follows: Samples underwent mRNA enrichment, mRNA fragmentation, and random priming. Genewiz performed first and second strand cDNA synthesis followed by end repair, 5' phosphorylation, and dA-Tailing. cDNA was sequenced, following adaptor ligation and enrichment by PCR. During analysis, the reads were trimmed and mapped to the Homo sapiens GRCh38 reference genome available [91] (https://www.ensembl.org) using the STAR aligner (v.2.5.2b). Hit counts for genes and exons were calculated with featureCounts (Subread package, v.1.5.2). DESeq2 was used for analysis of differential gene expression. p-values and log2 fold changes were determined with the Wald test, and genes with an adjusted $p\text{-value} < 0.05$ and absolute $\log_2$ fold change > 1 were considered to be differentially expressed. Additional RNA sequencing data from FLC patients was obtained from GSE250059.

2.4.8 | Seahorse metabolic flux analysis

HeLa and AML12 cells were seeded at 10,000 or 15,000 cells/well, respectively, in a XFe96 Microplate (Agilent Technologies, 103792-100) and cultured overnight at 37°C in 5% CO_2. The Extracellular Flux Assay Kit oxygen probes (Agilent Technologies, 103792-100) were activated in XF calibrant buffer (Agilent, 100840-000) at 37°C in a non-CO_2 incubator overnight. Seahorse XF medium was prepared fresh by supplementing XF DMEM Medium, pH 7.4 (Agilent, 103575-100) with 100 mM Pyruvate Solution (Agilent, 103578-100), 1 M Glucose Solution (Agilent, 103577-100), and 200 mM L-Glutamine

(Fisher Scientific, BP379-100). The cell culture medium was removed from the plate and the cells were washed once with pre-warmed Seahorse XF medium and replaced with fresh medium a second time. The cells were then incubated in a CO_2-free incubator at 37°C for 1 hr. Oxygen consumption rate (OCR) measurements were performed with a Seahorse XFe96 Extracellular Flux Analyzer (Agilent, S7800B) using the Cell Mito Stress Test program. The sensor cartridge was loaded with the drugs and inserted into the machine 30 min prior to the flux assay to calibrate the oxygen probes. Following measurements of baseline cellular respiration, respiration was measured after addition of oligomycin, carbonyl cyanide-p-trifluoromethoxyphenylhydrazone (FCCP), antimycin A, and rotenone with final concentrations of 1 μM. Oxygen consumption rate was analyzed with the Seahorse XF Cell Mito Stress Test Report Generator (Wave Software). OCR measurements were normalized to cell number as determined by the CyQUANT Cell Proliferation Assay Kit (Thermo Scientific, C7026) or DAPI staining for HeLa and AML12 cells, respectively. For the CyQUANT assay, the media was removed from each well and the plates were frozen at -80 °C for >1 hr to lyse the cells. CyQUANT was utilized per manufacturer's instructions to measure fluorescence intensity (Ex 480 nm, Em 520 nm). For DAPI staining, 40 μL media was left in each well and cells were frozen at -80 °C for >1 hr to lyse the cells. After thawing, 100 μL 1 μg/μL DAPI (Thermo Scientific, 62248) was added to each well for 5 min before measuring DAPI fluorescence (Ex 359 nm, Em 457 nm).

2.4.9 | LC-MS-based lipid analysis

Cell pellets containing 10 million HeLa cells per condition were frozen at -80 °C until lipid extraction. Lipid extraction and analysis were carried out as described[92]. Briefly, cell pellets were resuspended in methanol and sonicated 3x30 sec while on ice. The homogenized solution was centrifuged at 16,900 g for 15 min at 4 °C. 800 µL of supernatant was removed into a fresh 4-dram vial. 1 mL cold methanol was added to the remaining pellet, sonicated, and centrifuged again. This supernatant was combined with the previous extract and dried down using a nitrogen evaporator. LC-MS data was acquired using an Agilent 1260 HPLC with an Agilent 6530 Quadrupole Time-of-Flight mass spectrometer. A Luna C5 reverse-phase column (5m, 4.6 x 50mm, Phenomenex) was used for positive mode and a Gemini C18 reversed-phase column (5m, 4.6 x 50mm, Phenomenex) was used in negative mode. Mobile phase A was 95:5 water:methanol and mobile phase B was 60:35:5 isopropanol:methanol:water for both negative and positive modes. The mobile phases contained additives to aid electrospray ionization and improve ion detection (0.1% formic acid in positive mode; 5 mM ammonium formate, and 0.1% ammonium hydroxide in negative mode). Data acquisition in positive and negative mode used different gradients: ramping from 0% mobile phase B to 100% mobile phase B occurred over 45 min and 65 min for positive and negative mode, respectively. For both methods, the flow rate was set to 0.1 mL/min for the first 5 min at 100% mobile phase A then increased to 0.5 mL/min for the remainder of the run. A dual electrospray ionization source was used; capillary and fragmentor voltages were set to 3500 V and 175 V, respectively. All data were collected in the extended dynamic range mode (m/z = 50 - 1,700). Representative lipid species for each class were targeted by extracting the corresponding m/z for each ion in MassHunter Qualitative Analysis software (version B.06.00, Agilent Technologies). Peak areas were manually integrated and represented as abundance. Relative abundance values were calculated by dividing the abundance of a lipid by the average abundance of that lipid in the wildtype set.

2.4.10 | 13C6 leucine carbon tracing

800,000 Hela WT & MCU KO cells were plated in two 6-well plates to achieve 85-95% confluency. The next day, one plate was washed twice with PBS (Thermo Fisher Scientific, 20012050), and the medium was changed to DMEM/F-12 + 13C6 leucine. DMEM/F-12 + 13C6 leucine medium was prepared from DMEM/F-12 stock w/o glucose or amino acids (US Biological, D9807-02A) supplemented with 10 mM L-Leucine-13C6 (MedChem Express, HY-N0486S2),10% dialyzed FBS (VWR, 89510-186), 1x insulin-transferrin-selenium (Gibco, 41400045), 40 ng/mL dexamethasone (MP Biomedicals, 0219456180), and 100 IU/mL penicillin and 100 µg/mL streptomycin (VWR, 45000-652) and amino acid solution (except leucine) with concentrations matching regular DMEM/F-12 (Thermo Scientific, 21041025). FBS dialysis was done with Slide-A-Lyzer™ Dialysis Flasks (ThermoFisher Scientific, 87761) with a 3.5kD molecular weight cut off. DMEM/F-12 + 13C6 leucine-treated cells were incubated in 37 °C with 5% CO2 for 2 hrs to ensure that L-Leucine-13C6 was incorporated. The plate was then quickly washed with 1x HPLC-grade ice cold saline which was aspirated before adding 500 µL ice cold 80% HPLC-grade methanol in water. Each well was quickly harvested using a cell scraper. Solution from each well was transferred to a microcentrifuge tube and centrifuged at 17,000 g for 10 min at 4 °C. Equal amounts of supernatant were then taken from each tube and transferred to a fresh microcentrifuge tube which was centrifuged again at 17,000 g for 10 min at 4 °C. Finally, 350 µL of the supernatant of each sample was transferred to a fresh microcentrifuge tube and sent for MS analysis. After sample collection, the second 6-well plate was counted using a Coulter Z2 Cell and Particle Counter (Beckman Coulter, 383550) to obtain cell counts for normalization of each sample.

2.4.11 | NADH/NAD$^+$ measurements

1 million Hela WT and 1.5 million Hela MCU KO cells were plated in DMEM media (Thermo Fisher Scientific, 11-965-118) supplemented with 10% FBS (VWR, 89510-186), 2 mM GlutaMAX (Thermo Fisher Scientific, 35-050-061), 100 IU/mL penicillin and 100 µg/mL streptomycin (VWR, 45000-652) and allowed to reach 80% confluency. The medium was aspirated and rinsed with PBS (Thermo Fisher Scientific, 20012050), and replaced with DMEM:F12 w/o Glucose, Amino Acids (US Biological, D9807-02A) that was supplemented with dialyzed 10% FBS, 100 IU/mL penicillin and 100 µg/mL streptomycin, glucose, and either non-branched-chain amino acids or all amino acids. Plates were incubated for 3 hr at 37°C in 5% CO_2. Cells were detached with trypsin and resuspended in the appropriate media (BCAA-free or BCAA-containing media) spun down at 800 g for 3 min to remove any remaining trypsin then resuspended in 4 mL of the appropriate media. Cells were counted with the Coulter Z2 Cell and Particle Counter (Beckman Coulter, 383550) and two samples of 1 million cells were aliquoted for each cell line, one aliquot for an NAD$^+$ measurement and the second for the NADH measurement, adapted from the NAD$^+$/NADH Assay Kit (Sigma-Aldrich, MAK460) protocol. Sample preparation and working reagents from this point follows the kit's protocol. The fluorescence was read at Ex = 530 nm, and Em = 585 nm with the BioTek Synergy H1

plate reader (Fisher Scientific, 11-120-536) immediately after working reagent was added to the prepared sample and after 10 min. NAD^+ or NADH concentrations were calculated from the delta fluorescence using the standard curve established with reagents from the kit. These concentrations were used to calculate the $NADH/NAD^+$ ratio and subsequent fold changes.

2.4.12 | Cell lysate preparation and immunoblots

Cells were grown to 40-80% confluency, then plates were washed with cold PBS (Thermo Fisher Scientific, 20012050) on ice and lysed with either RIPA or triton lysis buffer. RIPA buffer consisted of 50 mM HEPES-KOH, pH 7.4 (Sigma-Aldrich, H3375; Sigma Millipore, 1050121000), 150 mM NaCl (Sigma-Aldrich, 746398), 2 mM EDTA (Sigma-Aldrich, 607-429-00-8), 10 mM sodium pyrophosphate (Sigma-Aldrich, 71501), 10 mM β-glycerophosphate (Sigma-Aldrich, G9422), 1% sodium deoxycholate (Sigma-Aldrich, D6750), 0.1% SDS (Sigma-Aldrich, L4509), and 1% Triton X-100 (Sigma-Aldrich, X100). Triton buffer consisted of 50 mM HEPES-KOH, pH 7.4, 40 mM NaCl, 2 mM EDTA, 10 mM β-Glycerophosphate, 1.5 mM sodium orthovanadate (Sigma-Aldrich, S6508), 50 mM sodium fluoride (Sigma-Aldrich, S7920), 10 mM sodium pyrophosphate, and 1% Triton X-100. Lysis buffers were supplemented with protease inhibitors (Sigma-Aldrich, 11836170001) immediately prior to lysis. Lysates were centrifuged at 17,000 g for 10 min at 4°C. The supernatants were normalized by protein concentration as measured by either a Bradford protein assay (Bio-Rad, 5000205) or Pierce BCA assay (Thermo Fisher Scientific, 23209) and a BioTek Synergy H1 plate reader (Fisher Scientific, 11-120-536). SDS-PAGE samples were prepared from the lysates with 5X reducing sample buffer (pH 6.8) consisting of 10% SDS, 25% 2-mercaptoethanol (Sigma-Aldrich, M3148), 25% glycerol (Sigma-Aldrich, G5516), 50 mM Tris-HCl (Sigma-Aldrich, RDD008), and 0.1% bromophenol blue (VWR, 97061-690).

Samples were heated to 95 °C for 5 min and then brought to room temperature. Samples were mixed by pipetting and loaded onto 4-15% gradient Mini-PROTEAN TGX gels (Bio-Rad, 4561086). Following gel electrophoresis in Tris-Glycine-SDS running buffer (Boston BioProducts, BP-150), proteins were transferred to ethanol-activated 0.2 µm PVDF membranes (Bio-Rad, 1620174) using the BioRad Mixed Molecular Weight Protein Transfer setting (7 min, 1.3 A, 25 V) on the Trans-Blot Turbo Transfer System (Bio-Rad, 1704150) with Trans-Blot Turbo Transfer Buffer (Bio-Rad, 10026938). After transfer, membranes were washed in 20% ethanol for ~2 min and checked for equal loading and even transfer by Ponceau stain (Sigma-Aldrich, P7170). Membranes were then incubated with 1% wt/vol BSA (Sigma-Aldrich, A2153) in TBST with 1% Tween-20 (Boston Bio-Products, IBB-180) at room temperature for 1-4 hr. Membranes were incubated overnight with primary antibody and 1% BSA in TBST at 4 °C. All membranes were then washed with TBST three times, 5 min each, and incubated with secondary antibody and 1% BSA in TBST for 1 hr using a BlotCycler W5 (Precision Biosystems). Membranes were washed 4 times, 5 min each, with TBST. Membranes were developed using Clarity Western ECL substrate (Bio-Rad, 170-5060) or Clarity Max Western ECL substrate (Bio-Rad, 1705062). Immunoblots were imaged with a iBrightCL1000 imager (Life Technologies, A23749) and quantified using the Image Studio Lite software, version 5.2 (LI-COR Biosciences). The following antibodies and dilutions were used: 1:3000 rabbit ACAT1 antibody (ABclonal, A13273); 1:3000 rabbit BCKDHA antibody (ABclonal, A21588); 1:5000 mouse β-actin antibody (Cell Signaling Technology, 3700); 1:5000 rabbit EMRE antibody (Bethyl Laboratories, A300-BL19208); 1:3000 rabbit HSP60 antibody (Cell Signaling Technology, 12165); 1:3000 rabbit KLF15 antibody (ABclonal, A7194); 1:3000 rabbit MCEE antibody (ABclonal, A14430); 1:3000 rabbit MCU antibody (Cell Signaling Technology, 14997); 1:3000 rabbit MICU1 antibody (ABclonal, A21948); 1:3000 rabbit MMSDH antibody (ABclonal, A3309); 1:3000 rabbit MMUT antibody (ABclonal, A3969); 1:1000 mouse OTC antibody (Invitrogen, PAS-28197); 1:3000 rabbit PCCB antibody (ABclonal, A5415); 1:3000 rabbit phospho-BCKDH-E1α, human S292/mouse S293 antibody (Cell Signaling Technology, 40368); 1:1000 rabbit phospho-R-X-S*/T* (Cell Signaling Technology, 9621); 1:3000 rabbit PKA-Cα antibody (BD Biosciences, 610980); 1:3000 rabbit TOM20 antibody (Cell Signaling Technology, 42406); 1:10,000 HRP-linked α-rabbit secondary antibody (Cell Signaling Technology, 7074); 1:10,000 HRP-linked α-mouse secondary antibody (Cell Signaling Technology, 7076).

2.4.13 | Isolation of patient samples

Fresh non-tumor liver (NTL) and FLC tumor samples were procured from patients undergoing liver resection for FLC. Prior to surgery, written-informed consent was obtained for tissue donation under a research protocol approved by the University of Washington Institutional Review Board (IRB) (#1852) and Seattle Children's Hospital IRB (#15277). All research samples were de-identified. Clinical details for each patient are outlined in Supplemental Table 1. NTL and FLC samples were processed and transferred to the laboratory on ice within 1 hr of tissue excision. Samples were stored at -80 °C prior to lysate preparation.

2.4.14 | Lysis and sample preparation of patient samples

Tissues were lysed with protease inhibitor-supplemented RIPA buffer using a TissueRuptor homogenizer (Qiagen, 9002755). Tissues were homogenized until they were a uniform consistency. Samples were then centrifuged at 17,000 g for 10 min at 4 °C and prepared for SDS-PAGE with 5X reducing sample buffer.

2.4.15 | Generation of shRNA constructs

ShRNA sequences were designed by the RNAi Consortium (TRC) of the Broad Institute. Forward and reverse oligos encoding the shRNA were annealed to form dsDNA. 100 pmol forward oligo and 100 pmol reverse oligo were resuspended in 25 µL 1x NEBuffer 2 (NEB, B7002S). The solution was incubated in a 95 °C water bath for 4 min then slowly cooled (~0.5 °C/min) to room temperature. The pLKO.1 vector (Addgene, 10878) was digested with AgeI-HF (NEB, R3552) and EcoRI-HF (NEB, R3101) and ligated with the oligo solution according to the NEB Quick Ligase (NEB, M2200) protocol. The ligation mixture was transformed into XL10-Gold competent cells (Agilent, 200315). Resulting plasmids were verified by sequencing.

Mouse shMCU-1, forward oligo:

CCGGGATCCGAGATGACCGTGAATCCTCGAGGATTCACGGTCATCTCGGATCTTTTTG;

reverse oligo:

AATTCAAAAAGATCCGAGATGACCGTGAATCCTCGAGGATTCACGGTCATCTCGGATC.

Mouse shMCU-2, forward oligo:

CCGGTAGGGAATAAAGGGATCTTAACTCGAGTTAAGATCCCTTTATTCCCTATTTTTG;

reverse oligo:

AATTCAAAAATAGGGAATAAAGGGATCTTAACTCGAGTTAAGATCCCTTTATTCCCTA.

Human shMCU-A forward oligo:

CCGGGCAAGGAGTTTCTTTCTCTTTCTCGAGAAAGAGAAAGAAACTCCTTGCTTTTTG

reverse oligo:

AATTCAAAAAGCAAGGAGTTTCTTTCTCTTTCTCGAGAAAGAGAAAGAAACTCCTTGC

Human shMCU-B forward oligo:

CCGGCCAGCAACTATACACCACACTCTCGAGAGTGTGGTGTATAGTTGCTGGTTTTTG

reverse oligo:

AATTCAAAAACCAGCAACTATACACCACACTCTCGAGAGTGTGGTGTATAGTTGCTGG

shGFP control, forward oligo:

CCGGCCACATGAAGCAGCACGACTTCTCGAGAAGTCGTGCTGCTTCATGTGGTTTTTG;

reverse oligo:

AATTCAAAAACCACATGAAGCAGCACGACTTCTCGAGAAGTCGTGCTGCTTCATGTGG

shRFP control, forward oligo:

CCGGGCTCCGTGAACGGCCACGAGTCTCGAGACTCGTGGCCGTTCACGGAGCTTTTTG

reverse oligo:

AATTCAAAAAGCTCCGTGAACGGCCACGAGTCTCGAGACTCGTGGCCGTTCACGGAGC

2.4.16 | Lentivirus production and transduction

1 million HEK293T cells (from the Whitehead Institute for Biomedical Research) were plated in 6 cm plates. The following day, cells were transfected. 100 ng p-CMV-VSV-G (Addgene, 8454), 900 ng psPax2 (Addgene, 12260), and 1 µg viral plasmid were diluted in 6 µL X-tremeGENE 9 DNA transfection reagent (Sigma-Aldrich, 6365787001) and 150 µL DMEM and incubated at room temperature for 15 min before being added to the cells. After 36-48 hr, the virus-containing medium was filtered through a 0.45 µm sterile filter (VWR, 28145-505) and stored at -80 °C until use. 200,000 HeLa or 100,000 AML12 cells were plated in 6-well plates. The following day, 200 µL of the virus-containing media and 8 µg/mL polybrene (Sigma-Aldrich, H9268) was added to the cells. Infected cells were selected for 48 hr with 2 µg/mL puromycin. For assays measuring transcriptional changes in the BCAA catabolism pathway, shMCU-infected cells were cultured for 2-3 weeks prior to harvesting.

2.4.17 | RNA isolation, cDNA synthesis, qPCR

AML12 cells were grown in 6-well plates to ~80% confluency in triplicate. Tumor and non-tumor liver samples were stored in RNALater solution at -80 °C prior to RNA extraction. RNA was isolated with the RNeasy Kit (Qiagen, 74106). For liver samples, ~30 mg of tissue was homogenized using a TissueRuptor homogenizer (Qiagen, 9002755) according to the kit protocol. 100 ng of RNA was used for cDNA synthesis using the Maxima First Strand cDNA synthesis kit (Thermo Fisher Scientific, K1641) according to kit instructions. The resulting cDNA was diluted 1:30 in dH_2O, and either 1 or 2 µL of diluted cDNA was used for qPCR using Applied Biosystems TaqMan Fast Advanced Master Mix (Thermo Fisher Scientific, 44-445-57) in a 384-well plate (Thermo Fisher

Scientific, 43-098-49) using a QuantStudio 5 RT-PCR System (Thermo Fisher Scientific). The following Taqman probes were used: human ACTB (Thermo Fisher Scientific, 4331182-Hs01060665_g1), human MCU (Thermo Fisher Scientific, 4331182-Hs00293548_m1), and human OTC (Thermo Fisher Scientific, 4331182-Hs00166892_m1).

2.4.18 | Immunohistochemistry

Fresh human FLC tissue from liver resections were fixed in formalin and paraffin embedded. 4 µm thick sections were cut and placed on glass slides. Slides were stained with Hematoxylin and Eosin (H&E) using a H&E staining kit (Vector Laboratories, H-3502) according to supplied protocol. For immunohistochemistry staining, slides were deparaffinized, rehydrated, and washed with TBST. After antigen retrieval in 10 mM sodium citrate (pH 6) and quenching of endogenous peroxidase activity with 3% H_2O_2, samples were blocked with 2.5% normal horse serum (NHS) before incubation with primary antibodies overnight at 4°C. The following primary antibodies were used: 1:300 KLF15 rabbit antibody (ABclonal, A7194) and 1:250 MCU rabbit antibody (Cell Signaling Technologies, 14997). Negative controls were treated with 2.5% NHS without primary antibodies. Signals were processed using the ImmPRESS HRP Horse Anti-Mouse (Vector Laboratories, MP-7402) and Anti-Rabbit (Vector Laboratories, MP-7401) Peroxidase Kits and ImmPACT DAB Substrate Kit Peroxidase (Vector Laboratories, SK-4105) according to manufacturer's protocol. Slides were counterstained with Hematoxylin QS, dehydrated, and mounted with VectaMount Express Mounting Medium.

2.4.19 | Ca^{2+} uptake in permeabilized cells

Protocol is adapted from Sancak *et al.*[10]. Cell medium was changed 1-2 hr prior to harvesting. Cells were detached with trypsin (Gibco, 12605-010) and resuspended in cell medium. 1 million HeLa cells or 0.5 million AML12 cells were centrifuged at 800 g for 3 min. Cell pellets were washed with PBS (Thermo Fisher Scientific, 20012050), centrifuged at 800 g for 3 min, and resuspended in 150 µL KCl buffer. KCl buffer consists of 125 mM KCl (Sigma-Aldrich, 793590), 2 mM K_2HPO_4 (Sigma-Aldrich, P3786), 1 mM $MgCl_2$, (Sigma-Aldrich, M8266), and 20 mM HEPES, pH 7.2 (Sigma-Aldrich, H3375) supplemented fresh with 5 mM glutamate (Sigma-Aldrich, G1251), 5 mM malate (Sigma-Aldrich, M7397), and 1 µM Oregon Green 488 Bapta-6F (Invitrogen, O23990). 0.01% or 0.005% digitonin (Thermo Fisher Scientific, BN2006) was added for HeLa and AML12 cell assays, respectively. Cells were transferred to a black 96-well plate (Greiner Bio-One, 655076). Fluorescence (Ex 485/20 nm, Em 520/20 nm) was monitored every 2 sec for 136 sec at room temperature using a BioTek Synergy H1 microplate reader (Fisher Scientific, 11-120-536) before and after injection of 50 µM $CaCl_2$ (Sigma-Aldrich, 746495). Ca^{2+} uptake rates were calculated using the linear fit of uptake data points between 20 and 30 sec after Ca^{2+} injection. A maximum of eight samples were assayed together, including one wildtype control per assay run.

2.4.20 | Ca^{2+} release from permeabilized cells

Cell medium was changed 1-2 hr prior to harvesting. Cells were detached with trypsin (Gibco, 12605-010) and resuspended in cell medium. 1 million HeLa cells or 0.5 million AML12 cells were centrifuged at 800 g for 3 min. Cell pellets were washed with

PBS (Thermo Fisher Scientific, 20012050), centrifuged at 800 g for 3 min, and resuspended in 150 µL KCl buffer. KCl buffer consists of 125 mM KCl (Sigma-Aldrich, 793590), 2 mM K_2HPO_4 (Sigma-Aldrich, P3786), 1 mM $MgCl_2$, (Sigma-Aldrich, M8266), and 20 mM HEPES, pH 7.2 (Sigma-Aldrich, H3375) supplemented fresh with 1 µM Oregon Green 488 Bapta-6F (Invitrogen, O23990). 0.01% or 0.005% digitonin (Thermo Fisher Scientific, BN2006) was added for HeLa and AML12 cell assays, respectively. Cells were transferred to a black 96-well plate (Greiner Bio-One, 655076). Fluorescence (Ex 485/20 nm, Em 520/20 nm) was monitored every 2 sec for 196 sec at room temperature using a BioTek Synergy H1 microplate reader (Fisher Scientific, 11-120-536) before and after injection of 1 µM CCCP (Cayman Chemical Company, 25458) in KCl buffer. Ca^{2+} release was calculated using the absolute difference between fluorescence reads prior to CCCP injection (average of six values, 0-10 sec) and 3 min after injection (average of six values, 186-196 sec). A maximum of eight samples were assayed together, including one wildtype control per assay run. For PKA kinase inhibition assays, AML12 cells were cultured for 4 days with 5 µM BLU2864 or DMSO vehicle control. Cells were passaged on day 2, and fresh medium and drug were added. Ca^{2+} release experiments with BLU2864 were performed with ~0.5 million cells, however BLU2864-treated cells formed clumps and could not be counted precisely. Data were instead normalized by protein concentration. Following Ca^{2+} release, 1 µL Triton X-100 (Sigma-Aldrich, X100) was added to each well, and the solution was pipetted vigorously. Protein concentration was then determined by Bradford assay (Bio-Rad, 5000205).

2.4.21 | TEM of FLC patient liver

Tissue fixation was performed with 4% glutaraldehyde in 0.1 M sodium cacodylate buffer, then stored overnight at 4 °C. The tissue was then washed 5 x 5 min in buffer at room temperature and post fixed in buffered 2% osmium tetroxide on ice for 1 hr. This was followed by 5 washes in ddH_2O, then en bloc staining in 1% uranyl acetate (aqueous), overnight at 4 °C. The following day the tissue was washed 5 x 5 minutes in ddH_2O then dehydrated in ice cold 30%, 50%, 70%, and 95% ethanol, then allowed to come to room temperature. This was followed by 2 changes of 100% ethanol and two changes of propylene oxide. The tissue was then infiltrated in a 1:1 mixture of propylene oxide:Epon Araldite resin for 2 hr followed by two changes of fresh Epon Araldite, 2 hr each change. It was then placed in flat embedding molds and polymerized at 60 °C overnight. Fixed samples were sliced to a thickness of 80 nm and were imaged on a JEOL1230 Transmission Electron Microscope (TEM) operated at 80 kV.

2.4.22 | Quantification of mitochondria and deposits from EM images

Images of patient liver tissue taken at 10,000x magnification were analyzed by two independent, blinded researchers. First, mitochondria were identified in each image. Mitochondria were characterized as structures with a well-defined, curved border, typically 0.5-1 µm in diameter, with a mottled, gray matrix and at least one visible cristae line. Confirmed mitochondria were examined for the presence or absence of black, electron-dense deposits. Deposits were defined as speckles that were both darker and thicker in diameter than cristae membrane lines. With FLC patient 42.2, for which no non-tumor liver sample was available, cells from the tumor periphery were classified as oncocytic or peri-oncocytic. Cells with a circular nucleus and dispersed mitochondria were classified as peri-oncocytic; cells with misshapen nuclei and abundant cytoplasmic mitochondria were classified as oncocytic.

2.4.23 | TMRM measurements

500,000 AML12 cells were centrifuged at 800 g for 3 min, washed with 1 mL PBS (Thermo Fisher Scientific, 20012050), and centrifuged again at 800 g for 3 min. The supernatant was aspirated and the cell pellet was resuspended in 150 µL KCl buffer (for composition, see Ca^{2+} uptake protocol above) supplemented with 500 nM tetramethylrhodamine methyl ester (TMRM, Thermo Fisher Scientific, I34361) and 0.005% digitonin (Thermo Fisher Scientific, BN2006). Cell suspension was transferred to a black 96-well plate (Greiner Bio-One, 655076). Fluorescence measurements (Ex 540 nm, Em 590 nm) were taken across three periods using a BioTek Synergy H1 microplate reader (Fisher Scientific, 11-120-536). The first measurements were taken every second for 1 min to establish a baseline. Then 500 mM glutamate (Sigma-Aldrich, G1251) and 5 mM malate (Sigma-Aldrich, M7397) stocks were injected for final concentrations of 5 mM, and a second reading was taken every second for 1 min to obtain the minimum fluorescence, corresponding with maximal mitochondrial membrane potential. Finally, mitochondrial membrane potential was dissipated with the addition of 1 µM CCCP (Cayman Chemical Company, 25458), and reads were taken every second for 2 min to obtain the maximum fluorescence. Relative mitochondrial membrane potential was reported as the difference between the maximum (average of data from 294-304 sec) and minimum TMRM fluorescence measurements (average of data from 172-182 sec).

2.4.24 | Generation of mito-GECO constructs and matrix and cytosolic Ca^{2+} measurements

The pLMM1 vector was generated from pLYS1[93] by replacing the CMV promoter with the EF1α promoter. G-GECO1.1[43] was cloned into either pLYS1 or pLMM1 with an N-terminal mitochondrial targeting sequence taken from cytochrome C subunit 8A (COX8). AML12 cells were transduced with mito-G-GECO lentiviral constructs generated using pLYS1 (WT and c14) or pLMM1 (c4) and selected with puromycin as described above. 80,000 AML12 wildtype, c14, and c4 cells expressing mito-G-GECO were cultured in 12-well plates for 2 days until reaching 90-95% confluency. Medium was then aspirated and replaced with 500 µL phenol red-free DMEM/F-12 (Thermo Scientific, 21041025) supplemented with 10% FBS (VWR, 89510-186) and 100 IU/mL penicillin and 100 µg/mL streptomycin (VWR, 45000-652) for 1.5 hr. Fluorescence measurements (Ex 480 nm, Em 520 nm) were obtained with a BioTek Synergy H1 microplate reader (Fisher Scientific, 11-120-536) at 37 °C. To establish baseline, fluorescence was measured every 10 sec for 2 min. Then CCCP was added to a final concentration of 50 µM (Cayman Chemical Company, 25458) to each well, and fluorescence was measured to determine minimum fluorescence. Finally, 5 µL of 1mM stock of ionomycin (Sigma-Aldrich, I3909) and 10 µL of 1M stock of $CaCl_2$ were added, and fluorescence was measured to establish maximum fluorescence. To correct for potential differences in mito-G-GECO expression across cell lines, baseline results were reported as a percentage of the difference between maximum and minimum values. To calculate the baseline fraction, minimum fluorescence is subtracted from baseline fluorescence over minimum fluorescence subtracted from maximum fluorescence. For each measurement, baseline, minimum, and maximum values were determined manually.

AML12 cells were transduced with cyto-G-GECO lentiviral constructs generated using pLYS1 and selected with puromycin as described above. 12-well plates were coated with EmbryoMax® 0.1% Gelatin Solution (Sigma-Aldrich, ES-006) for 10 min. Excess gelatin solution was aspirated, and 80,000 AML12 WT, c14, and c4 cells expressing cyto-G-GECO were cultured in 12-well plates for 2 days until reaching 90-95% confluency. Medium was then aspirated and replaced with 500 µL phenol red-free DMEM/F-12 (Thermo Scientific, 21041025) supplemented with 10% FBS (VWR, 89510-186) and 100 IU/mL penicillin and 100 µg/mL streptomycin (VWR, 45000-652) for 1.5 hr. Fluorescence measurements (Ex 480 nm, Em 520 nm) were obtained with a BioTek Synergy H1 microplate reader (Fisher Scientific, 11-120-536) at 37 °C. To establish baseline, fluorescence was measured every 10 sec for 2 min. Then 5 mM ionomycin (Sigma-Aldrich, I3909) and 2.5 mM EGTA (Sigma-Aldrich, E3889) were added to each well, and fluorescence was measured to determine minimum fluorescence. Finally, 10 mM $CaCl_2$ was added, and fluorescence was measured to establish maximum fluorescence. Relative fluorescence values were reported as described above.

2.5 | Contributions

- NM Marsh: conceptualization, data collection, data analysis, validation, visualization, methodology, and writing
- MJS MacEwen: conceptualization, data collection, data analysis, validation, visualization, methodology, and writing
- J Chea: data collection, data analysis, validation, visualization

- HL Kenerson: data collection, data analysis, visualization
- AA Kwong: data collection, data analysis
- TM Locke: data collection, data analysis
- FJ Miralles: data collection, data analysis
- T Sapre: data collection, data analysis
- N Gozali: data collection
- LB Sullivan: conceptualization, data analysis
- ML Hart: data collection, data analysis
- TS Gulraj:
- GE Atilla-Gokcumen: conceptualization, data collection, data analysis
- S Ong: data collection, data analysis, funding acquisition, visualization
- JD Scott: conceptualization, funding acquisition
- RS Yeung: data collection, data analysis, funding acquisition
- Y Sancak: conceptualization, data collection, data analysis, supervision, funding acquisition, validation, investigation, visualization, methodology, and writing

2.6 | Acknowledgements

We are thankful to the patients who donated samples to be used in research. We are also grateful to Dr. Vishal Gohil and for his thoughtful discussion of this project. We thank Edward Parker for processing patient samples for electron microscopy and his help with image acquisition, Dr. Rong Tien for sharing their KLF15 antibody and plasmids. This work used an EASY-nLC1200 UHPLC and Thermo Scientific Orbitrap Fusion Lumos Tribrid mass spectrometer purchased with funding from a National Institutes of Health SIG grant S10OD021502. Several figures were created with tools from BioRender.com. This research was supported by the Proteomics & Metabolomics Shared Resource, which is supported by a National Cancer Institute Cancer Center Support Grant for the Fred Hutch/University of Washington/Seattle Children's Cancer Consortium (NCI; P30CA015704), R35 GM136234 (Y.S.), Pew Charitable Trusts (Y.S.), 1F31AG072716-01A1 (M.J.S.M), NSF MCB2314338 (G.E.A.G), P30 CA015704 (R.S.Y, H.L.K), DOD W81XWH1910544 (R.S.Y, H.L.K), R01GM129090 (S.E.O), R35GM147118 (L.B.S.).

This chapter was adapted from our preprint manuscript: Marsh, N.M., MacEwen M.J.S., *et al.* Mitochondrial calcium signaling regulates branched-chain amino acid catabolism in fibrolamellar carcinoma. *BioRxiv* (2024).

2.7 | Supplemental Materials

2.7.1 | Supplemental Figures

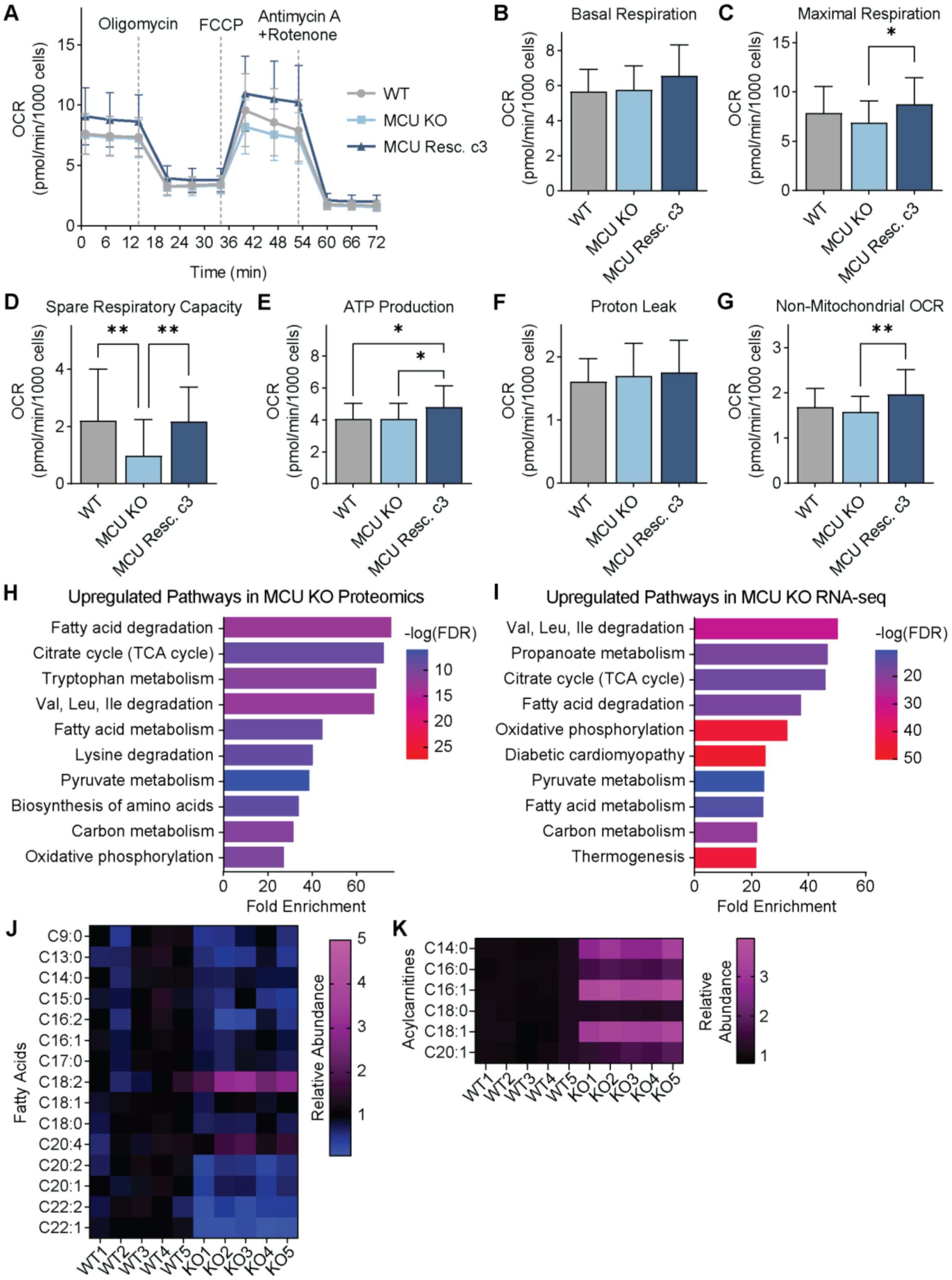

Supplemental Figure 2.1

(A-G) Seahorse extracellular flux analysis in WT, MCU KO, and MCU rescue HeLa cells. Oxygen consumption rate at baseline and after indicated treatments are shown in (A); indicated mitochondrial parameters are shown in (B-G). Statistical significance was determined by the Tukey-Kramer test following one-way ANOVA; n=24-28. **(H, I)** Gene Set Enrichment Analysis of mitochondrial proteins (H) or mRNAs coding for mitochondrial proteins (I) that show a statistically significant increase in MCU KO cells compared to WT cells. **(J, K)** Relative abundance of fatty acids (J) and acylcarnitines (K) in WT and MCU KO HeLa cells; loss of MCU decreases steady state levels of very long chain fatty acids, but increases acylcarnitines, suggesting activation of the mitochondrial FAO pathway. All error bars indicate standard deviation; * indicates a p-value < 0.05 and ** indicates a p-value < 0.01.

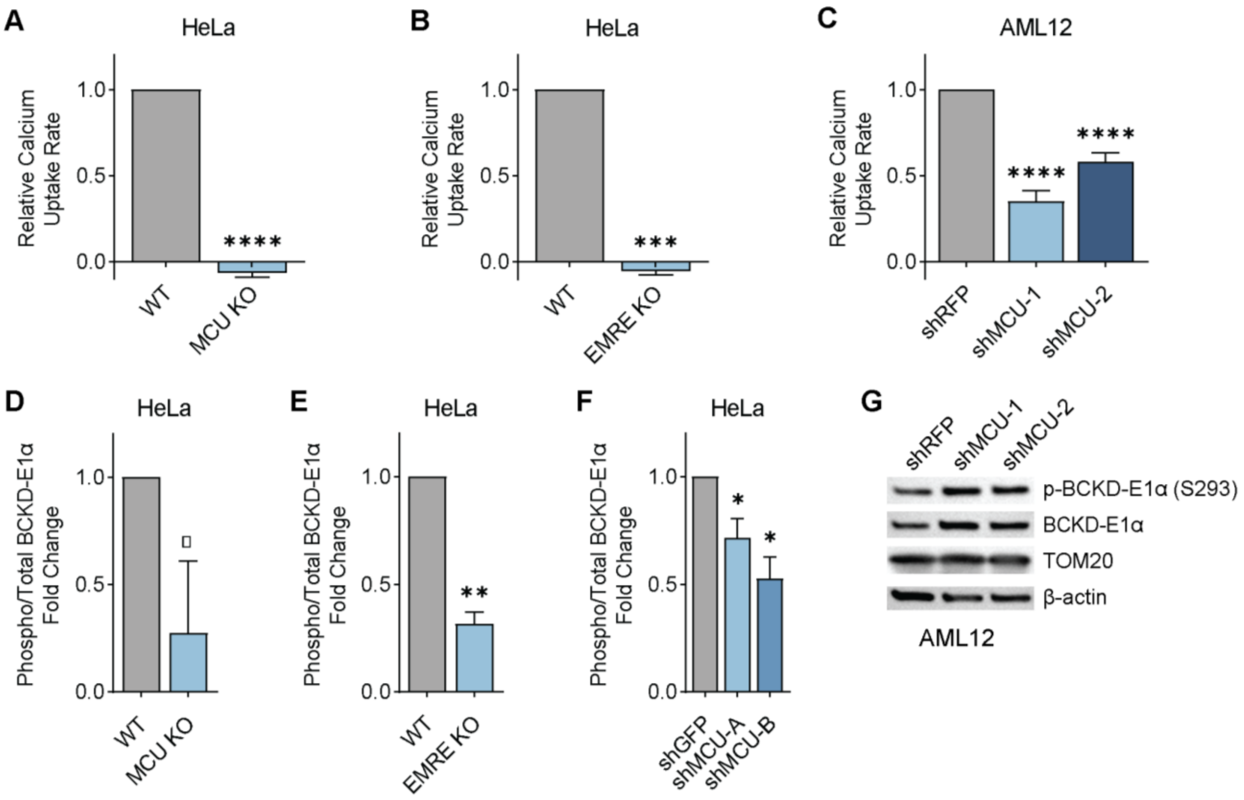

Supplemental Figure 2.2

(A-B) Mitochondrial Ca^{2+} uptake rates in MCU KO (A) and EMRE KO (B) cells relative to WT controls are shown; n=3. **(C)** Mitochondrial Ca^{2+} uptake rates following MCU knockdown compared to control RFP knockdown in AML12 cells; n=8. **(D-F)** Quantification of immunoblots in Fig. 2.2H (D), Fig. 2.2I (E), and Fig. 2.2J (F) are shown as the relative abundance of phosphorylated BCKD-E1α to total BCKD-E1α; n=3. **(G)** Immunoblots of phosphorylated and total BCKD-E1α in AML12 cells with or without MCU knockdown. All error bars indicate standard deviation. * indicates a p-value < 0.05, ** indicates a p-value < 0.01, *** indicates a p-value < 0.001, and **** indicates a p-value < 0.0001.

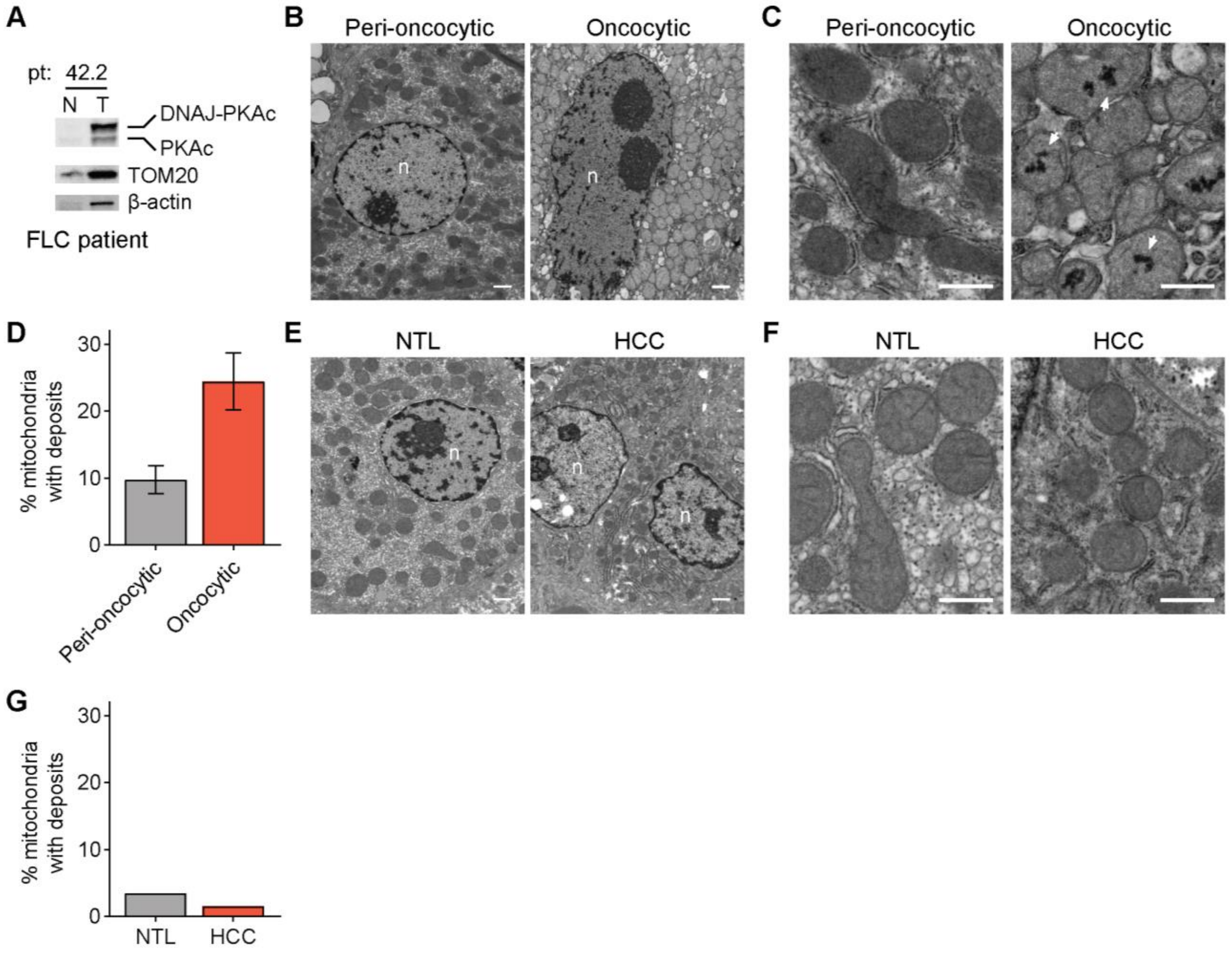

Supplemental Figure 2.4

(A) Immunoblot of tumor (T) and non-tumor liver (N) samples from FLC patient 42.2 showing fusion protein expression. **(B)** Electron micrographs at 10,000x magnification of oncocytic liver cells and proximal cells (peri-oncocytic) from the tumor border of FLC patient 42.2; normal tumor sample was not dissected in this surgery; scale bar = 1 µm; nuclei are labeled n. **(C)** Electron micrographs of samples shown in (B) at 25,000x magnification; white arrowheads mark representative Ca^{2+} deposits in the oncocytic cells; scale bar = 600 nm. **(D)** Percentage of mitochondria with calcium deposits in EM samples shown in (C); the mean is reported from manual counting of >500 mitochondria per sample by two independent, blinded analysts; error bars indicate standard deviation. **(E)** Electron micrographs at 10,000x magnification of non-tumor (NTL) and tumor (HCC) sections from HCC patient 7; scale bar = 1 µm; nuclei are labeled n. **(F)** Electron micrographs of samples shown in (E) at 25,000x magnification; scale bar = 600 nm. **(G)** Percentage of mitochondria with calcium deposits in EM samples shown in (F); >100 mitochondria per sample were quantified by an independent, blinded analyst.

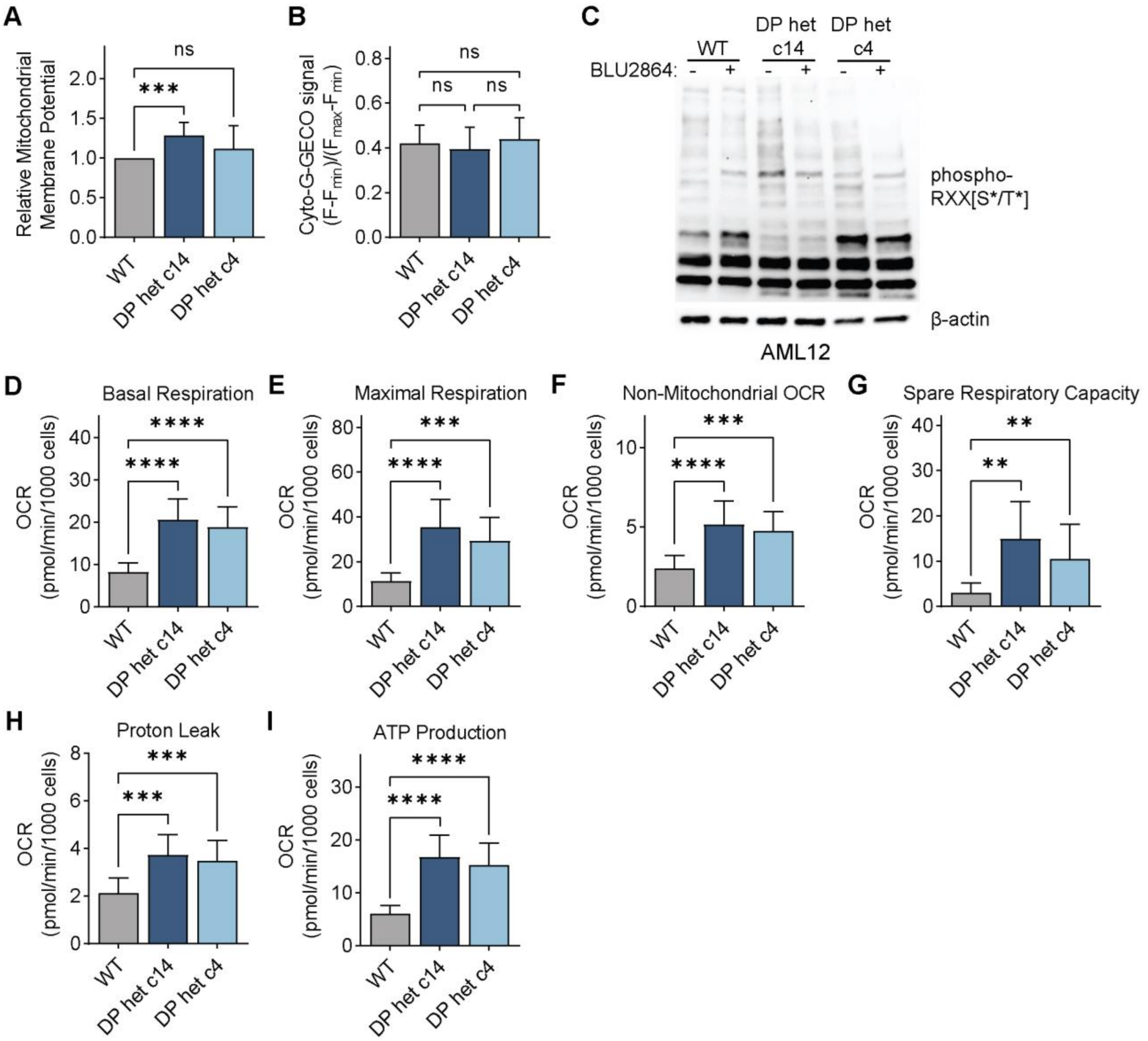

Supplemental Figure 2.5

(A) Baseline cyto-G-GECO fluorescence normalized to minimum and maximum signals in AML12 WT, c14, and c4 cells; statistical significance was determined by one-way ANOVA; n=11-12. **(B)** Resting mitochondrial membrane potential measured by the difference in TMRM fluorescence before and after CCCP addition, normalized to WT AML12 cells. **(C)** Immunoblot of AML12 lysates with a PKA substrate motif antibody after 5 μM BLU2864 or DMSO treatment for 4 days. **(D-I)** Indicated mitochondrial parameters of AML12 cells from Seahorse extracellular flux analysis in Fig. 2.5K; statistical significance was determined by the Dunnett test following Welch's one-way ANOVA; n=10-16. All error bars indicate standard deviation; ns indicates non-significant, ** indicates a p-value < 0.01, *** indicates a p-value < 0.001, and **** indicates a p-value < 0.0001.

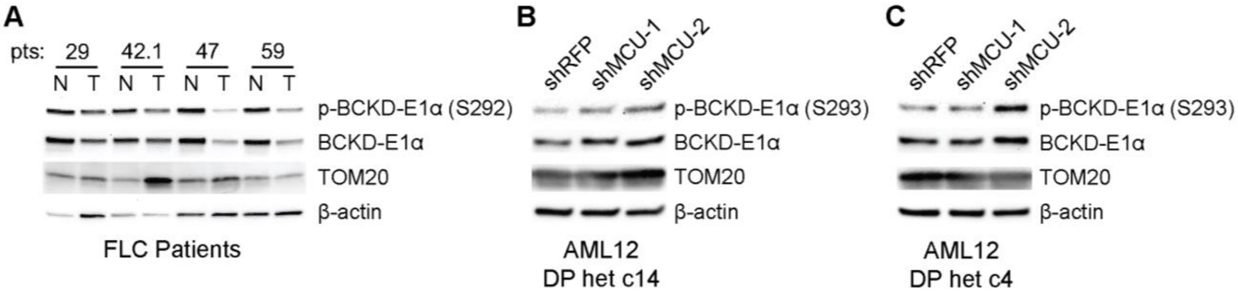

Supplemental Figure 2.6

(A) Immunoblots of phosphorylated and total BCKD-E1α in non-tumor (N) and tumor (T) lysates from FLC patients. **(B, C)** Immunoblots of phosphorylated and total BCKD-E1α in c14 (B) and c4 (C) after MCU knockdown.

2.7.2 | Supplemental Table

Supplemental Table 1. Patient Information

Patient ID	Diagnosis	Age	Sex
7	Hepatocellular carcinoma; history of HCV	70	Female
9	Fibrolamellar carcinoma	27	Male
17	Fibrolamellar carcinoma	14	Female
29	Fibrolamellar carcinoma	20	Male
42.1*	Fibrolamellar carcinoma	26	Male
42.2*	Fibrolamellar carcinoma	27	Male
47	Fibrolamellar carcinoma	26	Male
58	Fibrolamellar carcinoma	18	Female
59	Fibrolamellar carcinoma	18	Female

*Patient 42.1 and 42.2 refer to the same individual; the latter resection was performed following tumor recurrence.

2.8 | References

1 Balderas, E. *et al.* Mitochondrial calcium uniporter stabilization preserves energetic homeostasis during Complex I impairment. *Nat Commun* **13**, 2769 (2022).

2 Gherardi, G. *et al.* Loss of mitochondrial calcium uniporter rewires skeletal muscle metabolism and substrate preference. *Cell Death Differ* **26**, 362-381 (2019).

3 Huo, J. & Molkentin, J. D. MCU genetically altered mice suggest how mitochondrial Ca(2+) regulates metabolism. *Trends Endocrinol Metab* (2024).

4 Kwong, J. Q. *et al.* The mitochondrial calcium uniporter underlies metabolic fuel preference in skeletal muscle. *JCI Insight* **3** (2018).

5 Tomar, D. & Elrod, J. W. Metabolite regulation of the mitochondrial calcium uniporter channel. *Cell Calcium* **92**, 102288 (2020).

6 Baughman, J. M. *et al.* Integrative genomics identifies MCU as an essential component of the mitochondrial calcium uniporter. *Nature* **476**, 341-345 (2011).

7 De Stefani, D., Raffaello, A., Teardo, E., Szabo, I. & Rizzuto, R. A forty-kilodalton protein of the inner membrane is the mitochondrial calcium uniporter. *Nature* **476**, 336-340 (2011).

8 MacEwen, M. J. S. & Sancak, Y. Beyond the matrix: structural and physiological advancements in mitochondrial calcium signaling. *Biochem Soc Trans* **51**, 665-673 (2023).

9 Plovanich, M. *et al.* MICU2, a paralog of MICU1, resides within the mitochondrial uniporter complex to regulate calcium handling. *PLoS One* **8**, e55785 (2013).

10 Sancak, Y. *et al.* EMRE is an essential component of the mitochondrial calcium uniporter complex. *Science* **342**, 1379-1382 (2013).

11 Csordas, G. *et al.* MICU1 controls both the threshold and cooperative activation of the mitochondrial Ca(2)(+) uniporter. *Cell Metab* **17**, 976-987 (2013).

12 Kovacs-Bogdan, E. *et al.* Reconstitution of the mitochondrial calcium uniporter in yeast. *Proc Natl Acad Sci U S A* **111**, 8985-8990 (2014).

13 Liu, J. C. *et al.* MICU1 Serves as a Molecular Gatekeeper to Prevent In Vivo Mitochondrial Calcium Overload. *Cell Rep* **16**, 1561-1573 (2016).

14 Patron, M., Sprenger, H. G. & Langer, T. m-AAA proteases, mitochondrial calcium homeostasis and neurodegeneration. *Cell Res* **28**, 296-306 (2018).

15 Arruda, A. P. *et al.* Chronic enrichment of hepatic endoplasmic reticulum-mitochondria contact leads to mitochondrial dysfunction in obesity. *Nat Med* **20**, 1427-1435 (2014).

16 Konig, T. *et al.* The m-AAA Protease Associated with Neurodegeneration Limits MCU Activity in Mitochondria. *Mol Cell* **64**, 148-162 (2016).

17 Walters, G. C. & Usachev, Y. M. Mitochondrial calcium cycling in neuronal function and neurodegeneration. *Front Cell Dev Biol* **11**, 1094356 (2023).

18 Ghosh, S. *et al.* MCU-complex-mediated mitochondrial calcium signaling is impaired in Barth syndrome. *Hum Mol Genet* **31**, 376-385 (2022).

19 Marchi, S., Giorgi, C., Galluzzi, L. & Pinton, P. Ca(2+) Fluxes and Cancer. *Mol Cell* **78**, 1055-1069 (2020).

20 Fernandez Garcia, E. *et al.* The mitochondrial Ca(2+) channel MCU is critical for tumor growth by supporting cell cycle progression and proliferation. *Front Cell Dev Biol* **11**, 1082213 (2023).

21 Koval, O. M. *et al.* Loss of MCU prevents mitochondrial fusion in G(1)-S phase and blocks cell cycle progression and proliferation. *Sci Signal* **12** (2019).

22 Zhao, H. *et al.* AMPK-mediated activation of MCU stimulates mitochondrial Ca(2+) entry to promote mitotic progression. *Nat Cell Biol* **21**, 476-486 (2019).

23 Liu, J. C. *et al.* EMRE is essential for mitochondrial calcium uniporter activity in a mouse model. *JCI Insight* **5** (2020).

24 Pan, X. *et al.* The physiological role of mitochondrial calcium revealed by mice lacking the mitochondrial calcium uniporter. *Nat Cell Biol* **15**, 1464-1472 (2013).

25 Lombardi, A. A. *et al.* Mitochondrial calcium exchange links metabolism with the epigenome to control cellular differentiation. *Nat Commun* **10**, 4509 (2019).

26 Bauer, T. M. & Murphy, E. Role of Mitochondrial Calcium and the Permeability Transition Pore in Regulating Cell Death. *Circ Res* **126**, 280-293 (2020).

27 Craig, J. R., Peters, R. L., Edmondson, H. A. & Omata, M. Fibrolamellar carcinoma of the liver: a tumor of adolescents and young adults with distinctive clinico-pathologic features. *Cancer* **46**, 372-379 (1980).

28 Farhi, D. C., Shikes, R. H. & Silverberg, S. G. Ultrastructure of fibrolamellar oncocytic hepatoma. *Cancer* **50**, 702-709 (1982).

29 Lloreta, J., Vadell, C., Fabregat, X. & Serrano, S. Fibrolamellar hepatic tumor with neurosecretory features and systemic deposition of AA amyloid. *Ultrastruct Pathol* **18**, 287-292 (1994).

30 Levin, S. N. *et al.* Disruption of proteome by an oncogenic fusion kinase alters metabolism in fibrolamellar hepatocellular carcinoma. *Sci Adv* **9**, eadg7038 (2023).

31 Jeyaraj, D. *et al.* Klf15 orchestrates circadian nitrogen homeostasis. *Cell Metab* **15**, 311-323 (2012).

32 Thakral, N. & Simonetto, D. A. Hyperammonemic encephalopathy: An unusual presentation of fibrolamellar hepatocellular carcinoma. *Clin Mol Hepatol* **26**, 74-77 (2020).

33 Young, M. P. *et al.* Metabolic adaptation to the chronic loss of Ca(2+) signaling induced by KO of IP(3) receptors or the mitochondrial Ca(2+) uniporter. *J Biol Chem* **298**, 101436 (2022).

34 Ge, S. X., Jung, D. & Yao, R. ShinyGO: a graphical gene-set enrichment tool for animals and plants. *Bioinformatics* **36**, 2628-2629 (2020).

35 Huang, B. *et al.* Isoenzymes of pyruvate dehydrogenase phosphatase. DNA-derived amino acid sequences, expression, and regulation. *J Biol Chem* **273**, 17680-17688 (1998).

36 Pezzato, E., Battaglia, V., Brunati, A. M., Agostinelli, E. & Toninello, A. Ca2+ -independent effects of spermine on pyruvate dehydrogenase complex activity in energized rat liver mitochondria incubated in the absence of exogenous Ca2+ and Mg2+. *Amino Acids* **36**, 449-456 (2009).

37 Honeyman, J. N. *et al.* Detection of a recurrent DNAJB1-PRKACA chimeric transcript in fibrolamellar hepatocellular carcinoma. *Science* **343**, 1010-1014 (2014).

38 Gasparre, G., Romeo, G., Rugolo, M. & Porcelli, A. M. Learning from oncocytic tumors: Why choose inefficient mitochondria? *Biochim Biophys Acta* **1807**, 633-642 (2011).

39 Wolf, S. G. *et al.* 3D visualization of mitochondrial solid-phase calcium stores in whole cells. *Elife* **6** (2017).

40 Strubbe-Rivera, J. O. *et al.* The mitochondrial permeability transition phenomenon elucidated by cryo-EM reveals the genuine impact of calcium overload on mitochondrial structure and function. *Sci Rep* **11**, 1037 (2021).

41 Turnham, R. E. *et al.* An acquired scaffolding function of the DNAJ-PKAc fusion contributes to oncogenic signaling in fibrolamellar carcinoma. *Elife* **8** (2019).

42 Dinh, T. A. *et al.* Hotspots of Aberrant Enhancer Activity in Fibrolamellar Carcinoma Reveal Candidate Oncogenic Pathways and Therapeutic Vulnerabilities. *Cell Rep* **31**, 107509 (2020).

43 Zhao, Y. *et al.* An expanded palette of genetically encoded Ca(2)(+) indicators. *Science* **333**, 1888-1891 (2011).

44 Neumayer, C. *et al.* Oncogenic Addiction of Fibrolamellar Hepatocellular Carcinoma to the Fusion Kinase DNAJB1-PRKACA. *Clin Cancer Res* **29**, 271-278 (2023).

45 Toyota, A. *et al.* Novel protein kinase cAMP-Activated Catalytic Subunit Alpha (PRKACA) inhibitor shows anti-tumor activity in a fibrolamellar hepatocellular carcinoma model. *Biochem Biophys Res Commun* **621**, 157-161 (2022).

46 Davis, M. I. *et al.* Comprehensive analysis of kinase inhibitor selectivity. *Nat Biotechnol* **29**, 1046-1051 (2011).

47 Garbincius, J. F. *et al.* MCU gain- and loss-of-function models define the duality of mitochondrial calcium uptake in heart failure. *bioRxiv* (2023).

48 Ericksen, R. E. *et al.* Loss of BCAA Catabolism during Carcinogenesis Enhances mTORC1 Activity and Promotes Tumor Development and Progression. *Cell Metab* **29**, 1151-1165 e1156 (2019).

49 Bowker-Kinley, M. M., Davis, W. I., Wu, P., Harris, R. A. & Popov, K. M. Evidence for existence of tissue-specific regulation of the mammalian pyruvate dehydrogenase complex. *Biochem J* **329 (Pt 1)**, 191-196 (1998).

50 Chen, H., Li, L. L. & Du, Y. Kruppel-like factor 15 in liver diseases: Insights into metabolic reprogramming. *Front Pharmacol* **14**, 1115226 (2023).

51 Shao, D. *et al.* Glucose promotes cell growth by suppressing branched-chain amino acid degradation. *Nat Commun* **9**, 2935 (2018).

52 Auron, A. & Brophy, P. D. Hyperammonemia in review: pathophysiology, diagnosis, and treatment. *Pediatr Nephrol* **27**, 207-222 (2012).

53 Lo, E. K. K. *et al.* The Emerging Role of Branched-Chain Amino Acids in Liver Diseases. *Biomedicines* **10** (2022).

54 Mann, G., Mora, S., Madu, G. & Adegoke, O. A. J. Branched-chain Amino Acids: Catabolism in Skeletal Muscle and Implications for Muscle and Whole-body Metabolism. *Front Physiol* **12**, 702826 (2021).

55 Xiong, Y., Jiang, L. & Li, T. Aberrant branched-chain amino acid catabolism in cardiovascular diseases. *Front Cardiovasc Med* **9**, 965899 (2022).

56 Klyuyeva, A., Tuganova, A., Kedishvili, N. & Popov, K. M. Tissue-specific kinase expression and activity regulate flux through the pyruvate dehydrogenase complex. *J Biol Chem* **294**, 838-851 (2019).

57 McGarrah, R. W. & White, P. J. Branched-chain amino acids in cardiovascular disease. *Nat Rev Cardiol* **20**, 77-89 (2023).

58 Lauer, S. M. *et al.* Recruitment of BAG2 to DNAJ-PKAc scaffolds promotes cell survival and resistance to drug-induced apoptosis in fibrolamellar carcinoma. *Cell Rep* **43**, 113678 (2024).

59 Nishi, K. *et al.* Branched-chain keto acids inhibit mitochondrial pyruvate carrier and suppress gluconeogenesis in hepatocytes. *Cell Rep* **42**, 112641 (2023).

60 Sun, H. *et al.* Catabolic Defect of Branched-Chain Amino Acids Promotes Heart Failure. *Circulation* **133**, 2038-2049 (2016).

61 Kanyomse, Q. *et al.* KLF15 suppresses tumor growth and metastasis in Triple-Negative Breast Cancer by downregulating CCL2 and CCL7. *Sci Rep* **12**, 19026 (2022).

62 Wang, N. *et al.* Circular RNA MTO1 Inhibits the Proliferation and Invasion of Ovarian Cancer Cells Through the miR-182-5p/KLF15 Axis. *Cell Transplant* **29**, 963689720943613 (2020).

63 Wang, X., Liu, J., Xi, S., Pan, X. & Fang, X. Exploring the Mechanism of KLF15 on the Biological Activity and Autophagy of Gastric Cancer Cells based on PI3K/Akt/Mtor Signaling Pathway. *Comb Chem High Throughput Screen* (2024).

64 Wang, Z. H. *et al.* Circular RNA circFBXO7 attenuates non-small cell lung cancer tumorigenesis by sponging miR-296-3p to facilitate KLF15-mediated transcriptional activation of CDKN1A. *Transl Oncol* **30**, 101635 (2023).

65 Zhu, K. Y. *et al.* The functions and prognostic value of Kruppel-like factors in breast cancer. *Cancer Cell Int* **22**, 23 (2022).

66 Sun, C. X. *et al.* MiR-181a promotes cell proliferation and migration through targeting KLF15 in papillary thyroid cancer. *Clin Transl Oncol* **24**, 66-75 (2022).

67 Gray, S. *et al.* Regulation of gluconeogenesis by Kruppel-like factor 15. *Cell Metab* **5**, 305-312 (2007).

68 Haldar, S. M. *et al.* Kruppel-like factor 15 regulates skeletal muscle lipid flux and exercise adaptation. *Proc Natl Acad Sci U S A* **109**, 6739-6744 (2012).

69 Chapuy, C. I., Sahai, I., Sharma, R., Zhu, A. X. & Kozyreva, O. N. Hyperammonemic Encephalopathy Associated With Fibrolamellar Hepatocellular Carcinoma: Case Report, Literature Review, and Proposed Treatment Algorithm. *Oncologist* **21**, 514-520 (2016).

70 Sethi, S. *et al.* Hyperammonemic encephalopathy: a rare presentation of fibrolamellar hepatocellular carcinoma. *Am J Med Sci* **338**, 522-524 (2009).

71 Surjan, R. C., Dos Santos, E. S., Basseres, T., Makdissi, F. F. & Machado, M. A. A Proposed Physiopathological Pathway to Hyperammonemic Encephalopathy in a Non-Cirrhotic Patient with Fibrolamellar Hepatocellular Carcinoma without

Ornithine Transcarbamylase (OTC) Mutation. *Am J Case Rep* **18**, 234-241 (2017).

72 Bell, H. N. *et al.* Microenvironmental ammonia enhances T cell exhaustion in colorectal cancer. *Cell Metab* **35**, 134-149 e136 (2023).

73 Spinelli, J. B. *et al.* Metabolic recycling of ammonia via glutamate dehydrogenase supports breast cancer biomass. *Science* **358**, 941-946 (2017).

74 Wang, Y. *et al.* beta-Catenin Activation Reprograms Ammonia Metabolism to Promote Senescence Resistance in Hepatocellular Carcinoma. *Cancer Res* **84**, 1643-1658 (2024).

75 De Chiara, F. *et al.* Ammonia Scavenging Prevents Progression of Fibrosis in Experimental Nonalcoholic Fatty Liver Disease. *Hepatology* **71**, 874-892 (2020).

76 Domagala, J. *et al.* Ammonia inhibits antitumor activity of NK cells by decreasing mature perforin. *bioRxiv*, 2023.2011.2020.567708 (2023).

77 Barbul, A. Proline precursors to sustain Mammalian collagen synthesis. *J Nutr* **138**, 2021S-2024S (2008).

78 Harada, D. *et al.* Oral administration of l-ornithine increases the content of both collagen constituting amino acids and polyamines in mouse skin. *Biochem Biophys Res Commun* **512**, 712-715 (2019).

79 Mao, L. *et al.* Histone Deacetylase 11 Contributes to Renal Fibrosis by Repressing KLF15 Transcription. *Front Cell Dev Biol* **8**, 235 (2020).

80 Tian, Y. *et al.* KLF15 negatively regulates cardiac fibrosis by which SDF-1beta attenuates cardiac fibrosis in type 2 diabetic mice. *Toxicol Appl Pharmacol* **427**, 115654 (2021).

81 Wang, B. *et al.* The Kruppel-like factor KLF15 inhibits connective tissue growth factor (CTGF) expression in cardiac fibroblasts. *J Mol Cell Cardiol* **45**, 193-197 (2008).

82 Li, S. *et al.* Nobiletin mitigates hepatocytes death, liver inflammation, and fibrosis in a murine model of NASH through modulating hepatic oxidative stress and mitochondrial dysfunction. *J Nutr Biochem* **100**, 108888 (2022).

83 Colledge, M. & Scott, J. D. AKAPs: from structure to function. *Trends Cell Biol* **9**, 216-221 (1999).

84 Gabrovsek, L. *et al.* A-kinase-anchoring protein 1 (dAKAP1)-based signaling complexes coordinate local protein synthesis at the mitochondrial surface. *J Biol Chem* **295**, 10749-10765 (2020).

85 Li, C. J., Lin, H. Y., Ko, C. J., Lai, J. C. & Chu, P. Y. A Novel Biomarker Driving Poor-Prognosis Liver Cancer: Overexpression of the Mitochondrial Calcium Gatekeepers. *Biomedicines* **8** (2020).

86 Ren, T. *et al.* MCUR1-Mediated Mitochondrial Calcium Signaling Facilitates Cell Survival of Hepatocellular Carcinoma via Reactive Oxygen Species-Dependent P53 Degradation. *Antioxid Redox Signal* **28**, 1120-1136 (2018).

87 Ren, T. *et al.* MCU-dependent mitochondrial Ca(2+) inhibits NAD(+)/SIRT3/SOD2 pathway to promote ROS production and metastasis of HCC cells. *Oncogene* **36**, 5897-5909 (2017).

88 Rappsilber, J., Mann, M. & Ishihama, Y. Protocol for micro-purification, enrichment, pre-fractionation and storage of peptides for proteomics using StageTips. *Nat Protoc* **2**, 1896-1906 (2007).

89 Kong, A. T., Leprevost, F. V., Avtonomov, D. M., Mellacheruvu, D. & Nesvizhskii, A. I. MSFragger: ultrafast and comprehensive peptide identification in mass spectrometry-based proteomics. *Nat Methods* **14**, 513-520 (2017).

90 Demichev, V., Messner, C. B., Vernardis, S. I., Lilley, K. S. & Ralser, M. DIA-NN: neural networks and interference correction enable deep proteome coverage in high throughput. *Nat Methods* **17**, 41-44 (2020).

91 Yates, A. D. *et al.* Ensembl 2020. *Nucleic Acids Res* **48**, D682-D688 (2020).

92 Millner, A. *et al.* Ceramide-1-Phosphate Is Involved in Therapy-Induced Senescence. *ACS Chem Biol* **17**, 822-828 (2022).

93 MacEwen, M. J. *et al.* Evolutionary divergence reveals the molecular basis of EMRE dependence of the human MCU. *Life Sci Alliance* **3** (2020).

CHAPTER 3 | CONCLUSIONS

3.1 | Utilization of BCAAs

This work demonstrates BCAAs are an important source of NADH in the absence of mitochondrial calcium signaling while increased BCAA catabolism in MCU KO cells does not correlate with BCAA-derived acetyl-CoA incorporation into the TCA cycle. These observations contribute to a growing body of research which is shifting the narrative about the metabolic utility of BCAA catabolism. BCAA catabolism, like much of biochemistry, has classically been presented as a carbon-centric pathway despite also being a source of amines, NADH, and $FADH_2$ [1, 2]. There is evidence that these other components are also biologically significant. For example, recent work has shown that BCAAs are catabolized in brown adipose tissue for nitrogen utilization without increased TCA cycle incorporation [3]. Additionally, BCAA supplementation increases mouse liver ratios of $NADH/NAD^+$ [4]. This literature in combination with our findings indicates that BCAA-derived products can support multiple metabolic pathways beyond TCA cycle anaplerosis, depending on the tissue type and needs of the cell.

The stimulation of BCAA catabolism is conditional on the cell's $NADH/NAD^+$ redox balance. Improper balance of $NADH/NAD^+$ ratios can have toxic consequences for the cell. Low levels of NADH impairs the ETC [5] and slows MCU KO cell growth [6] while low levels of NAD^+ contributes to ROS accumulation [7]. BCAAs are conserved if there is sufficient replenishment of NADH from other metabolic pathways [8]. In MCU KO cells, however, there is less TCA cycle stimulation and lower ratios of $NADH/NAD^+$ [6, 9]. Conversely, MCU over-activation increases $NADH/NAD^+$ ratios [7]. Here, I propose that reduced NADH/NAD$^+$ as a result of impaired calcium stimulation of the TCA cycle is compensated for by increased BCAA catabolism.

In line with BCAA catabolism as a compensatory source of NADH, the catabolism pathway is regulated by mitochondrial concentrations of NADH. NADH allosterically inhibits the committed catabolism step carried out by the BCKDH complex, thereby limiting BCAA catabolism when NADH levels are high [10]. In contrast, depletion of acetyl-CoA from impaired FAO correlates with suppression of BCAA catabolism, contrary to expectations if BCAA catabolism were upregulated as a compensatory source of acetyl-CoA [11]. This acetyl-CoA-associated regulation is thought to be mediated by loss of histone acetylation (H3K9ac and H3K27ac) at the promoter regions of the BCAA catabolism genes *BCKDHA*, *BCKDHB*, *DBT*, *ACADSB*, and *ACADM*. Given that BCAA catabolism gene expression can be regulated by histone acetylation, it would be interesting to examine whether the Sirtuin family of NAD$^+$-dependent deacetylases are a means of NADH/NAD$^+$-mediated epigenetic regulation of BCAA catabolism [12]. Though the field would benefit from further elucidation of the regulatory mechanisms of BCAA catabolic enzymes, existing literature indicates that low NADH/NAD$^+$ ratios but not low acetyl-CoA stimulates catabolism, aligning with my model in which BCAA catabolism is an important compensatory source of NADH production.

3.2 | Novel signaling axis in FLC

Converse to our observations in MCU KO cells, I demonstrate that FLC tumors suppress expression of BCAA catabolism enzymes. Further characterization of FLC metabolism in DP-expressing AML12 cell line models indicated elevated OXPHOS activity and accelerated cell growth rates. Additionally, high mitochondrial calcium levels in these cells suggests that TCA cycle flux and NADH/$FADH_2$ production are fully stimulated. These findings support the idea that FLC tumors produce sufficient ATP via the canonical TCA-OXPHOS pathways to support increased cellular metabolism. Therefore, BCAA catabolism is likely not required to support TCA cycle anaplerosis or serve as a compensatory source of high energy electron carriers in this cancer. However, increased growth and proliferation requires increased availability of cellular building blocks such as amino acids and nucleotides for protein translation and DNA/RNA synthesis, respectively. These are common features of cancer in general, and increased rates of protein translation have been demonstrated in FLC cell models specifically [13]. Mitochondrial protein translation and ribosome biogenesis are inversely correlated with modulation of the BCAA catabolism pathway, suggesting that BCAA catabolism limits protein synthesis in the mitochondria [14]. I therefore propose that FLC tumor cells benefit from BCAA catabolism suppression due to the conservation of free BCAAs, which are essential and highly utilized amino acids in protein synthesis [15].

My data support a model of FLC metabolic signaling in which BCAA catabolism is tuned by levels of mitochondrial calcium. Downregulation of the majority of BCAA catabolic enzymes is observed at the mRNA level, suggesting the involvement of transcriptional regulators. We identify KLF15 as a uniporter-sensitive transcription factor which is downregulated in FLC tumors and cell models. Based on previous reports of KLF15 function in amino acid metabolism [16, 17, 18] KLF15 is likely to be a relevant transcriptional regulator of BCAA catabolism genes in the context of FLC. However, it remains to be demonstrated how KLF15 and downstream BCAA catabolism gene expression is affected by mitochondrial calcium signaling. Though KLF15 has previously been shown to be responsive to changes in cytosolic calcium signaling events [19], my characterization showed no significant change in concentrations of free cytosolic calcium in FLC cell models. Alternatively, KLF15 expression, DNA-binding, and/or protein stability could be altered by other mitochondrial signaling events or metabolite levels. KLF15 is regulated by starvation conditions [20], glucocorticoids [21], BT2 treatment [14], and the transcriptional regulators CREB [17], PPARδ [22], and FOXO1/3 [23], suggesting potential avenues of future research in FLC signaling and therapeutic design. Furthermore, BCAA catabolism could be sensitized to mitochondrial calcium signaling through direct regulation of catabolic enzyme activities. Consistent with this hypothesis, MMSDH, ACADM, BCAT2, DBT, ACSF3, THIM, and OXCT1 have recently been identified by the Sancak lab as potential calcium-regulated [24]. These findings encourage further work to elucidate the mechanistic steps linking mitochondrial calcium levels and uniporter function to the regulation of BCAA catabolism pathway component expression and activity.

It has long been observed that FLC tumor cells have overly abundant mitochondria [25, 26] and altered urea cycle metabolism [27], but the mechanism by which these mitochondrial phenotypes result from the FLC-associated deletion and expression of the DP fusion protein remains unknown. My work suggests that expression of DP leads to mitochondrial calcium overload which stimulates adaptive changes in amino acid and ammonia metabolism that support tumor growth and development. Going forward, an important research question is how the DP fusion protein dysregulates mitochondrial calcium influx/efflux to elicit this calcium overload phenotype. DP catalytic activity is required for sustained increases in mitochondrial calcium levels, but we have not yet tested whether the J-domain and its protein recruitment properties also contribute to changes in mitochondrial calcium. My data shows that mitochondrial calcium overload is significantly reduced in FLC cell models when treated with the PKA kinase inhibitor BLU2864, suggesting that this FLC phenotype is reversible and subject to pharmacological regulation. In the future, we plan to investigate the therapeutic potential of drugs which regulate mitochondrial calcium influx/efflux as a strategy to either stabilize FLC metabolism or exacerbate mitochondrial calcium concentrations to sensitize tumors to calcium-triggered cell death.

3.3 | Final remarks

Calcium is a critical cellular signaling molecule with diverse effects, and we are only beginning to scratch the surface of its roles in regulation of mitochondrial function. Through this work, we identify mitochondrial calcium signaling as a novel regulator of the enzymatic breakdown of branched-chain amino acids. We propose that this regulation serves as a metabolic switch that can direct these essential amino acids toward catabolic energy production or incorporation into protein synthesis in response to the needs of the cell. In the case of the adolescent liver cancer fibrolamellar carcinoma, mitochondrial calcium overload suppresses components of the BCAA catabolism pathway, including the transcriptional regulator KLF15. Loss of KLF15 expression downstream of mitochondrial calcium signaling may also explain the transcriptional inhibition of the urea cycle in FLC patient livers and the clinical observation that FLC patients can develop dangerous buildup of ammonia in their bloodstream.

Significant progress has been made in both the research fields of mitochondrial calcium signaling and the mechanistic drivers of fibrolamellar carcinoma oncogenesis in the last decade. Building upon that foundation, it is my hope that this body of work will contribute to our growing appreciation of the roles of mitochondrial calcium signaling and open new avenues of research for fibrolamellar carcinoma treatments.

3.4 | References

1. Salcedo, C. *et al.* Functional Metabolic Mapping Reveals Highly Active Branched-Chain Amino Acid Metabolism in Human Astrocytes, Which Is Impaired in iPSC-Derived Astrocytes in Alzheimer's Disease. *Front Aging Neurosci* **13**, 736580 (2021).
2. Vanweert, F., Schrauwen, P. & Phielix, E. Role of branched-chain amino acid metabolism in the pathogenesis of obesity and type 2 diabetes-related metabolic disturbances BCAA metabolism in type 2 diabetes. *Nutr Diabetes* **12**, 35 (2022).
3. Verkerke, A. R. P. *et al.* BCAA-nitrogen flux in brown fat controls metabolic health independent of thermogenesis. *Cell* **187**, 2359-2374.e18 (2024).
4. Surugihalli, C. *et al.* Branched-chain amino acids alter cellular redox to induce lipid oxidation and reduce de novo lipogenesis in the liver. *Am J Physiol Endocrinol Metab* **324**, E299–E313 (2023).
5. Titov, D. V *et al.* Complementation of mitochondrial electron transport chain by manipulation of the NAD+/NADH ratio. *Science* **352**, 231–5 (2016).
6. Balderas, E. *et al.* Mitochondrial calcium uniporter stabilization preserves energetic homeostasis during Complex I impairment. *Nat Commun* **13**, 2769 (2022).
7. Ren, T. *et al.* MCU-dependent mitochondrial Ca2+ inhibits NAD+/SIRT3/SOD2 pathway to promote ROS production and metastasis of HCC cells. *Oncogene* **36**, 5897–5909 (2017).
8. Holeček, M. Role of Impaired Glycolysis in Perturbations of Amino Acid Metabolism in Diabetes Mellitus. *Int J Mol Sci* **24**, (2023).
9. Young, M. P. *et al.* Metabolic adaptation to the chronic loss of Ca2+ signaling induced by KO of IP3 receptors or the mitochondrial Ca2+ uniporter. *J Biol Chem* **298**, 101436 (2022).
10. Bifari, F. & Nisoli, E. Branched-chain amino acids differently modulate catabolic and anabolic states in mammals: a pharmacological point of view. *Br J Pharmacol* **174**, 1366–1377 (2017).

11. Liu, Y. *et al.* CPT1A loss disrupts BCAA metabolism to confer therapeutic vulnerability in TP53-mutated liver cancer. *Cancer Lett* **595**, 217006 (2024).

12. Trapp, J. & Jung, M. The role of NAD+ dependent histone deacetylases (sirtuins) in ageing. *Curr Drug Targets* 7, 1553–60 (2006).

13. Lauer, S. M. *et al.* Recruitment of BAG2 to DNAJ-PKAc scaffolds promotes cell survival and resistance to drug-induced apoptosis in fibrolamellar carcinoma. *Cell Rep* **43**, 113678 (2024).

14. Biswas, D. *et al.* Inhibiting BCKDK in triple negative breast cancer suppresses protein translation, impairs mitochondrial function, and potentiates doxorubicin cytotoxicity. *Cell Death Discov* 7, 241 (2021).

15. Bogatyreva, N. S., Finkelstein, A. V & Galzitskaya, O. V. Trend of amino acid composition of proteins of different taxa. *J Bioinform Comput Biol* **4**, 597–608 (2006).

16. Gray, S. *et al.* Regulation of gluconeogenesis by Krüppel-like factor 15. *Cell Metab* **5**, 305–12 (2007).

17. Shao, D. *et al.* Glucose promotes cell growth by suppressing branched-chain amino acid degradation. *Nat Commun* **9**, 2935 (2018).

18. Chen, H., Li, L.-L. & Du, Y. Krüppel-like factor 15 in liver diseases: Insights into metabolic reprogramming. *Front Pharmacol* **14**, 1115226 (2023).

19. Hirata, Y. *et al.* A Piezo1/KLF15/IL-6 axis mediates immobilization-induced muscle atrophy. *J Clin Invest* **132**, 1–13 (2022).

20. Teshigawara, K. *et al.* Role of Krüppel-like factor 15 in PEPCK gene expression in the liver. *Biochem Biophys Res Commun* **327**, 920–6 (2005).

21. Fan, L., Hsieh, P. N., Sweet, D. R. & Jain, M. K. Krüppel-like factor 15: Regulator of BCAA metabolism and circadian protein rhythmicity. *Pharmacol Res* **130**, 123–126 (2018).

22. Fan, L. *et al.* Transcription factors KLF15 and PPARδ cooperatively orchestrate genome-wide regulation of lipid metabolism in skeletal muscle. *J Biol Chem* **298**, 101926 (2022).

23. Takeuchi, Y. *et al.* FoxO-KLF15 pathway switches the flow of macronutrients under the control of insulin. *iScience* **24**, 103446 (2021).

24. Locke, T. M. *et al.* High-Throughput Identification of Calcium Regulated Proteins Across Diverse Proteomes. *bioRxiv* (2024).

25. Craig, J. R., Peters, R. L., Edmondson, H. A. & Omata, M. Fibrolamellar carcinoma of the liver: a tumor of adolescents and young adults with distinctive clinico-pathologic features. *Cancer* **46**, 372–9 (1980).

26. Farhi, D. C., Shikes, R. H. & Silverberg, S. G. Ultrastructure of fibrolamellar oncocytic hepatoma. *Cancer* **50**, 702–9 (1982).

27. Levin, S. N. *et al.* Disruption of proteome by an oncogenic fusion kinase alters metabolism in fibrolamellar hepatocellular carcinoma. *Sci Adv* **9**, eadg7038 (2023).